



**HAL**  
open science

## Upscaling of geological properties in a world-class carbonate geothermal system in France: From core scale to 3D regional reservoir dimensions

Hadrien Thomas, Benjamin Brigaud, Thomas Blaise, Elodie Zordan, Hermann Zeyen, Maxime Catinat, Simon Andrieu, Emmanuel Mouche, Marc Fleury

### ► To cite this version:

Hadrien Thomas, Benjamin Brigaud, Thomas Blaise, Elodie Zordan, Hermann Zeyen, et al.. Upscaling of geological properties in a world-class carbonate geothermal system in France: From core scale to 3D regional reservoir dimensions. *Geothermics*, 2023, 112, pp.102719. 10.1016/j.geothermics.2023.102719 . hal-04086839v2

**HAL Id: hal-04086839**

**<https://hal.science/hal-04086839v2>**

Submitted on 31 Jul 2024

**HAL** is a multi-disciplinary open access archive for the deposit and dissemination of scientific research documents, whether they are published or not. The documents may come from teaching and research institutions in France or abroad, or from public or private research centers.

L'archive ouverte pluridisciplinaire **HAL**, est destinée au dépôt et à la diffusion de documents scientifiques de niveau recherche, publiés ou non, émanant des établissements d'enseignement et de recherche français ou étrangers, des laboratoires publics ou privés.

# 1 Upscaling of geological properties in a world-class 2 carbonate geothermal system in France: from core 3 scale to 3D regional reservoir dimensions 4

5 Hadrien Thomas<sup>1</sup>, Benjamin Brigaud<sup>1</sup>, Thomas Blaise<sup>1</sup>, Elodie Zordan<sup>2</sup>, Hermann Zeyen<sup>1</sup>,  
6 Maxime Catinat<sup>1</sup>, Simon Andrieu<sup>3,4</sup>, Emmanuel Mouche<sup>5</sup>, Marc Fleury<sup>6</sup>

7 <sup>1</sup>Université Paris-Saclay, CNRS, GEOPS, 91405 Orsay, France

8 <sup>2</sup>Schlumberger, Software Integrated Solutions, Le Palatin 1, 1, cours du Triangle, 92 936 La  
9 Défense Cedex, France

10 <sup>3</sup>BRGM, 3 avenue Claude Guillemin, BP 36009, 45060 Orléans, France

11 <sup>4</sup>Department of Geoscience, Aarhus University, Høegh-Guldbergs Gade 2, 8000 Aarhus C,  
12 Denmark

13 <sup>5</sup>Université Paris-Saclay, CNRS, CEA, UVSQ, Laboratoire des Sciences du Climat et de  
14 l'Environnement, 91191, Gif-sur-Yvette, France

15 <sup>6</sup>IFP Energies nouvelles, 1 et 4 avenue de Bois-Préau, 92852 Rueil-Malmaison Cedex, France  
16

## 17 **Abstract**

18 The greater Paris area has some 12 million inhabitants and 48 heating network production  
19 units that exploit the heat capacity of a 1.5 km deep aquifer, the Bathonian limestone. This is  
20 one of the most productive aquifers in the world for district heating, with an annual output of  
21 about 1.7 TWh of energy. The current challenge for Paris is to triple the number of heating  
22 networks using geothermal energy so as to reduce dependence on fossil fuels (40% in 2020 in  
23 France). As no detailed geothermal reservoir model is available, drilling involves geological  
24 risk. A recent well, drilled at Grigny (20 km south of Paris), turned out to be a failure in

25 transmissibility because the bed of permeable limestones it tapped into was very thin (meter-  
26 scale). The main aim of this study is to create a digital database and a 3D geological model of  
27 this aquifer to minimize geological risks and optimize the location of future geothermal  
28 operations around Paris. By compiling data from 168 wells, a high-resolution 3D geological  
29 model of 360 km<sup>3</sup> size is constructed (about 40 km x 50 km x 0.2 km), made up of 12.2 million  
30 cells and displaying sedimentary facies, sequence stratigraphy, porosity ( $\Phi$ ) and permeability  
31 (k). About 20% of the oolitic and bioclastic facies are of good reservoir quality ( $\Phi > 13\%$  and  $k$   
32  $> 350$  mD), especially in two targeted, high-quality reservoir sequences. These facies of  
33 interest probably correspond to giant dunes and a shoal/barrier prograding from east to west.  
34 In these facies, permeable zones are generally 4 m thick and form patches of 1600 m x 1100 m,  
35 on average, elongated perpendicular to the depositional slope. 2D and 3D maps of  
36 temperature, salinity, porosity, transmissivity, and permeability allow us to understand the  
37 areas of interest for geothermal exploration, as demonstrated around Grigny. This model  
38 helps us to apprehend better the heterogeneous character of the reservoir for geothermal  
39 prospection and to reduce the risk of future doublets during well implantation. Detailed local  
40 models may be extracted to anticipate better the implantation of new doublets in areas with  
41 already densely spaced existing wells.

42 **Keywords:** limestone, Paris Basin, Jurassic, 3D geomodeling, reservoir, facies, geothermics

43

## 44 **1. Introduction**

45 The use of renewable energies has progressed in France over the last ten years, from 250 TWh  
46 in 2010 to 322 TWh in 2020, and they now make up 23% of the country's total energy  
47 production (Beck et al., 2021; Phan et al., 2021). Despite large aquifers in sedimentary basins,  
48 deep geothermal heat accounts for only 0.6% of renewable energy production in France,

49 with 2 TWh in 2020 (Beck et al., 2021; Phan et al., 2021). Heating networks largely depend on  
50 fossil fuels (40% in 2020), and deep geothermal energy represents less than 6% of the energy  
51 mix of heating networks in France (Phan et al., 2021). France's energy-climate strategy is to  
52 produce 5 TWh of geothermal heat by 2028, compared to 1 TWh in 2010 and 2 TWh in 2020  
53 (Beck et al., 2021; Phan et al., 2021). The greater Paris area (Fig. 1A) has exceptional deep  
54 geothermal energy resources, exploited in two main aquifers: (1) the Middle Jurassic  
55 limestones between 1.5 and 2 km depth with a temperature range of 55–80 C and (2) the  
56 Lower Cretaceous sandstones, between 0.5 km and 0.8 km depth and at 30–38 C (Lopez et al.,  
57 2010; Bel et al., 2012). This geothermal energy is mainly used for district heating (Lund and  
58 Toth, 2021). Seventy-six geothermal doublets (152 wells), nine triplets (27 wells) and six single  
59 geothermal wells have been drilled in the greater Paris area since 1931 (Orsay well). In 2022,  
60 43 of these doublets, 9 of these triplets and 3 of the single wells are still active in these two  
61 main reservoirs. The greater Paris region is home to the highest concentration of low-energy  
62 geothermal heating network production units worldwide (Lund and Toth, 2021). While a single  
63 conventional production network unit in the Middle Jurassic aquifer provides heating for 4000  
64 to 6000 housing units, all the production units together provide direct collective heating for  
65 6–7% of the 12 million inhabitants of the greater Paris area. With 48 geothermal heating units  
66 currently producing geothermal water, the Middle Jurassic carbonate is the main aquifer  
67 exploited in the greater Paris area. This aquifer is one of the most productive in the world,  
68 supplying 1.7 TWh of energy per year. As some areas of this aquifer are intensively exploited,  
69 the objective of tripling geothermal energy production implies targeting new areas around  
70 Paris. A 3D high-resolution and predictive geological model could allow better understanding  
71 the reservoir heterogeneity. By transferring knowledge, 3D models allow more doublets to be  
72 drilled efficiently in an area where the density of geothermal wells is significant. There is a real

73 risk that an installation may not reach a geothermal resource with sufficiently high  
74 transmissivity and temperature to ensure the project is cost-effective during its lifetime. Sites  
75 with poor transmissivity are challenging to predict and constitute real obstacles to the future  
76 development of geothermal energy in the greater Paris area. In the late 1980s, pioneering  
77 work by the French Geological Survey (BRGM) proposed maps of facies, porosity, and  
78 transmissivity of the Middle Jurassic carbonate reservoir based on 110 wells drilled between  
79 1976 and 1986 (Rojas et al., 1989). These maps have been used to guide the development of  
80 new operations since the 1990s, but they do not reliably predict low transmissivity areas  
81 because they fail to integrate small-scale variations in facies, porosity, and permeability.  
82 Although 671 wells have been drilled for petroleum exploration or production since the 1950s,  
83 and 186 wells have been drilled for geothermal production, there is currently no detailed 3D  
84 reservoir model on regional scale compiling all the well data of the Middle Jurassic limestones  
85 (Lopez et al., 2010). As no 3D heterogenous geological and no recent geological study of the  
86 reservoir are available, a recently drilled well at Grigny (well GGR-2, at the same location as  
87 GGR-1 Fig. 1) turned out to be a failure regarding water flow as the aquifer turned out to be  
88 composed of very thin beds of porous limestones (meter-scale) with too low transmissivity.  
89 Geological models would help to reduce the risk involved in future geothermal operations  
90 around the Paris region for new doublet implantations (Lopez et al., 2010). Hydro-dynamic  
91 simulations are currently based on highly simplified synthetic models, assuming one  
92 homogeneous productive layer or multiple permeable layers (2 to 7 layers) with homogeneous  
93 hydraulic conductivity (typically  $10^{-6} \text{ m.s}^{-1}$ ) or homogenous permeability (typically 5 Darcys),  
94 separated by impermeable strata (Rojas et al., 1989; Lopez et al., 2010; Le Brun et al., 2011;  
95 Ungemach et al., 2019). However, in Middle Jurassic limestones, with an emphasis on the  
96 Bathonian limestones, permeabilities exhibit a high degree of spatial heterogeneity across all

97 scales, depending largely on the depositional environment and the subsequent diagenetic  
98 processes (Brigaud et al., 2010, 2014a). To achieve the energy-climate objective set out for  
99 France and for the greater Paris area it is essential to de-risk future operations that are often  
100 supported by public investors. This de-risking can be done by better predicting variations in  
101 the 3D carbonate reservoir and the reservoir quality of the Middle Jurassic limestones. The  
102 main problem is finding a way to spatially interpolate the porosity and permeability measured  
103 on rock samples or estimated by well logging from the centimeter or micrometer scale to the  
104 scale of the entire reservoir (hundreds of meters to kilometers). The objective of this work is  
105 to propose a fine-scaled geological model (XYZ dimension of the entire model of about 40 km  
106 x 50 km x 0.2 km and XYZ cell dimension of 100 m x 100 m x 3.73 m on average), based on  
107 upscaled porosity and permeability data measured from mini-cores and well logs and  
108 revealing small-scale heterogeneities.

109 This objective was achieved through the following steps:

- 110 1. data compilation (well log, porosity and permeability) on a volume of 360 km<sup>3</sup> through  
111 the creation of a new, reliable and exploitable database by digitizing old well-logs  
112 available in .pdf or .tiff to ASCII format;
- 113 2. facies heterogeneity analysis by description of cores and cuttings and determination  
114 of facies with good reservoir qualities;
- 115 3. construction of the reservoir architecture by conducting high-resolution sequence  
116 stratigraphy correlation (third-order sequences) and determining the sequence(s)  
117 presenting the best reservoir quality;
- 118 4. definition of a method for upscaling facies distribution applicable to the Middle  
119 Jurassic carbonate platform;

- 120 5. definition of a method for upscaling porosity and permeability from mini-core scale to  
121 regional reservoir proportions;
- 122 6. creation of temperature maps of the geothermal water in the reservoir, temperature  
123 gradient, salinity, and transmissivity to better map the geothermal characteristics;
- 124 7. construction and prediction of reservoir heterogeneity on the regional scale in a 3D  
125 grid composed of 12.2 million cells of X, Y, Z dimensions of 100 m x 100 m x 3.73 m size  
126 (on average for Z) using Petrel© geomodeler.

127 The main objective of this study is to construct a 3D static model of petrophysical properties.  
128 The resulting 3D model is one possible 3D realization showing the geological heterogeneities  
129 and complex sedimentary architecture. Based on the proposed workflow and existing data,  
130 different realizations of static models may be produced allowing quantification of the risk of  
131 failure. Th resulting 3D model will in addition be a prerequisite for thermo-hydro-dynamic  
132 simulations and for optimizing the location of future geothermal operations around Paris.

133        **2. Geological, geothermal and structural settings**

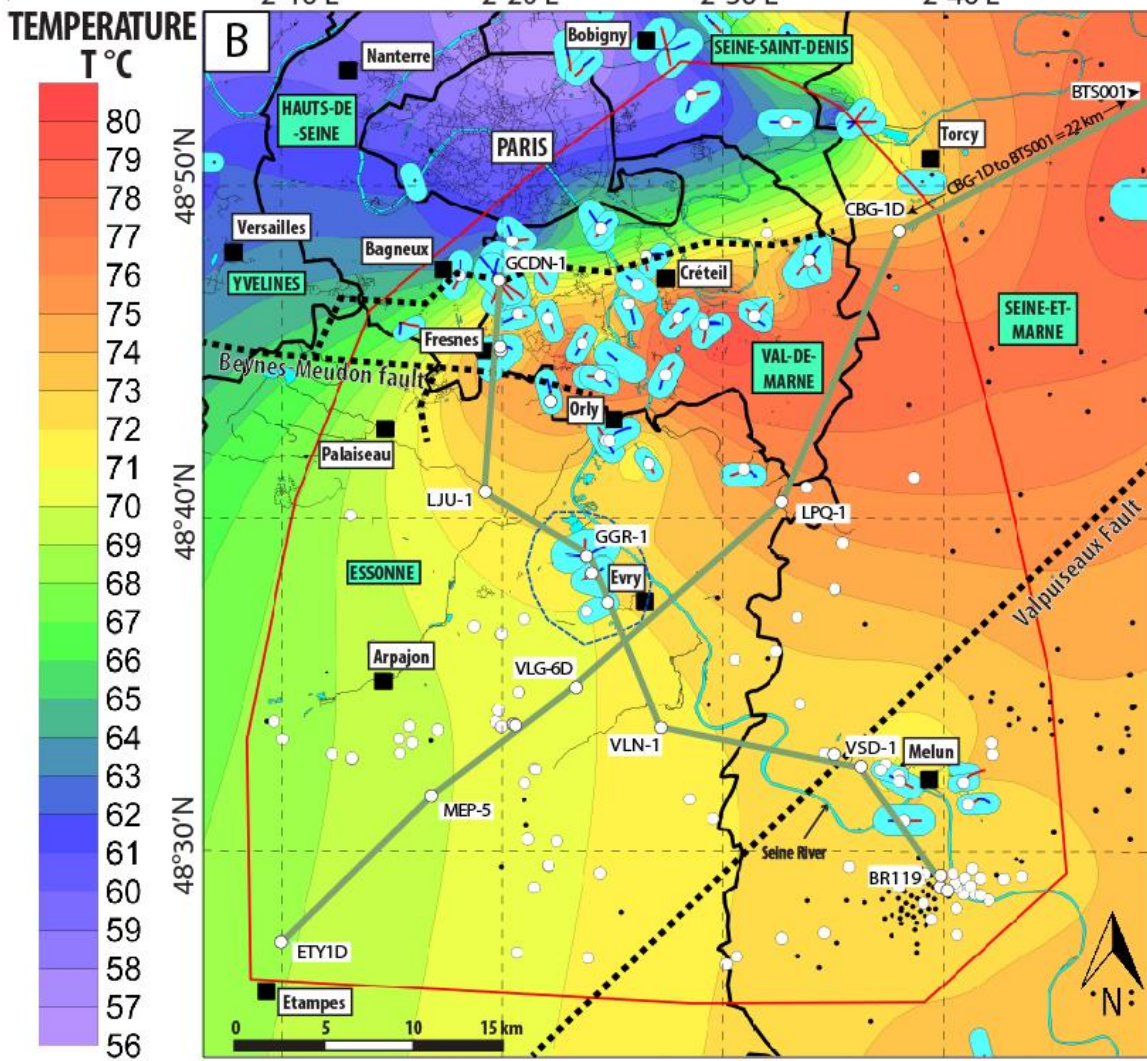
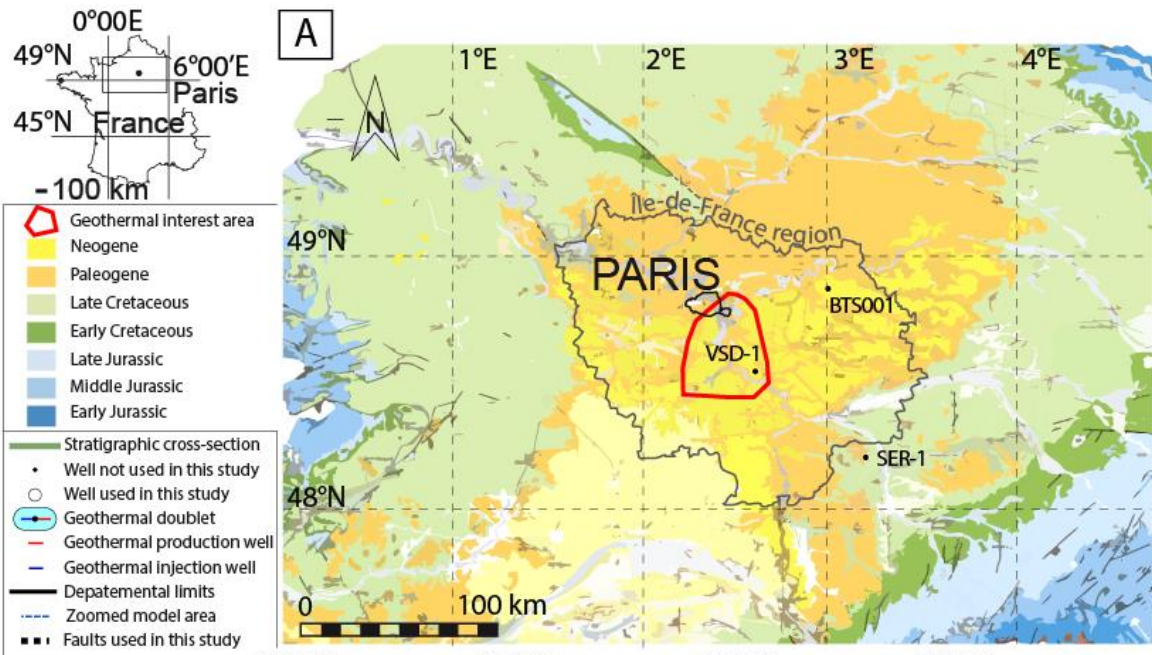
134        This study is based on the well log data available for a specific area of the Paris Basin, between  
135        Paris and Melun (Fig. 1A-B), located in the center of the greater Paris area.

136        *2.1. Structural, palaeogeographic and stratigraphic settings*

137        The Paris Basin is an intracratonic sedimentary basin, formed by three significant tectonic  
138        phases: (1) extension with crustal thinning from the Permian to the end of the Jurassic,  
139        marking a period of intense subsidence; (2) a period of slow subsidence (Early Cretaceous–  
140        Eocene) with an increased rate during the Late Cretaceous; and (3) a period of uplift since the  
141        Neogene (Brunet and Le Pichon, 1982; Guillocheau et al., 2000; Brigaud et al., 2014a). The  
142        basement of the basin comprises Permian-Carboniferous sedimentary deposits and  
143        Palaeozoic granitic and metamorphic rocks. It stretches from east to west for about 600 km,  
144        from the edge of the Armorican massif in the west to the Vosges massif in the east  
145        (Guillocheau et al., 2000). The Paris Basin extends from the English Channel to the Massif  
146        Central from north to south. The structural context of the Paris Basin center has recently been  
147        reappraised from seismic data (Beccaletto et al., 2011; Dentzer et al., 2018). These studies  
148        reveal faults within the study area, such as the Beynes-Meudon fault-anticline system and the  
149        Valpuseaux fault (Fig. 2B). The Beynes-Meudon fault complex originated from the N–S  
150        compressive Pyrenean phase that peaked in the Paris Basin during the Late Eocene (Bergerat,  
151        1984; Guillocheau et al., 2000; Lenoir et al., 2021). The Valpuseaux fault is rooted in the  
152        basement and forms the south-eastern boundary of the Hurepoix block inherited from the  
153        Gondwana-Avalonia collision (Cazes and Torreilles, 1988; Autran et al., 1994; Averbuch and  
154        Piromallo, 2012; Briais et al., 2016).

155





157 Figure 1. A- Location of the study area in the Paris Basin on a simplified geological map of the northern part of France with  
158 the greater Paris boundary (grey outline: administrative Ile-de-France Region) and the model area (red outline). Note the  
159 location of two cores studied: Vert-Saint-Denis-1 (VSD-1) located in the model area near Melun and Sergine-1 (SER-1), out of  
160 the model area. B- Location of the wells on a temperature map at the top of the Bathonian aquifer. Blue ellipses: geothermal  
161 doublets in the aquifer used in the study; white dots: wells used in this study; black dots: other wells present in the region. The  
162 following abbreviations are used: GCDN-1 (Geothermal Cachan Doublet North-1), CBG-1D (Croissy-Beaubourg-1D), BTS001  
163 (Berthuis-1), LJU-1D (Longjumeau-1), GGR-1 (Geothermy Grigny-1), LPQ-1 (Le-Petit-Quincy-1), VLG-6D (Vert-le-Grand-6D),  
164 VLN-1 (Villoison-1), MEP-5 (Marolles-en-Hurepoix-5), VSD-1 (Vert-Saint-Denis-1), ETY-1D (Etrechy-1D), BR119 (Brie-119). The  
165 transect illustrated in figure 9 (green line from SW to NE) is located between ETY-1D in the SW and BTS001 in the NW. The  
166 transect illustrated in figure 10 (green line from NW to SE) is located between GCDN-1 in the NW and BRIE-119 in the SE.  
167 Names in blue boxes are French administrative departments, their boundaries being indicated by black lines.

168

169 During the Middle Jurassic, the study area was a vast epicontinental sea located at subtropical  
170 latitudes of about 30° to 25°N. This marine domain was open to the Atlantic, Tethys, and  
171 Northern seas (Contini and Mangold, 1980; Thierry and Barrier, 2000). Deposits from the  
172 upper Bajocian to lower Callovian consist of alternating marls and carbonates. From bottom  
173 to top, the five sedimentary formations can be described as follows (Fig. 2B, Mégnien and  
174 Mégnien, 1980; Brosse et al., 2010; Delmas et al., 2010):

175 (1) The *Marnes à Ostrea acuminata* consist of marls ranging from a few meters to nearly 50 m  
176 in thickness, deposited in lower to upper offshore environments and dated from the late  
177 Bajocian to the mid-Bathonian (*zigzag* ammonite zone).

178 (2) The *Calcaires marneux à Pholadomyes*, dated from the mid-Bathonian, are mainly  
179 composed of marls deposited in upper offshore environments. Ooid limestone patches are  
180 present locally. The thickness of this formation varies from 30 to 60 m.

181 (3) The *Oolithe Blanche* Formation consists of ooid limestones deposited on a high-energy  
182 shallow platform (Vincent et al., 2021). This formation is the main reservoir for geothermal

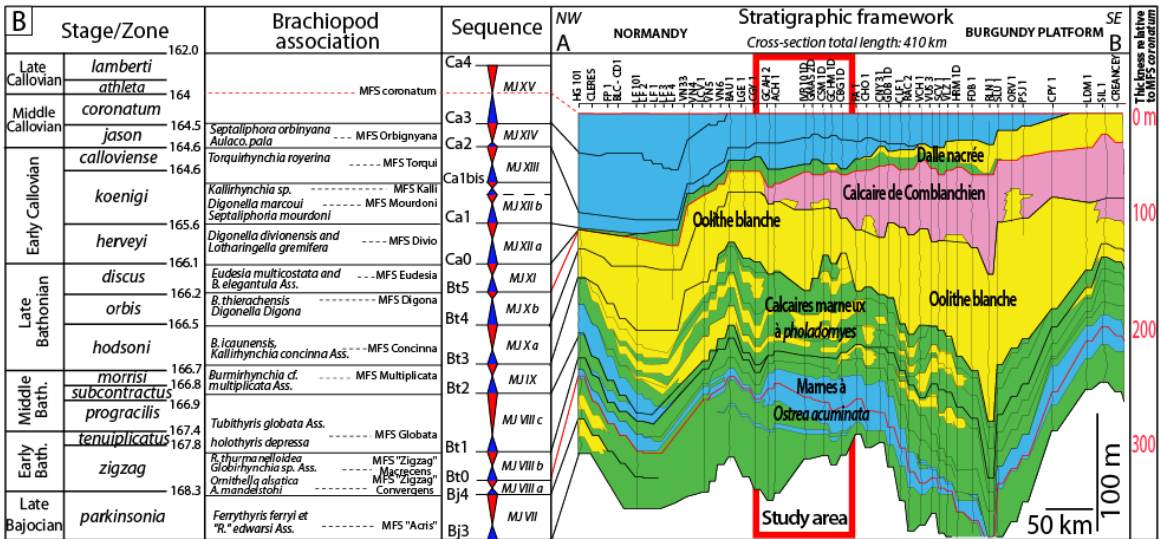
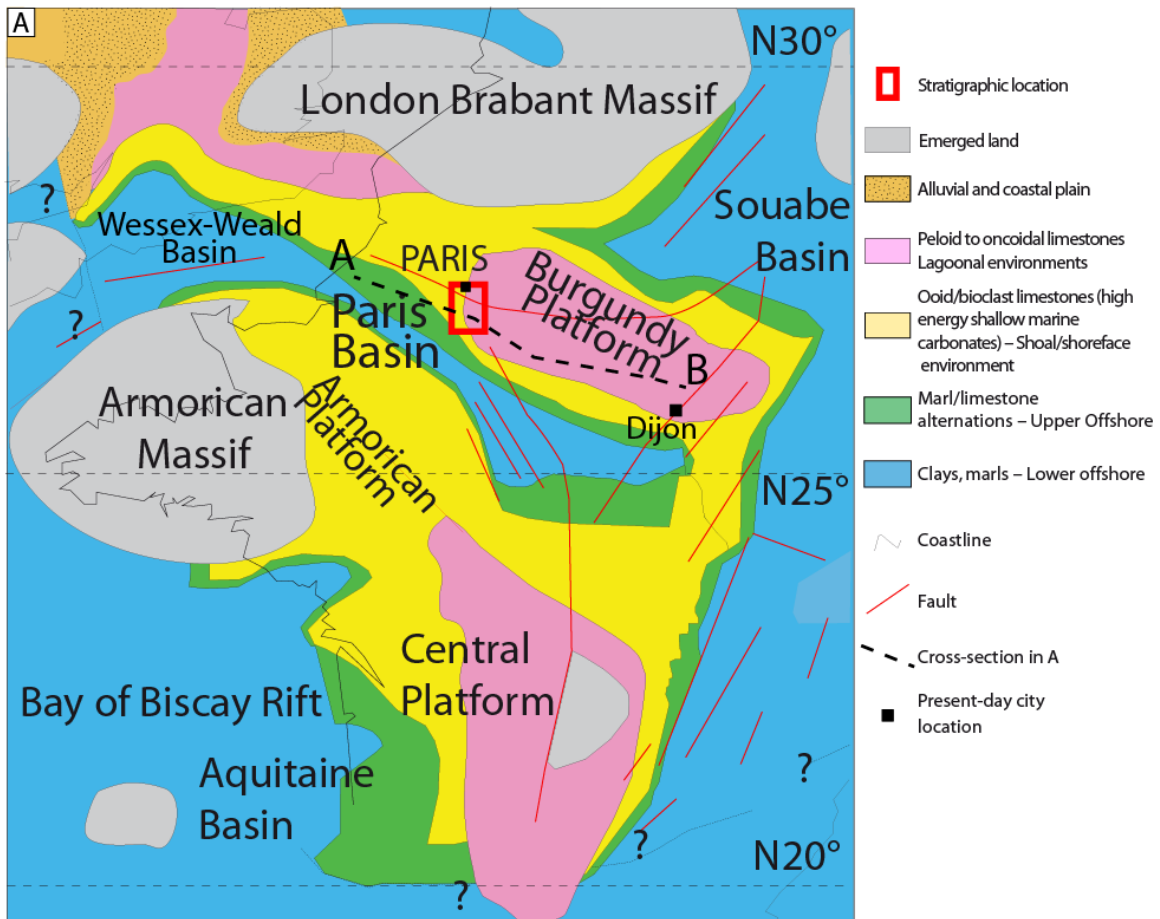
183 energy in the Middle Jurassic limestones (Rojas et al., 1989, Lopez et al., 2010). The thickness  
184 of this formation varies from 50 to 100 m.

185 (4) The *Calcaire de Comblanchien* consists of micritic limestones and oncoidal-bioclastic  
186 limestones. This formation migrates from the south-eastern to the north-western part of the  
187 basin (Gaumet et al., 2001) (Fig. 2B). Small production levels are found locally in this  
188 formation. This formation is absent west of Paris (Fig. 2A, B).

189 (5) The top of the Middle Jurassic limestones is composed of a thin (from a few meters to  
190 20 m) limestone level of the early Callovian age called the *Dalle Nacrée* Formation. It is a well-  
191 known oil reservoir in the Paris Basin (Javaux, 1992; Perrodon and Zabek, 1990). Boreholes  
192 are cemented down to the base of the *Dalle Nacrée* Formation (Lopez et al., 2010), to avoid  
193 oil contamination of geothermal fluids.

194 The total thickness of the upper Bajocian to lower Callovian formations is about 200 m in the  
195 study zone. Purser (1972) recognized three “lithoclines” in the Middle Jurassic limestones of  
196 the eastern Paris Basin, corresponding to biosedimentary packages and forming three  
197 regressive sequences. These three sequences form a progressive upward transition from clays  
198 and marls to shallow marine limestones, topped by a hardground surface (Purser, 1972). The  
199 Bathonian lithocline is well-recognized in the study area from the *Marnes à Ostrea acuminata*  
200 at the base to the *Calcaire de Comblanchien* formation at the top. The cap rock consists of  
201 clayey and marly sedimentary formations dated from the early/mid Callovian to the early  
202 Oxfordian (Vail et al., 1987; Perrodon and Zabek, 1990). In this cap rock, a well-defined meter-  
203 thick iron ooid layer appears in all the well-logs of the Paris Basin (Vail et al., 1987). It is dated  
204 by ammonite fauna from the late Callovian (*athleta* and *lamberti* zones) to the early Oxfordian  
205 (*cordatum* zone) (Vail et al., 1987; Gaumet, 1997; Collin et al., 2005, Figs 2A, 3).

206 The Jurassic limestones of the Paris Basin were selected by Vail et al. (1987) for the first  
207 application of the seismic stratigraphic model (Vail et al., 1977) in an intracratonic basin.  
208 Following this first application, Purser's "lithoclines" were interpreted as second-order  
209 stratigraphic sequences (Jacquin et al., 1992, 1998; Vincent et al., 2021). In the 1990s,  
210 biostratigraphic work resulted in cross-referencing the ammonite zonation with brachiopod  
211 zonations, particularly in sections located in the distal sedimentation area (in the Nièvre  
212 department) (Garcia et al., 1996). This work combines the brachiopod association zonation  
213 with the ammonite zonation, increasing the resolution (Garcia et al., 1996; Garcia and  
214 Dromart, 1997). This zonation enabled the Bathonian and Callovian carbonates to be dated  
215 accurately in oil exploration boreholes in the Paris Basin (Garcia et al., 1996; Gaumet, 1997).  
216 On the carbonate platform, the brachiopod-rich levels correspond to maximum flooding  
217 surfaces (Garcia et al., 1996; Garcia and Dromart, 1997) detailing a third-order sequence  
218 stratigraphy framework, described in the Paris Basin boreholes by Gaumet (1997). From the  
219 Bathonian base to the middle Callovian end, 14 third-order sequences have been recognized  
220 (Garcia et al., 1996; Gaumet, 1997; Jacquin et al., 1998). The maximum flooding surfaces of  
221 each sequence exhibit a specific brachiopod association, enabling us to date these sequences  
222 (Garcia et al., 1996; Thomas et al., 2021; Vincent et al., 2021) (Fig. 2B).



223

224

Figure 2. A- Palaeogeographic map of France and part of England during the Late Bathonian with the location of the study

225

area, adapted from Hendry (2002) and Brigaud et al. (2009). The same color code for facies association types has been used

226

in subsequent figures. The red rectangle in the figures marks the study area. B- Schematic lithostratigraphic section of the

227

Middle Jurassic carbonates reconstructed from wells drilled in the Paris Basin modified from Nader et al., (2016), flattened at

228

the top to the ooid iron layer (Callovian/Oxfordian boundary).

## 229 2.2. Geothermal setting

230 The first geothermal development in the Middle Jurassic limestones of the Paris Basin was  
231 initiated in the late 1960s at Melun (Rojas et al., 1989). The operation consisted of drilling two  
232 wells targeting the Bathonian limestones (*Oolite Blanche* and *Calcaire de Comblanchien*  
233 formations) from 1600 to 1700 m depth to form an open loop with one production well and  
234 one injection well, a technology known as a geothermal doublet (Rojas et al., 1989; Lopez et  
235 al., 2010). 78 doublets or triplets have produced or are producing geothermal water ranging  
236 from 55 to 80 °C, which is re-injected into the Middle Jurassic limestone aquifer at about 40 °C  
237 (Fig. 1B) (Rojas et al., 1989; Lopez et al., 2010). Of the 78 installations, 36 geothermal doublets  
238 and triplets lie within the study area and were drilled into or through the Middle Jurassic  
239 carbonate reservoir (Fig. 1B). Subsurface temperatures were compiled by Housse et al. (1976),  
240 Le Nir et al. (2008), Bonté et al. (2010) and Lopez et al. (2010). The temperature of the aquifer  
241 is heterogeneous (Fig. 1B). The lowest temperatures are found in the northern part of the  
242 study area, below Paris and the Seine-Saint-Denis Department (Fig. 1B), reaching about 50 °C  
243 at a depth of 1650 m (thermal gradient about 23 °C/km). Temperatures in the study area are  
244 the highest south-east of Créteil (around 80 °C at a depth of 1660 m, thermal gradient of  
245 40.9 °C/km) and south of Cachan (east of Fresnes, around 75 °C at a depth of 1590 m, thermal  
246 gradient of 39.6 °C/km). From Fresnes to the south of Paris, the temperature drops by 18 °C  
247 from 72 °C in Fresnes GFR1D well (1600 m below the surface, thermal gradient of 37.5 °C/km)  
248 to 54 °C south of the Paris boundary in the GBA1 well located at Bagneux (1510 m below the  
249 surface, thermal gradient of 27.8 °C/km, Fig. 1B). All the gradients are computed assuming a  
250 mean surface temperature of 12 °C. A possible explanation for temperatures dropping locally  
251 by nearly 20°C at the top of the reservoir may be the presence of pervasive fractures, leading  
252 to downward flow from the Cretaceous aquifers, but this explication is still debated in the

253 community (Dentzer et al., 2018). The temperature in the western part of the study zone is  
254 not well defined as no geothermal wells are available and historical exploration wells did not  
255 report reliable well temperatures (Fabris, 1975). Additional information on groundwater flow  
256 and salinity can be found in the works of Fabris (1975), Aubertin et al. (1987), Wei et al. (1990),  
257 Menjoz et al. (1993) and Matray and Chery (1998).

258

### 259 **3. Material and methods**

#### 260 *3.1 Cores, well-logs, petrophysical data, temperature, and salinity*

261 The digital database was compiled from logs, reports and other technical data from 168 wells  
262 (94 oil exploration wells and 74 geothermal wells) available in the French Geological Survey  
263 subsurface database (BRGM, <https://infoterre.brgm.fr/>). The Sergines-1 and Berthuis-001  
264 wells are considered in this study as reference wells but are not included in the final modeled  
265 zone (Fig. 1A). The well logs generally consisted of gamma-ray logs (GR, 151 logs), sonic logs  
266 (delta time, DT, 74 logs), resistivity logs (mainly laterolog deep, LLd and laterolog shallow, LLs,  
267 62 logs), spontaneous potential logs (SP, 39 logs) and calliper logs (CAL, 5 logs). Porosity logs  
268 (neutron porosity, NPHI, neutron, NEUT, total combinable magnetic resonance, TCMR or  
269 related) were available for 76 wells, and density logs (Rho<sub>b</sub>) for 39 wells. An Nuclear Magnetic  
270 Resonance (NMR) logging tool (Combinable Magnetic Resonance - CMR©) was only available  
271 for the Cachan GCAH-2 well (Ungemach et al., 2019; Wielemaker et al., 2020). The NMR  
272 logging tool provides continuous porosity and permeability along a well (Westphal et al.,  
273 2005). The permeability ( $k_{SDR}$ ) from the NMR tool is obtained with the Schlumberger Doll  
274 Research (SDR) default relationship (Kenyon et al., 1988). Routine petrophysical analyses of  
275 porosity ( $\Phi$ ) and permeability ( $k$ ) from mini-cores (plugs from cores) were compiled from well-  
276 reports, from 40 wells for  $\Phi$  (4561 measurements in total) and 37 wells for  $k$  (3317

277 measurements in total).  $\Phi$ -k data were tabulated in an Excel spreadsheet and converted into  
278 “.las” data files to be geolocated in 3D. 64 wells included water temperatures, and 66 wells  
279 reported salinity values in the aquifer. All the log data are available in the supplementary data  
280 sheet (Supplementary Table A). The well coordinates, trajectory, logs, temperature, salinity,  
281 and  $\Phi$ -k data measured on mini-cores were imported into the Petrel© software for 3D  
282 processing. The well list is available in Supplementary Table A and  $\Phi$ -k data in Supplementary  
283 Table B.

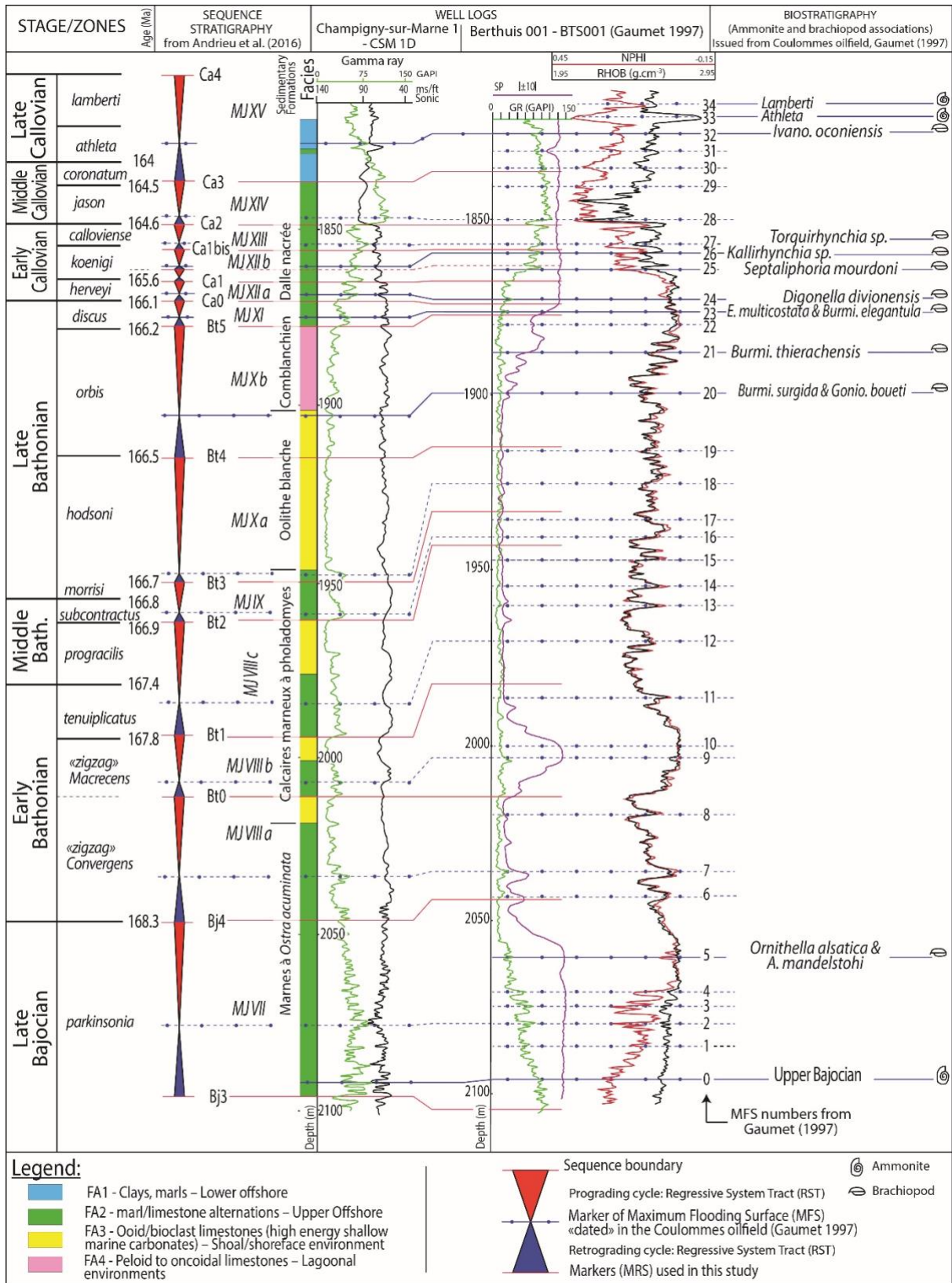
### 284 *3.2 Petrography and sequence stratigraphy*

285 Vert-Saint-Denis 1 (VSD1) and Sergines 1 (SER1) well cores, stored at the BRGM core storage  
286 facility, were described. Thirty-four samples for these two core-wells as well as 123 cutting  
287 samples from nine other wells (Paris Aéroport 1&2, Bagneux 1&2, Fresnes 3D, Cachan 1&2,  
288 Villejuif 1&2, Supplementary data A) were selected for thin-section manufacturing. These thin  
289 sections were impregnated with blue resin to highlight the porosity and easily differentiate it  
290 from the diagenetic calcite cements. Samples were extracted from the drilling mud to obtain  
291 thin sections from cuttings. Once dry and clean, they were sorted (clast diameter of more than  
292 1 mm) to extract the coarse (1 mm) fraction of each sample. These 157 thin sections enabled  
293 us to determine facies, facies associations, pore space, and diagenetic cements in the  
294 reservoir. These thin sections were observed and described under an optical microscope  
295 (Leica DM750 P). A Micro-Computed Tomography scanner ( $\mu$ CT scan) was used to investigate  
296 the 3D pore space at high resolution in a sample in the Vert-Saint-Denis 1 well (VSD-  
297 1\_1712,9m). The  $\mu$ CT scans were performed at IFPEN with a microtomograph X EasyTOM from  
298 RX Solution.

299 Following the definition of Embry and Johannessen (2017), sequence stratigraphic  
300 interpretations were performed, integrating data from 168 wells (Fig. 1). Maximum flooding



301 surfaces (MFS) mark the boundary between deepening-upward and shallowing-upward  
302 trends. Subaerial unconformities or maximum regressive surfaces correspond to sequence  
303 boundaries (SB), labelled following the definition of recently compiled for the Bathonian of  
304 the Paris Basin. For the sequence stratigraphy and biostratigraphic framework, the well-  
305 known Coulommès oilfield discovery in 1958 was taken as reference (Gaumet, 1997).  
306 Brachiopod fauna in the Coulommès 001 well (CS001) provided a reference for sequence  
307 stratigraphy in the Middle Jurassic limestones (Gaumet, 1997). Wells were correlated  
308 between Coulommès and Berthuis (BTS001) by Gaumet, (1997) and throughout the basin  
309 (Gaumet, 1997; Delmas et al., 2010; Houel and Delmas, 2013). As brachiopod levels  
310 correspond to maximum flooding surfaces (MFS) in this platform, Gaumet (1997) used 34  
311 MFSs to define third-order sequences (Fig. 3). Maximum flooding surfaces are recognized in  
312 well-logs by Gamma-Ray maxima (Fig. 3). In this study, we also included the location of MRSs,  
313 identified, from bottom to top, by the onset of an increase of Gamma-Ray (Fig. 3). MRS  
314 corresponds to the top of a shallowing-upward trend, for example top of ooid-bioclast  
315 limestone units (Fig. 3). A total of 15 MRSs and 15 MFSs were correlated from BTS001 to  
316 Champigny-sur-Marne 1 well (CSM1D) (Fig. 3). These surfaces were propagated along the 168  
317 wells of the study area. Following the labeling of Garcia et al. (1996), Gaumet (1997), and  
318 Hardenbol et al. (1998), two MRSs (Bj3 and Bj4) are defined in the Bajocian, six in the  
319 Bathonian (Bt0 to Bt5) and six in the Callovian from Ca0 to Ca4 (Fig. 3).



320

321

Figure 3. Biostratigraphic and well-log calibration between Champigny-sur-Marne (CSM 1D) well (see Fig. 2B for location in

322

the study area) and the reference well of Berthuis 001 (BTS001) in the Coulommès oil field. The biostratigraphy of this oil field,

323 including the well-log of BTS001, is defined by Gaumet (1997). Maximum flooding surfaces (MFS) with biostratigraphy in  
324 Coulommès oilfield appear in blue continuous lines, without biostratigraphy in blue dotted lines.

325

### 326 3.3 Facies, stratigraphic, and petrophysical 3D modeling

#### 327 3.3.1. 3D grid creation

328 Eighteen stratigraphic surfaces were defined on well sections: MRSs from Bj3 to Ca4, the iron  
329 oolite layer (condensed MFSs *Athleta* and *Lamberti*), the Toarcian/Aalenian top, the  
330 Toarcian/Aalenian base and the basement top. Of these 18 stratigraphic surfaces, 14 (surfaces  
331 Bj4 to Ca4) were used to define 13 stratigraphic zones in the model (sequences MJVII, MJVIIIa,  
332 MJVIIIb, MJVIIIc, MJIV, MJXa, MJXb, MJXI, MJXIIa, MJXIIb, MJXIII, MJXIV, MJXV, Fig. 3). The  
333 other surfaces were not within the stratigraphic framework of the model. Four facies  
334 associations were encoded in 168 wells using well logs, well reports, cuttings, and core  
335 samples. Two cross-sections at a regional scale were produced, one oriented North-South and  
336 one oriented East–West. To ensure compatibility with other software, the corner point  
337 gridding algorithm (based on the pillar gridding algorithm) was used to create the 3D grid.  
338 Faults were modeled using the structural maps provided by the BRGM (Beccaletto et al., 2011;  
339 Dentzer et al., 2018). They were then transformed as fault sticks in Petrel© and used as inputs  
340 in the structural and fault framework of the model. Cell size was set to 100 m in the I and J  
341 (horizontal) directions. A total of 52 layers were modeled with 3.76 m mean thickness in the  
342 K direction. This resulted in a grid of 12.2 million cells.

#### 343 3.3.2. Property upscaling

344 The facies log was upscaled using the “most of” method without weighting. This method took  
345 the log values going through the cell and encoded the cell with the most commonly  
346 represented value. In total, the model has 6384 facies cells encoded using this method.

347 The well-interpreted and porosity-calibrated NPHI (28 logs), NMR (1 log), and NEUT (7 logs),  
348 as well as the min-core data (40 logs) were combined and upscaled to maximize cells  
349 containing porosity data (1686 cells). Sixty-nine porosity logs were considered for upscaling  
350 porosity in the model (Supplementary data A). Mini-cores were the calibrating tool for  
351 neutron-based data. Mini-cores and TCMR data were prioritized over NPHI-based data. The  
352 porosity logs were then upscaled using the arithmetic averaging method. This method takes  
353 the average value of all the data points of a well crossing a cell. Thirty-eight permeability logs  
354 were used for upscaling (37 permeabilities from mini-cores and one from NMR). The  
355 permeability data were upscaled using the geometric averaging method. The temperature and  
356 salinity properties were upscaled using the arithmetic averaging method. Temperature data  
357 is given in 65 wells at the top of the reservoir, measured at the beginning of the geothermal  
358 production. Only one well presents a continuous temperature log.

### 359 3.3.3. Facies, porosity, and permeability modeling

360 The “Truncated Gaussian with Trends” algorithm was used to model facies associations,  
361 stratigraphic zone by stratigraphic zone. This algorithm allowed us to define boundaries  
362 between facies associations. Facies were locally refined to better fit the stratigraphic well  
363 correlation diagrams (brush tool). This step was critical as the petrophysical properties are  
364 highly correlated to the facies (Nurmi, 1986; Borgomano et al., 2008; Tomassetti et al., 2018;  
365 Trippetta et al., 2021).

366 Facies is commonly accepted as a factor controlling porosity in the Middle Jurassic carbonates  
367 of the Paris Basin (Brigaud et al., 2014b). For porosity, and depending on the facies, the  
368 transformation part of the Data Analysis with Petrel© was used to prepare the data and  
369 determine the distribution used in the model (i.e., input truncation and normal score). For the  
370 normal score transformation, the “define curve” option was used to match the porosity

371 distribution with facies from the mini-core data in the wells and to apply it statistically to the  
372 entire volume of the model. The same approach was used for permeability by adding a  
373 logarithmic transformation to account for the porosity versus permeability logarithmic  
374 relationship.

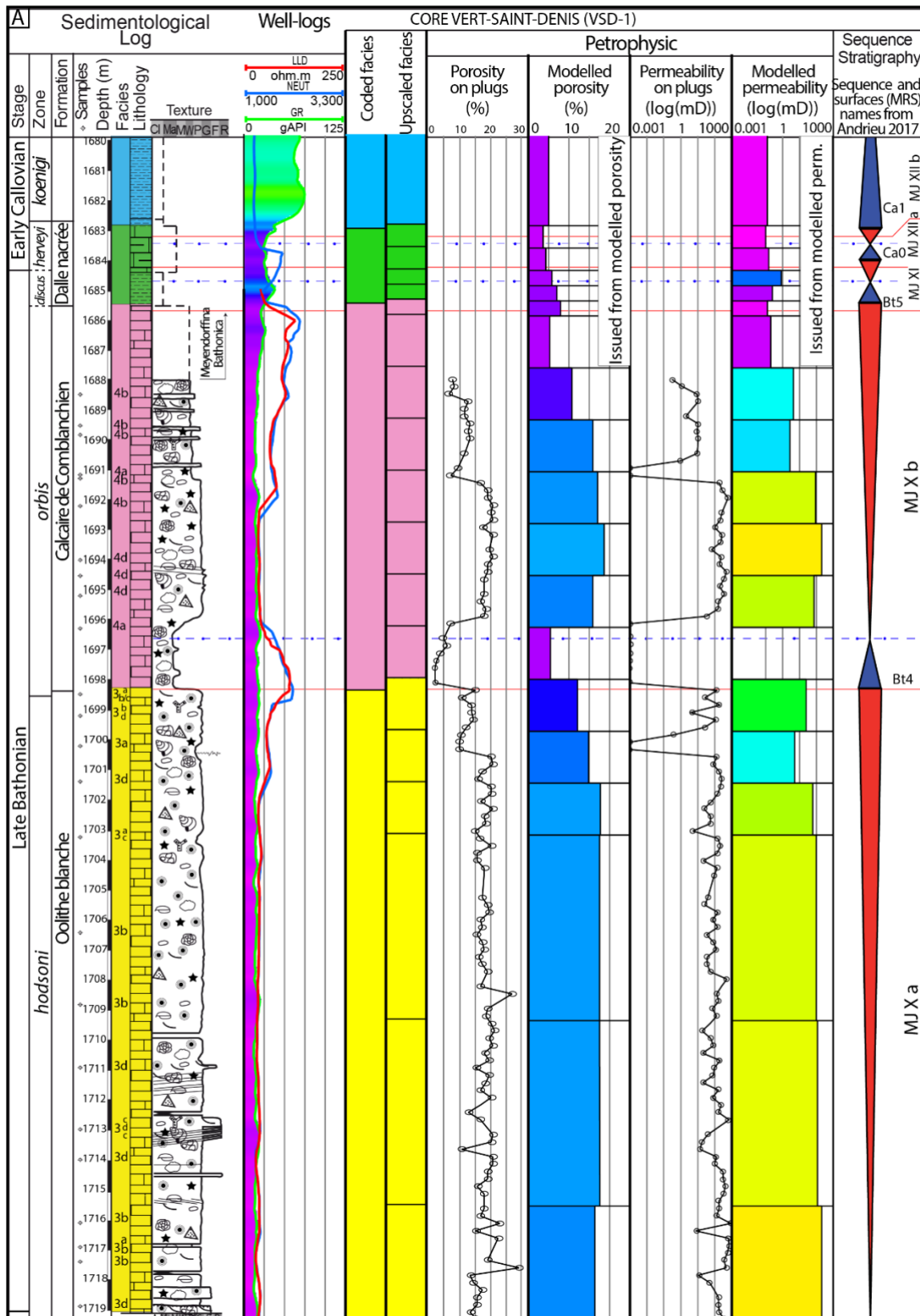
375 To detect the anisotropy of the data (porosity and permeability), a variogram map based on  
376 the upscaled porosity was created. Variograms were conducted on the overall model for each  
377 facies association to populate porosity in the grid, and then zone by zone, facies by facies in 2  
378 key zones of the reservoir with high data density. The same process was used for permeability.

379

## 380 **4. Results**

### 381 *4.1 Sedimentary facies*

382 Thirteen facies are identified for the entire study, grouped into four depositional  
383 environments (FA – Facies Associations) ranging from lower offshore to lagoon (Fig. 4, Fig. 5,  
384 Table 1). Facies associations have been defined for the eastern part of the Paris Basin in the  
385 synthesis of Brigaud et al. (2014a) on Jurassic formations. The distribution of facies  
386 associations is shown on a theoretical profile from the lower offshore in the outer ramp to  
387 lagoon in the inner ramp (Fig. 5).



388

389

Figure 4A. Section of the Vert-Saint-Denis-1 core located in the Paris Basin (VSD-1 located in Fig. 1). This core section displays

390

the sedimentological log with the constituent allochems and texture, well-logs laterolog deep (LLD), neutron (NEUT) and

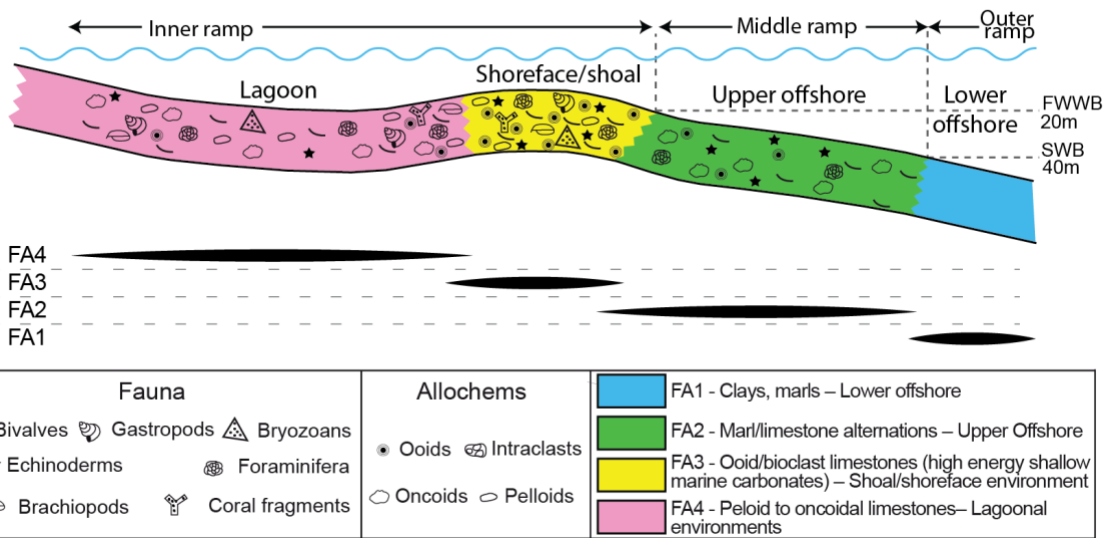
391 gamma-ray (GR) and facies association codes. Porosity and permeability measured on mini-cores and sequence stratigraphy  
 392 have been reported. Upscaled values of facies, porosity and permeability are also indicated.

LEGEND	Fauna		Allochems		Texture		
	Bivalves	Gastropods	Echinoderms	Ooids	Intraclasts	Ma: Marl	P: Packstone B: Boundstone
	Bryozoans	Foraminifera	Oncoids	Pelloids	M: Mudstone	G: Grainstone	
	Brachiopods	Coral fragments			W: Wackestone	R: Rudstone	
Surface					Lithology		
hardground					Shoal	Clays	
					Marls alternances		
FA4 - Peloid to oncoidal limestones – Lagoonal environments			FA3 - Ooid/bioclast limestones (high energy shallow marine carbonates) – Shoal/shoreface environment			RST Regressive Systems Tract	
F4a - Peloidal wackestone/packstone with foraminifera and echinoderms			F3a - Peloidal packstone with bioclasts				
F4b - Low to moderately cemented peloidal grainstone			F3b - Low to moderately cemented ooid grainstone with bioclasts				
F4c - Oncolithic floatstone			F3c - Highly cemented ooloidal grainstone with bioclasts				
F4d - Rudstone with intraclasts			F3d - Rudstone to grainstone with bivalves and intraclasts			TST Transgressive Systems Tract	
FA2 - Marl/limestone alternations – Upper Offshore			FA1 - Clays, marls – Lower offshore				

393

394 Figure 4B. Legend of the core section presented in Fig. 4A.

395



396

397 Figure 5. Distribution of the Bathonian facies associations on a theoretical downdip profile. This synthetic profile shows the  
 398 succession of the facies across the platform, depending on bathymetry.

399

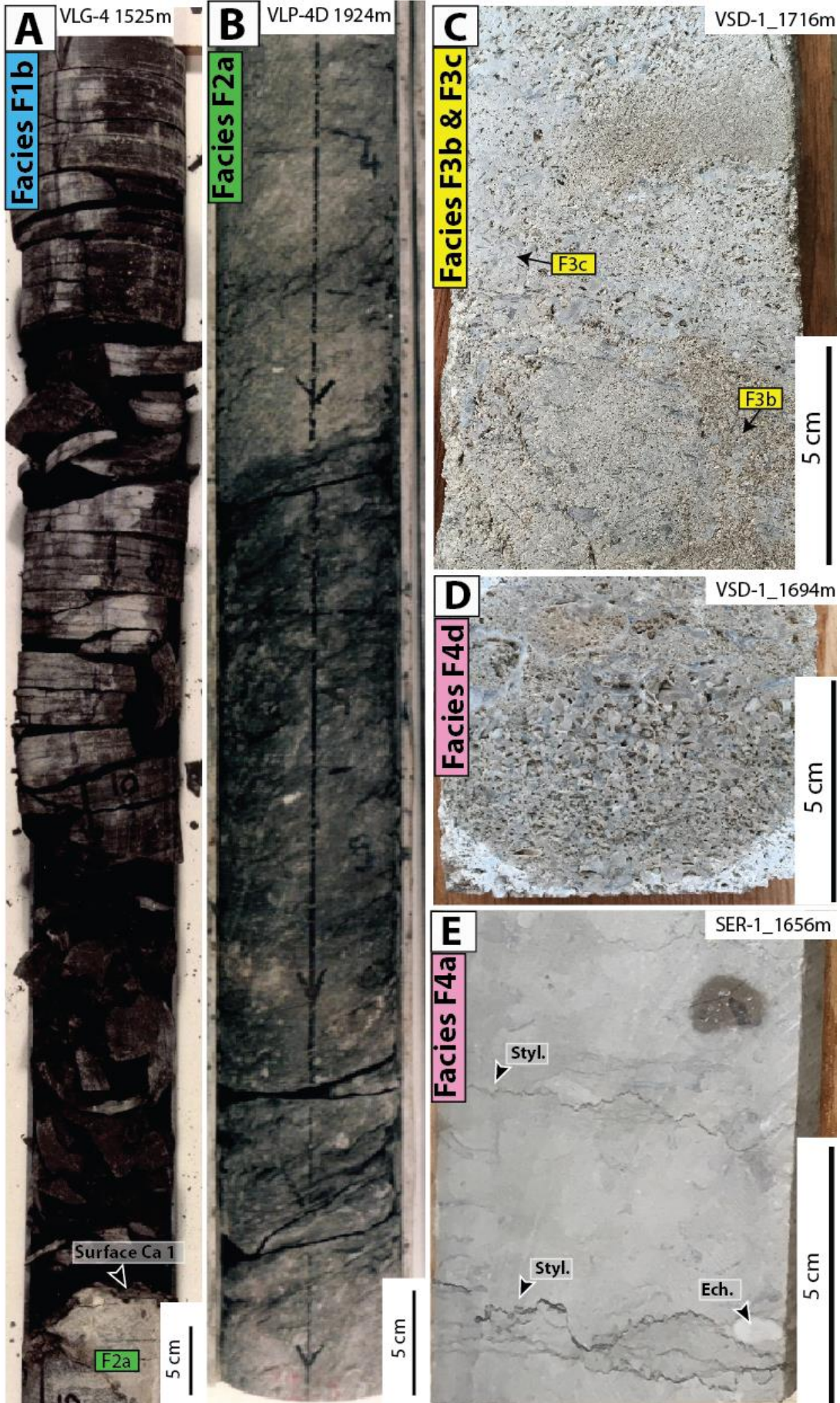
400 4.1.1. Clays, marls – Lower offshore environment (facies association FA1)

401 Description – Two facies are grouped in the lower offshore facies association (Fig. 5): (1) marls  
 402 (facies F1a) and (2) clays (facies F1b) (Figs 4, 5, and 6A, and Table 1). Facies F1a is composed

403 of clays and silts (Table 1). Faunas are composed of ammonites, belemnites, brachiopods, and  
404 echinoderms. Facies F1a occurred mainly during the Callovian, and locally during the late  
405 Bajocian and early Bathonian (Figs 3 and 4). Facies F1b is composed exclusively of clays (Figs  
406 4, 5 and 6A, Table 1). Although these two facies mainly appear in the Callovian deposits,  
407 forming the cap-rock of the aquifer, some local appearances are also detected in the late  
408 Bajocian deposits.

409 Interpretation – The absence of hydrodynamic sedimentary structures, the presence of  
410 ammonites and belemnites, bivalves or brachiopods in life position, and abundant  
411 bioturbation indicate very low energy conditions in an open distal marine environment, below  
412 the storm wave base, probably at a water depth of more than 40 m (Andrieu et al., 2016) (Fig.  
413 5). Considering the predominance of clays and marls in this facies, effective porosity and  
414 permeability are expected to be very low. This facies forms the cap rock of the reservoirs and  
415 locally impermeable layers in the *Calcaires marneux à Pholadomyes*.





417 Figure 6. A- Core picture of clays (facies F1b, lower offshore from the Vert-Le-Gr 4 well (VLG-4, 1525 m)). B- Core picture of  
418 marls (facies F2a, upper offshore) from the Vert-Le-Petit-4D well (VLP-4D, 1924 m). C- Oo-bioclastic grainstone (facies F3b and  
419 F3c, shoal) from the Vert-Saint-Denis-1 (VSD-1) core (1716 m). D- Intraclast grainstone (facies F4d, lagoon) from the Vert-  
420 Saint-Denis-1 (VSD-1) core (1694 m). E- Peloidal wackestone (facies F4a, lagoon from the Sergines-1 (SER-1) core (1656 m).

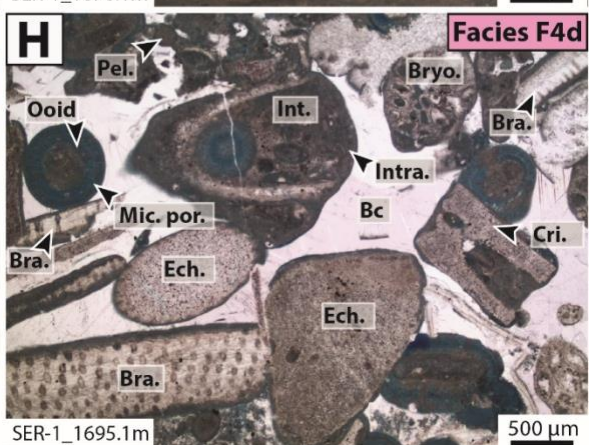
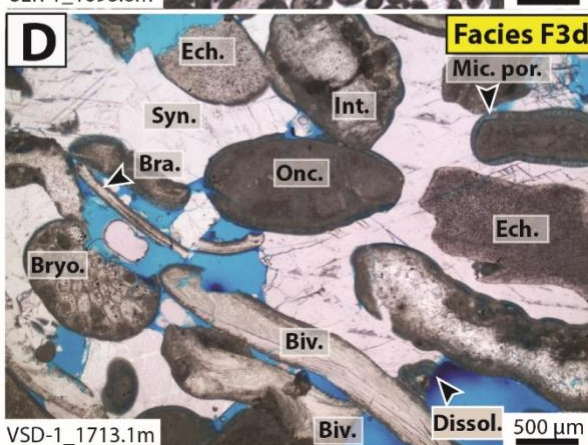
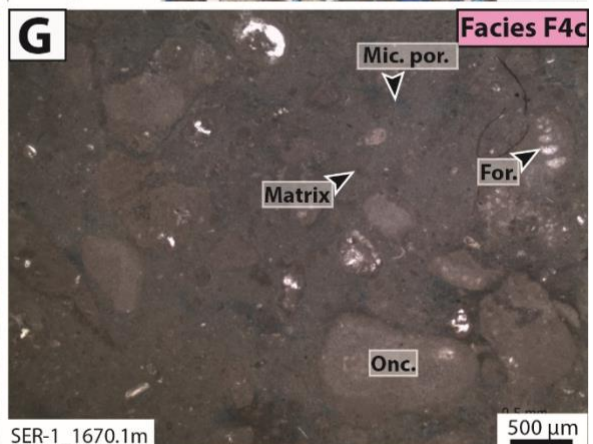
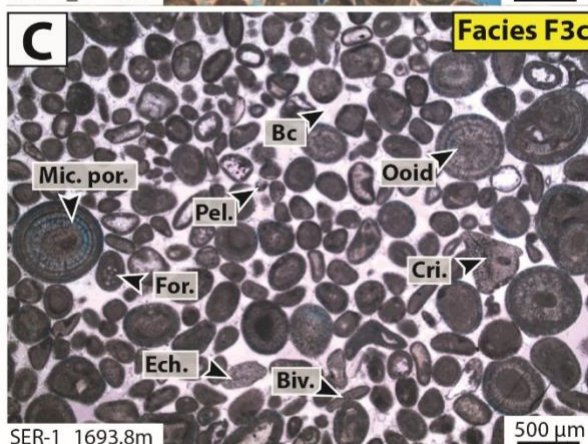
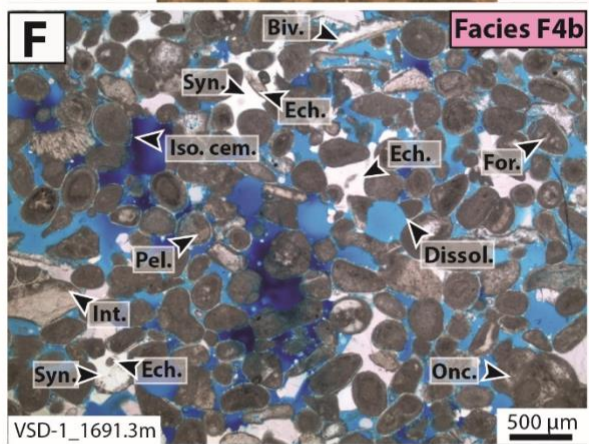
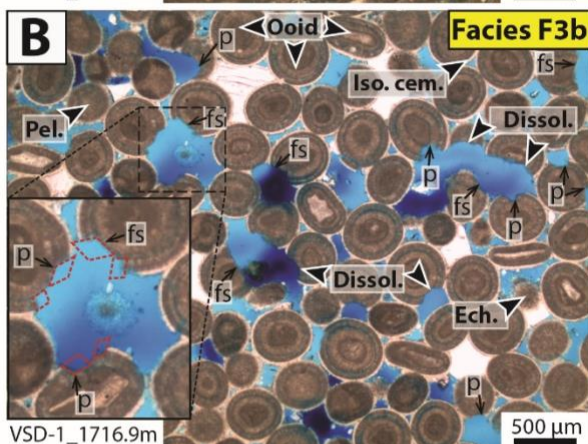
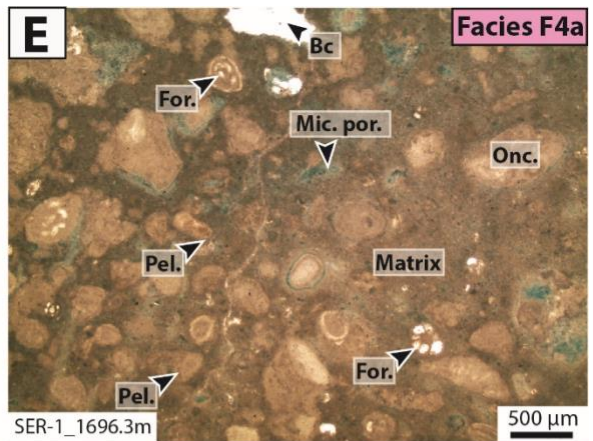
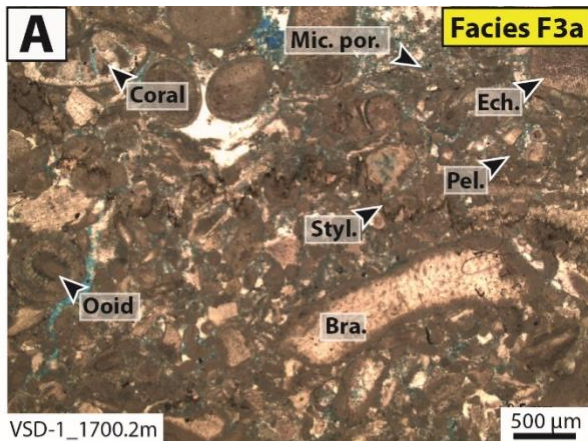
421

422 4.1.2 Alternating marls and mud-dominated limestones – Upper offshore environment (facies  
423 association FA2)

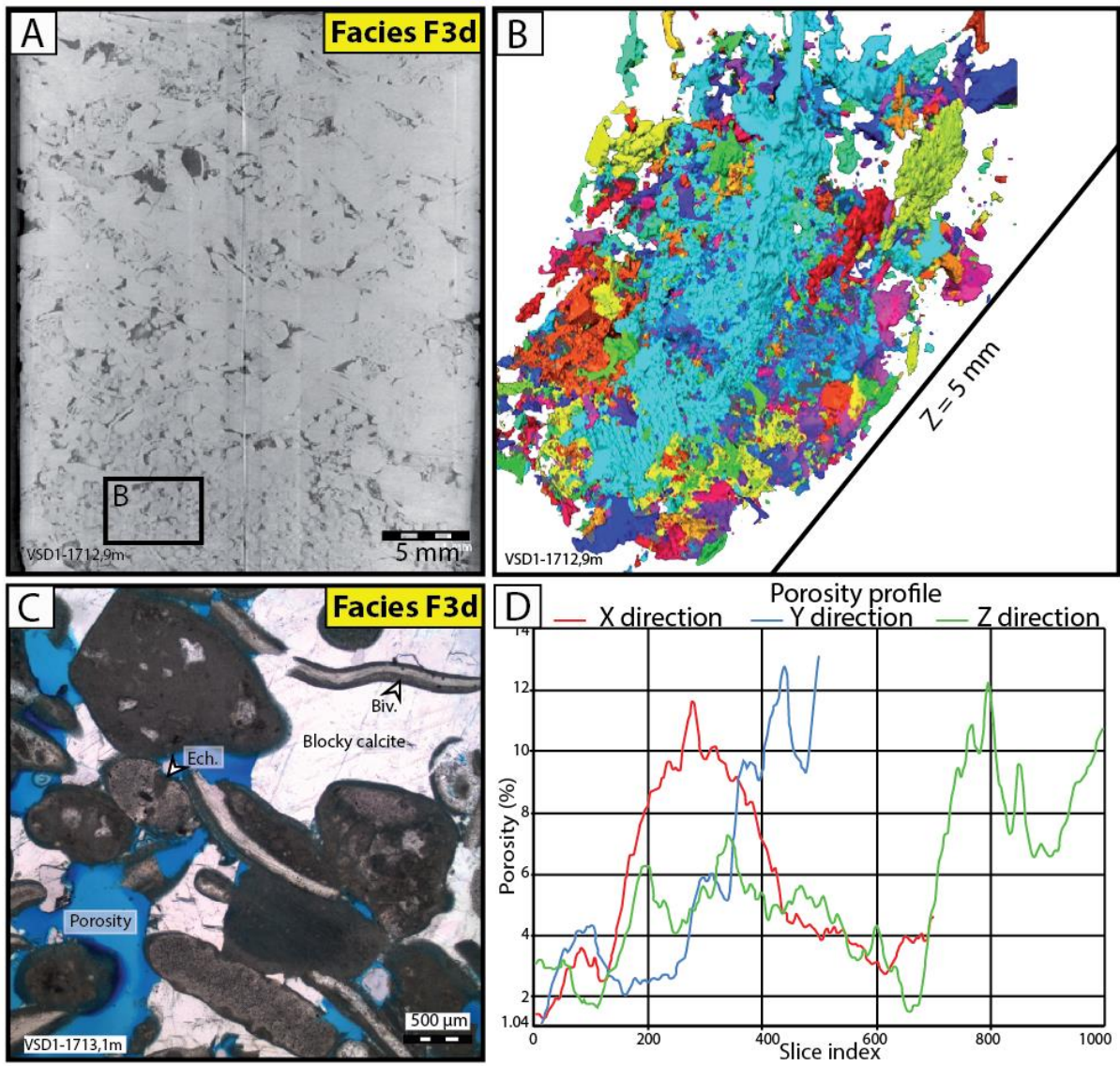
424 Description – This facies association contains three facies: (1) alternating marls and peloidal  
425 wackestone to packstone (facies F2a), (2) siliciclastic bioturbated packstone (facies F2b), and  
426 (3) marls with iron ooids (facies F2c), (Table 1, Figs 4, 5 and 6B). Wackestone to packstone  
427 layers in Facies F2a are composed of peloids, quartz, clays, foraminifera, bivalves, echinoderm  
428 fragments, crinoids and gastropods. The main characteristic of facies F2a is the clear  
429 alternations of marl layers and packstone layers (Table 1; Figs 5 and 6B). Facies F2b is roughly  
430 composed of the same bioclasts as the packstone of facies F2a but is more continuous  
431 vertically (Table 1; Fig 5). Facies F2c consists of marly deposits rich in iron ooids (Table 1). This  
432 facies also includes peloids and quartz grains. Facies F2c is present in all wells, forming a thin  
433 (metres-thick) and very well-defined marker across the Paris Basin. The ammonite fauna dated  
434 this layer from the late Callovian (*lamberti* Zone) to the early Oxfordian (*cordatum* Zone) (Vail  
435 et al., 1987; Gaumet, 1997; Collin et al., 2005).

436 Interpretation – Silty, marly or mud-dominated facies mark a calm environment. Some sandy  
437 or bioclast-rich layers are slightly graded with undulating draping lamination, suggesting  
438 storm-graded beds. The depositional zone is situated between the storm wave base and the  
439 fair-weather wave base, probably at a water depth of 20 to 40 m (Andrieu et al. (2016) and  
440 Brigaud et al. (2018), Table 1, Fig. 4). Considering the predominance of clays and marls in this  
441 facies, effective porosity is expected to be very low as is the effective permeability. This facies

442 association mainly occurred in the *Calcaires marneux à Pholadomyes* and *Dalle Nacrée*  
443 Formations (Fig. 4A)



445 *Figure 7. A- Peloidal packstone (facies F3a) with bioclasts and ooids displaying brachiopods (Bra.), peloids (Pel.), echinoderm*  
446 *fragments (Ech.), coral fragments (Coral). Porosity appears in blue and is low in this sample. Some micro-porosity (Mic. Por.)*  
447 *and styloliths (Sty.) are present. B- Low to moderately cemented ooid grainstone (Facies F3b) with rare peloids (Pel.), bioclasts*  
448 *such as echinoderm fragments (Ech.) locally form nucleus of ooid, isopachous cements (Iso. Cem.) are well-developed.*  
449 *Rhombohedral pore spaces are preserved as flat surfaces (fs) printing the dissolved dolomite rhomb faces or as points (p)*  
450 *printing the dissolved dolomite rhomb terminations (see arrows and zoom with possible location of dissolved dolomite rhombs*  
451 *in red dotted line). Dissolution (Dissol.). The porosity appears in blue due to the resin impregnation. C- Highly cemented*  
452 *oopeloidal (Pel.) grainstone (facies F3c) with echinoderm fragments (Ech.), crinoids (Cri.), bivalves (Biv.), foraminifera (For.).*  
453 *Micro-porosity (Mic. Por.) is present in ooids. Bc. : Blocky calcite. D- Rudstone to grainstone with bivalves (Biv.) and intraclasts*  
454 *(Int.), (facies F3d), oncoids (Onc.), echinoderm fragments (Ech.), brachiopods (Bra.), bryozoans (Bryo.), intraclasts and*  
455 *syntaxial overgrowth calcite cement around echinoderm fragments (Syn.). Porosity (in blue) is variable but can sometimes be*  
456 *very substantial. E- Peloidal (Pel.) wackestone/packstone with foraminifera (For.) and oncoids (Onc.), facies F4a. Blocky calcite*  
457 *(Bc) fills macroporosity. Micro-porosity is still present. F- Low to moderately cemented peloidal (Pel.) grainstone (facies F4b)*  
458 *with echinoderm fragments (Ech.), bivalves (Biv.), intraclasts (Int.) and oncoids (Onc.). Syntaxial overgrowth calcite cement*  
459 *around echinoderm fragments (Syn.) and isopachous cements (Iso. Cem.) reduce the porosity (in blue), while dissolution*  
460 *(Dissol.) enhances it. G- Oncolithic (Onc.) floatstone (facies F4c) with foraminifera (For.). H- Rudstone with intraclasts (Intra.),*  
461 *facies F4d, peloids (Pel.), echinoderm fragments (Ech.), crinoids (Cri.), brachiopods (Bra.) and bryozoans (Bryo.). Blocky calcite*  
462 *(Bc) is present, and micro-porosity (Mic. Por.) is current in the cortex of some grains. SER-1 corresponds to Sergines-1 well and*  
463 *VSD-1 to Vert-Saint-Denis-1 well.*  
464



Estimated permeability:  $k(x)= 70 \text{ mD}$ ,  $k(y)= 145 \text{ mD}$ ,  $k(z)= 135 \text{ mD}$

466

467 *Figure 8. A- Picture of the VSD1-1712,9m sample dominated by F3d facies (Rudstone to grainstone with bivalves and*

468 *intraclasts) B- 3D porosity representative volume elements (RVE) visualized using  $\mu$ CT scan at IFPEN on a mini-core sample*

469 *from the VSD1 core (1712,9m sample in measured depth). Each individual pore (not connected to others) is depicted in a*

470 *separate color. C- Thin section located in the VSD1 core, 20 cm beneath the sample, analyzed for 3D porosity (1712,9m*

471 *sample). D- Graph of the porosity distribution in each of the three directions in the VSD1-1712,9m sample. Each color*

472 *corresponds to a separate pore space.*

473

474 4.1.3 Ooids or bioclast-dominated facies – Shoal environment (facies association FA3)

475 Description – This facies association encompasses four grain-supported facies: (1) peloidal  
476 packstone with ooids and bioclasts (facies F3a), (2) low to moderately cemented ooid  
477 grainstone with bioclasts (facies F3b), (3) highly cemented ooid-peloidal grainstone with  
478 bioclasts (facies F3c) and (4) ooid-oncoidal rudstone to grainstone with bioclasts and  
479 intraclasts (F3d) (Figs 4, 5, 6C-E and 7A-D). Facies F3a is a packstone composed mainly of  
480 peloids, bivalves, echinoderm fragments, ooids and rare oncoids, coral fragments, intraclasts,  
481 foraminifera (in ooids), bryozoans and gastropods (Fig. 7A). Grain sizes range from 100  $\mu\text{m}$  to  
482 2 mm (Fig. 7). In this facies association, it is the only facies with a bounding matrix phase and  
483 it has a packstone texture. The matrix is unevenly distributed in the facies, and interparticle  
484 porosity can sometimes be observed. Facies F3a displays compaction textures, reducing the  
485 effective porosity and permeability (Table 1, Fig. 7A). Facies F3b is a grainstone mainly  
486 composed of 200–500  $\mu\text{m}$ -large ooids. Peloids are present, together with oncoids, intraclasts  
487 and bioclasts (bivalves, echinoderm fragments, foraminifera, bryozoans, and gastropods,  
488 Table 1, Figs 5, 6C, 7B). Large interparticle pores (100–500  $\mu\text{m}$ ) form the macroporosity  
489 considered as the effective porosity, contrary to the porosity under 10  $\mu\text{m}$  considered as  
490 microporosity and non-effective porosity. Early isopachous cements, typical of early marine  
491 cement, are present. This early cement limits mechanical compaction, maintaining large  
492 intergranular pore space with sharp borders. Limited blocky calcite zones are also present (Fig.  
493 7B). Locally, part of the ooids and blocky calcite have been dissolved, suggesting a late  
494 dissolution process. Rhombohedral pore spaces of about 500  $\mu\text{m}$  in size are locally observed,  
495 labelled as mouldic pores (Fig. 7B). Facies F3c is mainly composed of ooids, with common  
496 content of peloids, oncoids, bivalves, and rare intraclasts, echinoderm fragments,  
497 foraminifera, bryozoans, gastropods, and coral fragments. This facies is very similar to F3b,  
498 but differs with blocky calcite cement filling intergranular space (Fig. 7C). Only microporosity

499 in some ooids is present (Table 1, Fig. 7C, Fig. 7a). F3d is a grainstone to rudstone composed  
500 of common intraclasts, gastropods, bivalves, brachiopods, and echinoderm fragments, with  
501 rare ooids, peloids, oncoids, bryozoans and foraminifera (Fig. 7D). This facies was deposited  
502 in thin layers with millimetric bivalve and brachiopod shell fragments. Millimeter-sized blocky  
503 to syntaxial overgrowth calcite cement around echinoderm fragments fills the intergranular  
504 space. Dissolution forms 200  $\mu\text{m}$  to 2 mm pores (Fig. 7D). CT scan 3D models of the porous  
505 network show that, despite a high porosity value, pores are not well connected in facies F3d  
506 (Fig. 8B). At the microscale, this facies displays moderate porosity and moderate permeability  
507 around 100 mD. Porosities extracted from the CT scan have similar variations in all three  
508 directions, ranging from 2 to 12% (Fig. 8). Horizontal permeability is anisotropic with a  
509 minimum of 70 mD and a maximum of 145 mD. Vertical permeability is close to the maximum  
510 horizontal value (Fig. 8). This facies presents a good effective porosity and permeability  
511 overall. Still, it is less common than F3b in this facies association (Table 1).

512 Interpretation – The presence of echinoderms, brachiopods, or bryozoans suggests well-  
513 oxygenated water with normal salinity (Brigaud et al. 2009). Common sigmoid cross-bedding  
514 in sandwaves and grainstone/rudstone textures indicates shallow and high-energy wave-  
515 dominated conditions in an oolitic shoal complex (Fig. 4). Based on pore development  
516 observed in thin sections, two groups of facies have been distinguished. Facies F3a and F3c  
517 are considered to have low reservoir potential due to the presence of a mud-matrix, high  
518 compaction (F3a) and the development of highly blocky calcite (F3c). Facies F3b and F3d are  
519 the main reservoir facies in the shoal environment. Facies F3b is more common than F3d,  
520 which only appears locally in thin but porous and permeable layers. Rhombic pseudomorphs  
521 can be locally recognized by careful observations of the pore boundaries, either forming flat  
522 surfaces along ooids or forming points, printing the crystal terminations (Fig. 7B). Pores with



523 rhomb shapes suggest dissolution of dolomite in facies F3b, as already observed by Purser  
524 (1985), (Fig. 7B). The dolomite is entirely dissolved, while blocky calcite and clasts have been  
525 only partially affected by dissolution. Dissolution appears to be an essential process of  
526 porosity development in the reservoir. This facies association mainly occurred in the *Oolithe*  
527 *Blanche* Formation (Fig. 4A).

#### 528 4.1.4 Peloid to oncoidal facies – Lagoon environments (Facies association FA4)

529 Description – This facies association encompasses four grain-supported facies with peloid  
530 dominant non-bioclastic components: (1) peloidal wackestone to packstone with foraminifera  
531 and echinoderms (facies F4a), (2) low to moderately cemented peloidal grainstone (facies  
532 F4b), (3) oncoidal packstone to floatstone (facies F4c) and (4) rudstone with intraclasts (facies  
533 F4d) (Table 1, Figs 7E-H). Facies F4a is mainly composed of peloids, with common oncoids,  
534 foraminifera (presence of *Meyendorfina bathonica*), echinoderm fragments, bivalves and rare  
535 ooids, bryozoans, gastropods, brachiopods and coral fragments. Grain size ranges from 200 to  
536 800  $\mu\text{m}$ . This facies is mud-dominated, with a wackestone to packstone texture and it displays  
537 low effective porosity and permeability, mainly microporosity in the matrix between the  
538 grains (Table 1, Fig. 6E). Facies F4b is mainly composed of peloids but differs from facies F4a  
539 by the absence of a mud matrix. This facies has a grainstone texture and exhibits high effective  
540 porosity and permeability (Fig. 6F). Grain size varies from 100 to 400  $\mu\text{m}$ , displaying 50 to  
541 500  $\mu\text{m}$  pore sizes with very high microporosity. Cementation is directly related to the  
542 echinoderm content, around which syntaxial cement systematically develops. As echinoderm  
543 fragments are rare, cementation is not well developed in facies F4b (Fig. 6F). Local dissolution  
544 of grains improves the porosity of this facies. Facies F3c is mainly composed of oncoids (grain  
545 size from 100  $\mu\text{m}$  to 5 cm), with common peloids, and rare bivalves, foraminifera and  
546 gastropods. This facies is matrix-supported with a packstone to floatstone texture. No macro-

547 pores are observed in facies F4c, resulting in very low effective porosity and permeability  
548 (Table 1, Fig. 7G). Facies F4d is composed mainly of intraclasts, with common oncoids,  
549 bivalves, brachiopods and rare foraminifera, gastropods and green algae. Pores are rare due  
550 to calcite overgrowths (Table 1, Fig. 7H).

551

552 Interpretation – The dominance of peloid-oncoid dominated facies and the muddy matrix  
553 indicates low-energy environments, probably within a lagoon. As for the shoal environment,  
554 two groups can be distinguished in this facies association. A first group is composed of the  
555 non-porous and impermeable facies F4a and F4c (permeability from 0.1 mD to a few mD in  
556 the Vert-Saint-Denis-1 well). A second group displays high effective porosity and permeability  
557 and contains F4b (permeability from 0.5 mD to >1500 mD in the Vert-Saint-Denis-1 well).  
558 Facies F4d may belong to the first or second group depending on its degree of cementation.  
559 This facies association shows that, even in a sheltered environment like a lagoon, porous and  
560 permeable rocks are present and must be modeled. Petrographically, facies association FA4  
561 has a lower reservoir value than facies association FA3, but some local non-cemented granular  
562 facies (F4b) may form productive layers. This facies association mainly occurs in the *Calcaire*  
563 *de Comblanchien* Formation (Fig. 4A), dated as Late Bathonian by *Meyendorfina bathonica*  
564 (Thomas et al., 2021; Vincent et al., 2021).

565

Depositional environments and corresponding facies and/or facies association	Lithofacies	Non-bioclastic components	Bioclastic components	Energy and Depositional environment	Texture (Dunham, 1962)	Sorting and grain size	Porosity	Diagenesis	Reservoir potential
Lower Offshore, Palaeodepth >40 m (Facies association FA1 - Clays, marls)	F1a - Marls	Silts, clay	-	Very low energy, Lower Offshore	Mudstone	-	No effective porosity	-	Non-existent
	F1b - Clays	Clay	-	Very low energy, Lower Offshore	Mudstone	-	No effective porosity	-	None-existent
Upper Offshore, Palaeodepth 20–40 m (Facies association FA2 - Alternating marls and mud-dominated limestones)	F2a - Alternating marls and peloidal wackestone to packstone	Peloids (A), Quartz (C), Clay (C)	Foraminifera (F), Bivalves (F), Echinoderm fragments (C), Crinoids (R), Gastropods (R)	Low to moderate energy, Upper Offshore	Packstone, Wackestone	Poorly sorted	No macroporosity / very low microporosity in micritic matrix	Micritization, early microsparitic cement, stylolithization, pyrite	Unusable
	F2b - Siliciclastic bioturbated packstone	Peloids (A), Quartz (C), Clay (C)	Foraminifera (F), Bivalves (F), Echinoderm fragments	Low to moderate energy, Upper Offshore	Packstone	Poorly sorted	Sparse intraparticle macroporosity, microporosity	Micritization, early microsparitic cement,	Unusable

			(C), Crinoids (R), Gastropods (R)				y in micritic matrix	stylolithization, pyrite	
	F2c - Marls with iron ooids	Peloids (A), Ferruginous ooids (C), Quartz (C), Clay (C)		Low to moderate energy, Upper Offshore	Wackestone, Mudstone	Poorly sorted	No macroporosity / microporosity in micritic matrix		Unusable
Shoal Environment - Shoreface, Palaeodepth <20 m (Facies association FA3 - Ooids or bioclastic-dominated facies)	F3a - Peloidal packstone with ooids and bioclasts	Ooids (C), Peloids (C), Oncoids (C), Intraclasts (R)	Bivalves (F), Echinoderm fragments (F), Crinoids (F), Gastropods (C), Brachiopods (C), Bryozoans (R), Coral fragments (R), Foraminifera (R), Algae (R)	High energy, Shoal	Packstone	Poorly sorted	Sparse interparticle porosity. Mouldic macroporosity in dissolved bioclasts. Microporosity in ooid cortex	Syntaxial cement, micritization, recrystallization, stylolithization, frequent concavo-convex contacts between grains, dissolution of bioclasts	Low
	F3b - Low to moderately cemented ooid grainstone with bioclasts	Ooids (A), Peloids (C), Oncoids (VR), Intraclasts (VR)	Bivalves (C/R), Echinoderm fragments (R), Foraminifera (in ooids)	High energy, Shoal	Grainstone	Very well sorted	Interparticle macroporosity, mouldic macroporosity, intraparticle microporosity	No cement to local blocky calcite, grain micritization. Isopachous cement. Concavo-	Very high

			(R), Bryozoans (R), Gastropods (R)				y (oid cortex)	convex contacts can appear on some grains, mostly when isopachous cement is not observed. Some styloliths. Local syntaxial cement growth around echinoderm fragments. Dolomite dissolution	
	F3c - Highly cemented ooid- peloidal grainstone with bioclasts	Ooids (A), Peloids (A/C), Oncoids (C), Intraclasts (R)	Bivalves (C/R), Echinoderm fragments (C/R), Foraminifer a (R), Bryozoans (R), Gastropods (R), Coral fragments (R)	High energy, Shoal	Grainstone	Well sorted	Rare interparticle pores. Microporosit y is present in ooid cortex.	Extensively developed blocky calcite. Recrystallized bioclasts. Syntaxial cement growth near echinoderms and non- isopachous cements.	Low to very low

	F3d - Ooid-oncoidal rudstone to grainstone with bioclasts and intraclasts	Intraclasts (C), Ooids (R), Peloids (R), Oncoids (VR)	Brachiopods (F), Bivalves (F), Gastropods (C), Echinoderm fragments (C), Bryozoans (R), Foraminifera (R)	High energy, Shoal	Grainstone /Rudstone	Very poorly sorted	Variable intraparticle porosity depending on cementation. Rare microporosity in ooid cortex.	Developed blocky syntaxial cement around echinoderm, recrystallized bioclasts, isopachous cement around most grains.	High
Lagoon environments, Palaeodepth <20 m (Facies association FA4 - Peloid to oncoidal facies)	F4a - Peloidal wackestone/packstone with foraminifera and echinoderms	Peloids (A), Oncoids (C), Ooids (VR)	Foraminifera (F) (presence of <i>Meyendorfi na bathonica</i> ), Echinoderm fragments (C), Bivalves (C), Bryozoans (R), Gastropods (R), Brachiopods (R), Coral (VR)	Low to moderate energy, protected environments, Lagoon	Wackestone / Packstone	Poorly sorted	Low to absent macroporosity, microporosity in micritic matrix and dissolved grains	Very local syntaxial cement growth near echinoderms, matrix recrystallization, sparse dissolution, stylolithization	Low

	F4b - Low to moderately cemented peloidal grainstone	Peloids (A), Oncoids (C), Ooids (C/R), Intraclasts (R)	Bivalves (C), Echinoderm fragments (R), Bryozoans (R), Gastropods (R), Foraminifera (C)	Moderate energy protected environments, Lagoon	Grainstone	Well sorted	High macroporosity within pore throats, excellent connectivity. Few grains with intraparticle porosity (recrystallized bioclasts and ooids)	Recrystallized bioclasts, moderate local syntaxial cement growth near echinoderms and irregular cements around the grains, local dolomite dissolution	High
	F4c - Oncolitic floatstone	Oncoids (A), Peloids (C)	Bivalves (R), Foraminifera (R), Gastropods (VR)	Low to moderate energy, protected environments, Lagoon	Floatstone	Very poorly sorted	Microporosity in matrix	Recrystallized bioclasts	Very low
	F4d - Rudstone with intraclasts	Intraclasts (A), Oncoids (C),	Bivalves (C), Brachiopods (C), Foraminifera (R), Gastropods (VR), Algae (R)	Moderate energy, protected environments, Lagoon	Grainstone /Rudstone	Very poorly sorted	High macroporosity within pore throats (rarer than in F4c). Few grains with intraparticle porosity (recrystallized bioclasts and ooids)	Non-isopachous and sporadic dog tooth cement around some grains. Extensive syntaxial cement growth around few big echinoderm fragments, pyrite, local	Low to medium (depends on the development of blocky calcite growth)

								dolomite dissolution	
--	--	--	--	--	--	--	--	-------------------------	--

566

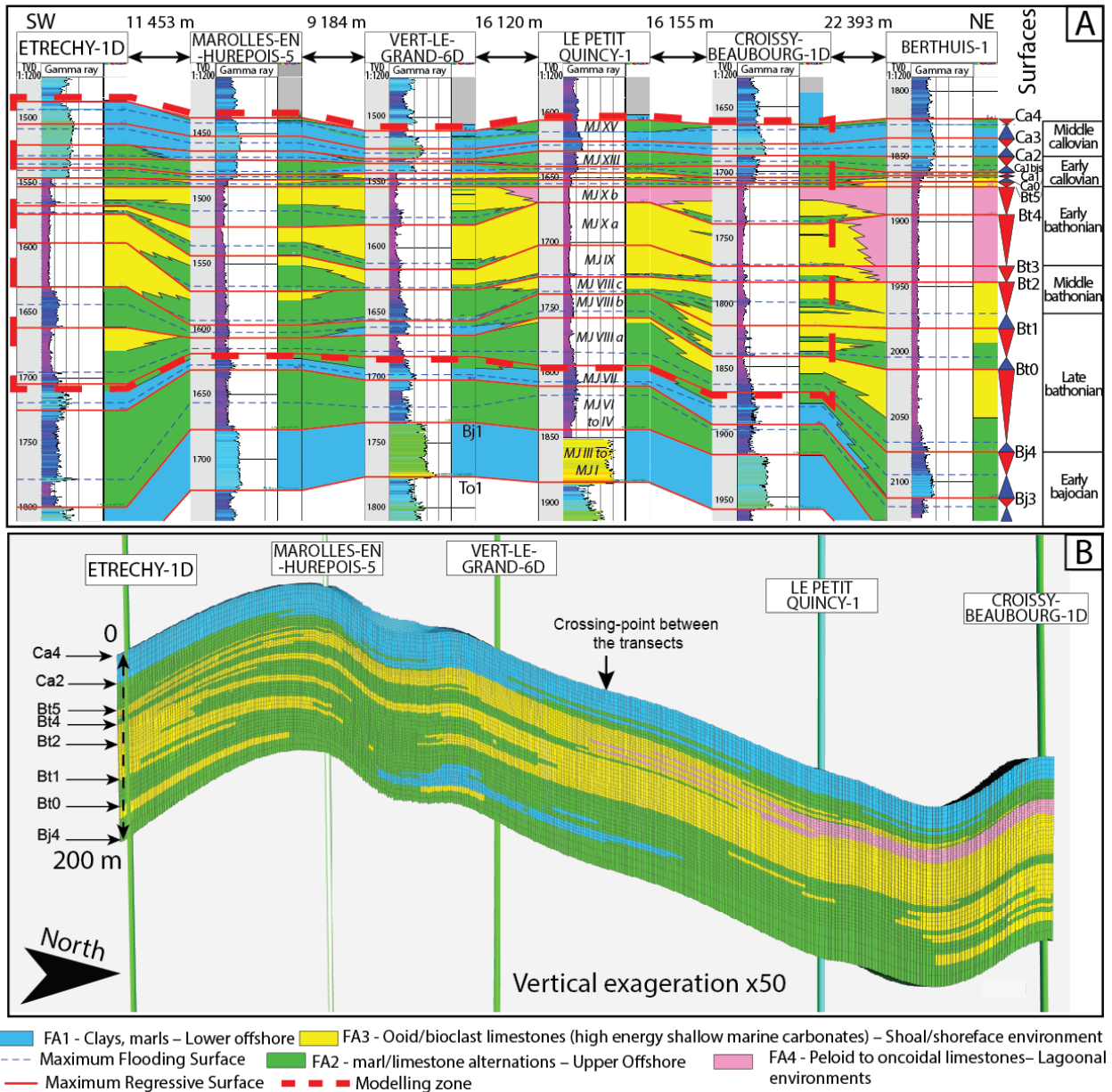
567

Table 1: Facies table for the facies associations with sorted samples from cores. VR = Very rare < 5% R = Rare < 10%; C = Common 10 – 20%;

568

F = Frequent 20 – 50%; A = Abundant > 50%





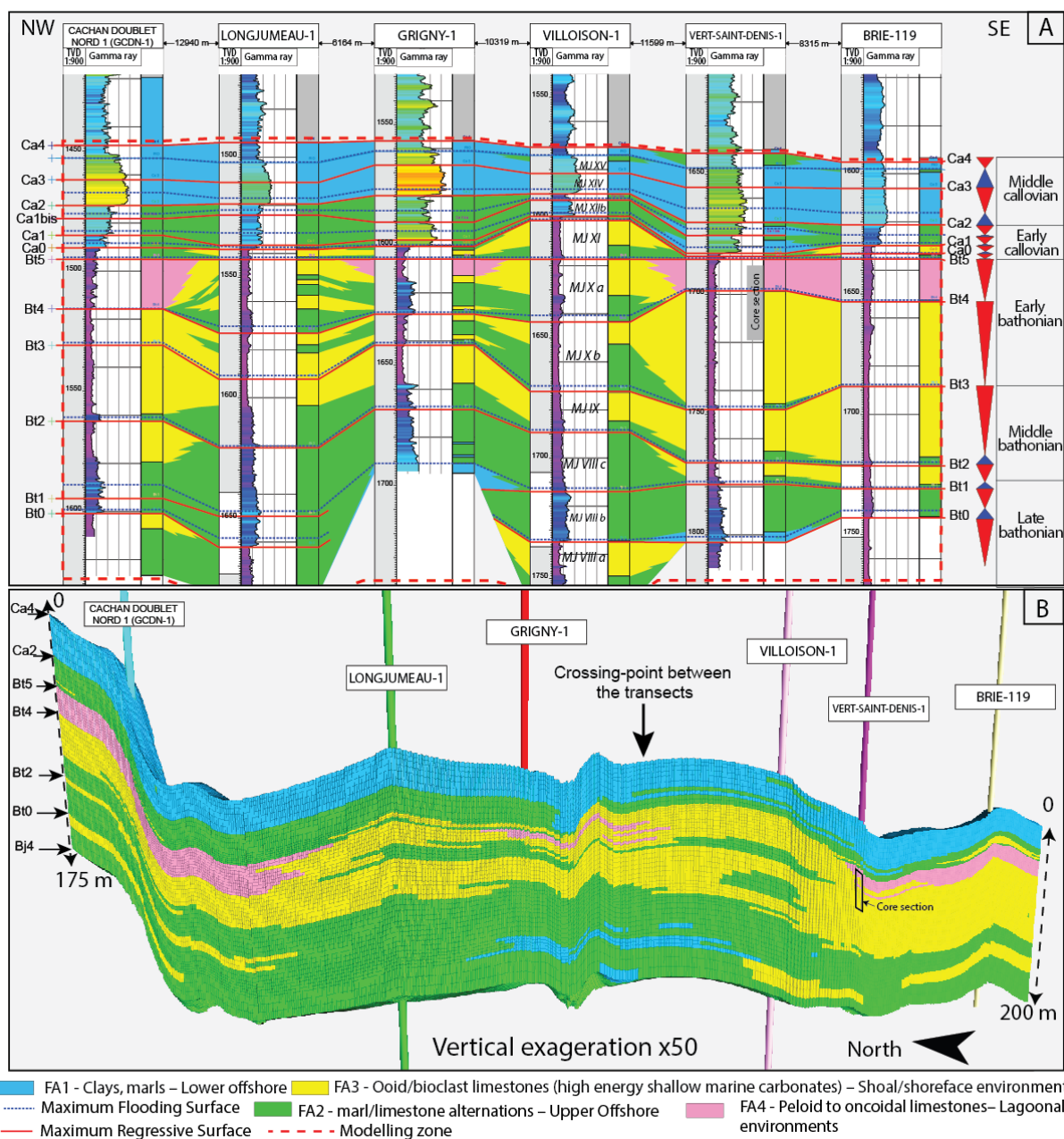
571

572 Figure 9. A- Stratigraphic cross-section from SW to NE, between the Etrechy-1D well and the Berthuis-1 well. This cross-section  
 573 is located in fig. 1B. Each well is represented with depth, gamma ray values, and facies. Berthuis-1 is not in the model zone  
 574 but is a reference well for the stratigraphic sequence in the Paris Basin (Gaumet, 1997). B- Same stratigraphic cross-section  
 575 as A, extracted from the 3D model in Petrel© (except Berthuis-1 well). This section represents the final facies model with well  
 576 locations and stratigraphic surfaces (vertical exaggeration is set to 50).

577 The SW–NE stratigraphic cross-section from the Etrechy-1D to Berthuis-1 wells allows us to  
 578 reconstruct vertical and lateral facies heterogeneity (Fig. 9A). The Berthuis-1 well is located

579 outside the area modeled in this study. It allows to correlate the stratigraphic sections of the  
580 model with the facies and biostratigraphic attribution of the Coulommès oil field (Gaumet,  
581 1997). The Early Bajocian sequences beneath Bj4 are not modeled. They exhibit alternating  
582 marls, clays, and packstones (Fig. 9B). Between Bj4 and Bt2 (sequences VIIIa, VIIIb, VIIIc), the  
583 facies associations described on wells mainly correspond to marls and packstones of the upper  
584 offshore environment (facies association FA2), and locally oolitic deposits (facies association  
585 FA3) at the Croissy-Beaubourg-1D and Etrechy-1D wells. In the Vert-le-Grand-6D well, oolitic  
586 facies are absent, and clay layers (lower offshore) are predominant (Fig. 9). Between Bt4 and  
587 Bt2 (sequences MJIX and MJXa), the dominant facies along the cross-section are ooid  
588 limestones (facies association FA3). Marl-limestone alternations are still present at the base  
589 of each sequence, corresponding to the flooding of the platform (Fig. 9). In the western part  
590 of the cross-section (between the Etrechy-1D and Vert-le-Grand-6D wells), alternating marls  
591 and limestones (facies association FA2) dominate and form a trench (Fig. 9). These marl-  
592 limestone deposits vastly reduce the reservoir properties of the area. Between Bt5 and Bt4  
593 (sequence MJXb), the *Calcaire de Comblanchien* Formation (facies association FA4) is present  
594 between the Le Petit Quincy-1 well and the Croissy-Beaubourg-1D well between Bt5 and Bt4  
595 surfaces (Fig. 9B). This formation is thicker towards the Berthuis-1 well, where the oolitic shoal  
596 facies (facies association FA3) passes laterally into lagoonal facies (from Bt2 to Bt5 surfaces).  
597 West of the lagoon (west of the Le Petit Quincy-1 well), facies are dominated by oolitic  
598 deposits (at Vert-le-Grand-6D). In sequence MJXb, westwards, the dominant facies association  
599 is alternating marl/packstone (upper offshore environment: facies association FA2),  
600 corresponding to the distal part of the carbonate ramp. In sequence MJXb, oolitic limestones  
601 correspond to a shoal environment. Between Ca2 and Bt5 surfaces (sequences MJXc to  
602 MJXIII), the *Dalle Nacrée* formation consists mainly of alternating marl and limestone, with

603 local ooid or bioclastic limestones at Berthuis between Bt5 and Ca1 or at Vert le Grand and Le  
 604 Petit Quincy between Ca2 and Ca0. The cross-section shows the homogeneity of the cap rock  
 605 (middle Callovian deposits) in the section (Fig. 9). From Ca4 to Ca2 surfaces, deposits are  
 606 mainly composed of clays (lower offshore facies association FA1).  
 607 The second transect illustrates the facies architecture between Cachan in the northwest and  
 608 the historic oil field of Chailly-en-Bière in the southeastern part of the study area (Fig. 1B, Fig.  
 609 10).



610

611 *Figure 10. A- Stratigraphic cross-section from NW to SE, between Cachan Nord-1 well and BRIE-119 well. This cross-section is*  
612 *located in fig. 3B. Each well is represented with depth, gamma ray values and facies. B- Same stratigraphic cross-section as A,*  
613 *extracted from the 3D model in Petrel®. This section represents the final facies model with the location of wells and*  
614 *stratigraphic surfaces (vertical exaggeration is set to 50). TVD: True Vertical Depth.*

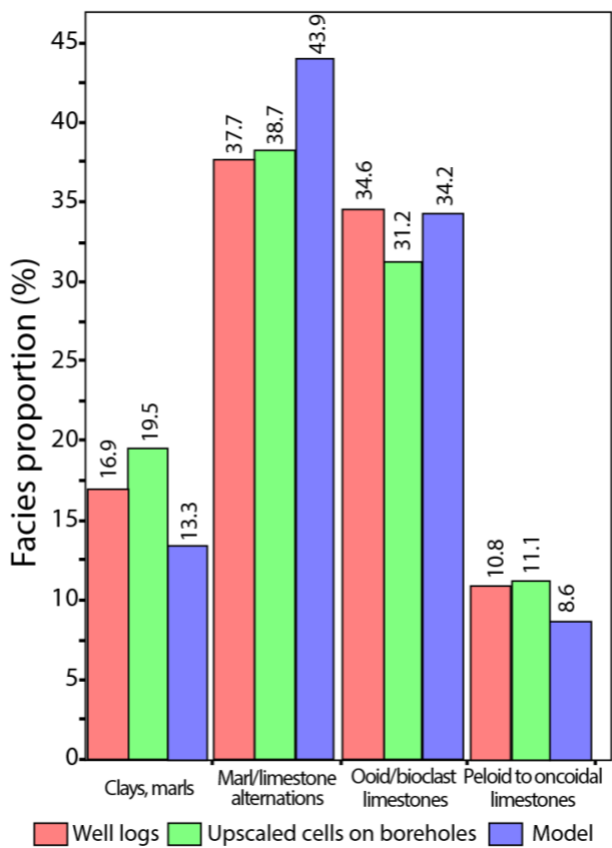
615 Below the Bt2 surface, the facies are mainly marl-limestone alternations (facies association  
616 FA2), with local development of oolitic deposits just below maximum regressive surfaces Bj4,  
617 Bt0, and Bt2. Some clay deposits typical of a lower offshore environment (facies association  
618 FA1) are also present just above the Bj4, Bt0, and Bt1 surfaces in the Grigny-1 well,  
619 corresponding to maximum flooding surfaces (Fig. 10A-B). Between Bt4 and Bt2, although the  
620 reservoir is mainly composed of oolitic facies, alternating marl and limestone are present at  
621 the base of the sequences (MJIX and MJXa sequences) between Longjumeau-1 and Villoison-  
622 1 wells (Fig 10). These marly layers are thinner in the north-west and south-east of the study  
623 area (Fig. 10). In sequence MJXb deposits, marl-limestone alternations (facies association FA2)  
624 pass vertically into oolitic grainstone (facies association FA3) in the Longjumeau-1, Villoison-1  
625 and Grigny-1 wells (Fig. 10). A lagoon (facies association FA4) developed at the top of the  
626 sequence in the Grigny well. In the western and northern parts of the study area, sequence  
627 MJXb deposits are composed exclusively of lagoonal facies. In this sequence, the oolitic  
628 limestones form an oolitic shoal or barrier, protecting sheltered lagoons located around the  
629 Cachan-1, Grigny-1, and Brie-119 wells. This cross-section exhibits a similar architecture for  
630 the middle Callovian deposits as the E–W cross-section (Fig. 9), ranging from Ca0 to Ca4. An  
631 exception is found at the base of the lower Callovian deposits near Brie-119 and Villoison-1,  
632 with the oolitic facies corresponding to the reservoir of the *Dalle Nacrée* formation (Javaux,  
633 1992). These deposits are usually framed between Bt5 and Ca1.

634 The third-order depositional sequences described displaying a regressive stacking pattern.  
635 Facies pass upwards from (1) lower offshore marls or clays into (2) upper offshore

636 marl/limestone alternations, (3) ooid limestones, and (4) lagoonal peloid to oncoidal facies  
 637 (Figs 9 and 10). Sequences never contain the complete succession of facies, and most of them  
 638 form vertical successions passing upwards from marl/limestone alternations into ooid  
 639 limestones. Sequences MJIX, MJXa and MJXb are the most complete sequences with a vertical  
 640 succession passing upwards from marl/limestone alternations into ooid limestones and peloid  
 641 to oncoidal facies (Figs. 9 and 10).

642

643 **4.3 Facies modeling**



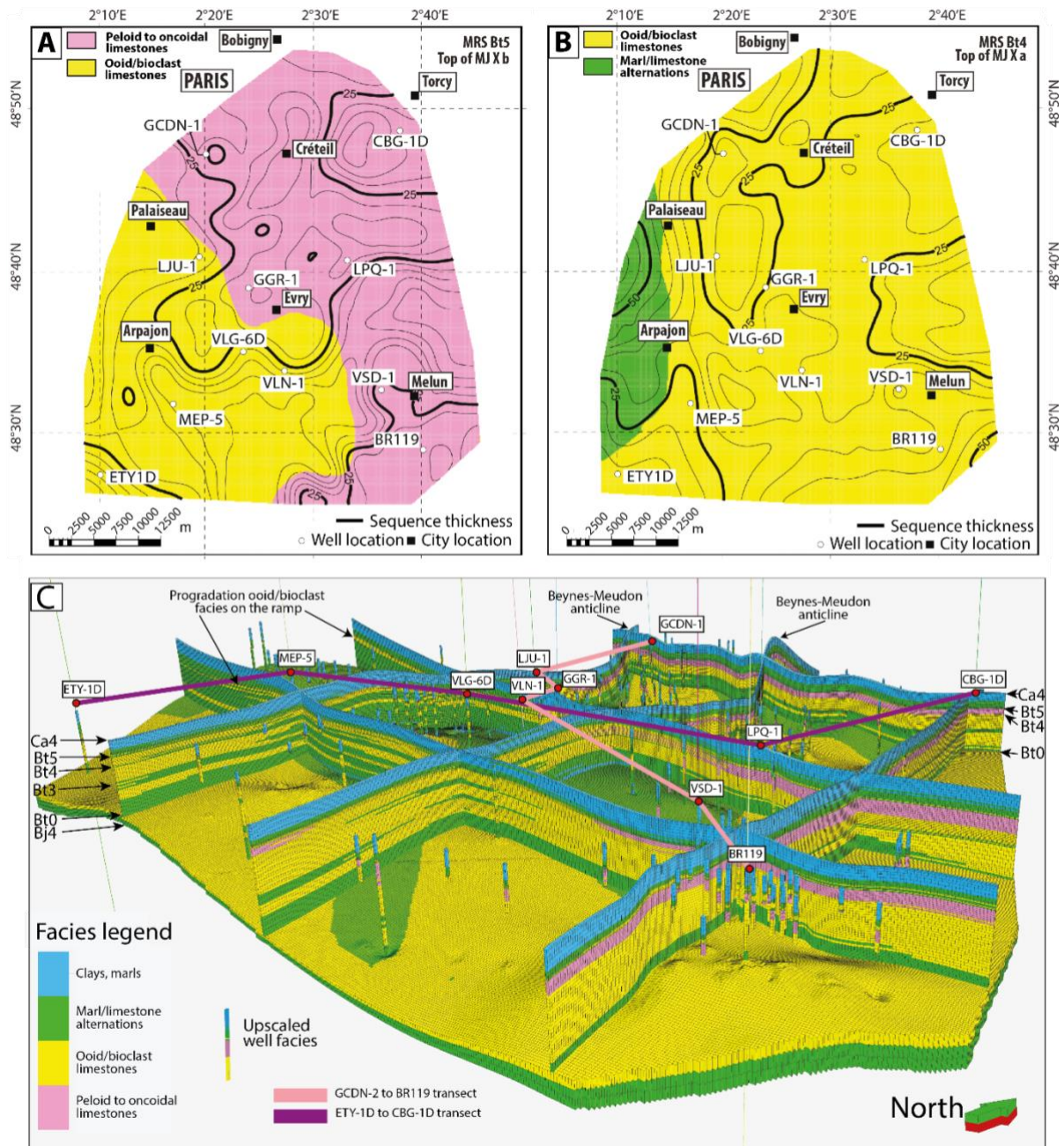
644

645 *Figure 11. Facies association proportion in well logs, in upscaled cells along each well and in the entire model (12.2 million*  
 646 *cells).*

647 Using the two cross-sections and a view of the upscaled cells in each well, facies associations  
 648 in each stratigraphic sequence have been computed using the “truncated Gaussian with  
 649 trends” algorithm. This algorithm is well suited for modeling large-scale ordered facies

650 progradation and retrogradation, defining transgressive and regressive systems tracts  
651 (Brigaud et al., 2014b). For each zone, this algorithm requires a workflow to be followed  
652 (Brigaud et al., 2014a): (1) choose the facies and check the facies order, (2) set up the  
653 depositional geometry, i.e., edit the transition lines between the facies (boundaries of the  
654 facies belts), and (3) decide on the variogram ranges (spatial extension of facies belts) and  
655 variances (degree of interfingering between facies belts). The “truncated Gaussian with  
656 trends” algorithm is used to model the evolution of the depositional system in time and space  
657 in each zone. Detailed cross-sections and palaeogeographic maps from hard data (e.g., facies  
658 in wells) at the bottom and base of each sequence are used to design facies trends and honor  
659 hard data from each well. To control the quality of facies modeling, we compared the facies  
660 association proportion in wells to ensure they are statistically compatible (Fig. 11) with the  
661 percentage of each facies association in the upscaled cells in the wells and in the entire grid.  
662 In well logs, facies association content is very homogeneous: clays (facies association 1) =  
663 16.9%; marl/limestone alternations (facies association 2) = 37.7%; ooid limestones (facies  
664 association 3) = 34.6% and peloid to oncoidal facies (facies association 4) = 10.8%. Facies  
665 contents (in percentage) in upscaled cells and in the entire model are similar to well logs,  
666 except for the marl/limestone alternations in the entire model, which seem to be over-  
667 estimated (43.9%), at the expense of clays (facies association FA1). Since these rocks are not  
668 considered reservoirs, no impact is expected on the reservoir location. Facies evolution can  
669 be observed in 2D maps or in a 3D block-diagram along the model (Fig. 12). It appears that in  
670 the modeled area, the early–late Callovian deposits act as cap rock for the reservoir, with the  
671 partial exception of the Brie region, where some ooid limestones are present (Fig. 12). In the  
672 north-western area, the anticline structure of Beynes-Meudon forms a major structural  
673 feature of the geothermal reservoir (in the Cachan area). The ramp was deepening westward

674 as attested by the progressive transition from the muddy lagoon and ooid shoals (facies  
675 associations FA3 and FA4) to upper offshore marl-limestone alternations (facies association  
676 FA2) (Fig. 12). The lagoonal facies association is mainly present in the eastern and northern  
677 parts of the model, and it progrades westward in sequence MJXb. Deposits of sequences MJIX  
678 and MJXa form a good reservoir in most of the study area. They are mainly composed of ooid  
679 limestones, with some marl and limestone alternations at the bottom of the sequences. The  
680 reservoir facies passes into marl-limestone alternations in the western part of the study area  
681 (Fig. 12 B, C). Below the Bt2 surface, the likelihood of encountering reservoir facies is low,  
682 except locally in the eastern part (Fig. 10), with more distal deposits ranging from marls to  
683 clays.

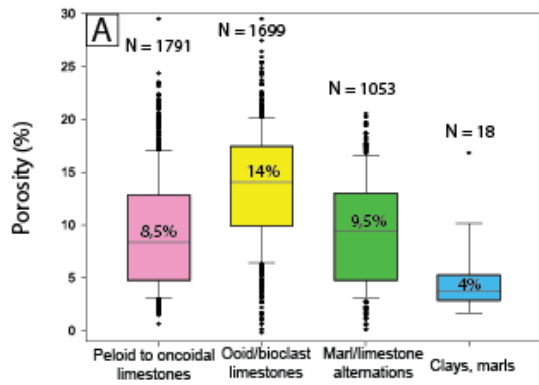


684  
 685 *Figure 12. A- Facies map at the top of Bt5 maximum regressive surface with the thickness (black line) of the sequence MJXb*  
 686 *deposits. B- Facies map at the top of Bt4 maximum regressive surface with the thickness of sequence MJXa deposits. C- View*  
 687 *of the entire 3D model with cross-sections generated by Petrel© showing facies association architecture. Facies association is*  
 688 *upscaled in each well. Only the bottom three layers (of 52 layers) are displayed.*

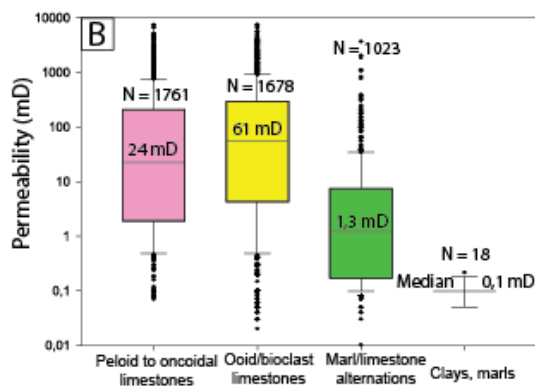
689 **4.4 Petrophysical characteristics**



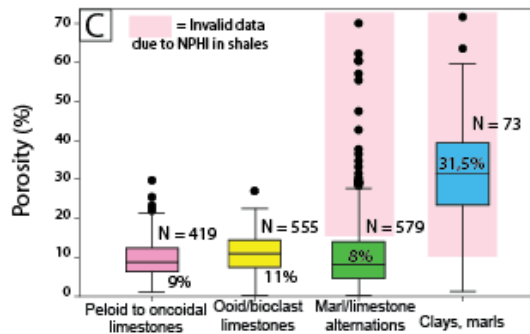
Mini-core porosity sorted by facies association



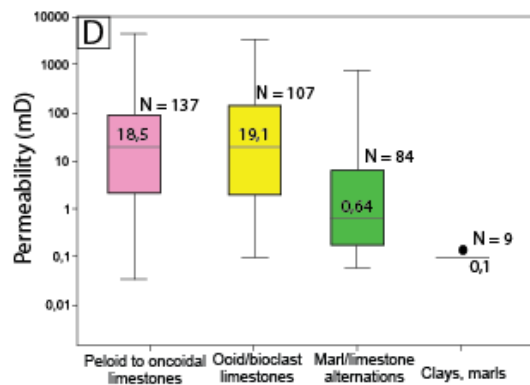
Mini-core permeability sorted by facies association



Mini-core and NPHI log porosity upscaled data sorted by facies association



Mini-core and  $k_{SDR}$  log permeability upscaled data sorted by facies association



691 *Figure 13. A- Mini-core porosity sorted by facies association. B- Mini-core permeability sorted by facies association. C- Mini-*  
692 *core and NPHI log porosity upscaled data sorted by facies association. Note that values differ widely between A and C in the*  
693 *marl/limestone alternations and clay facies associations. This is a known phenomenon of uncalibrated Neutron Porosity (NPHI)*  
694 *data in shales (Serra, 1979). D- Mini-core and Schlumberger Doll Research (SDR) permeability upscaled data sorted by facies*  
695 *association. The line inside the box is the median, and the top and base of the box correspond to the 25 and 75% quartiles.*  
696 *The horizontal bars represent the 5% (for the bottom bar) and the 95% (for the upper bar) of the data range. The dots represent*  
697 *the data out of range.*

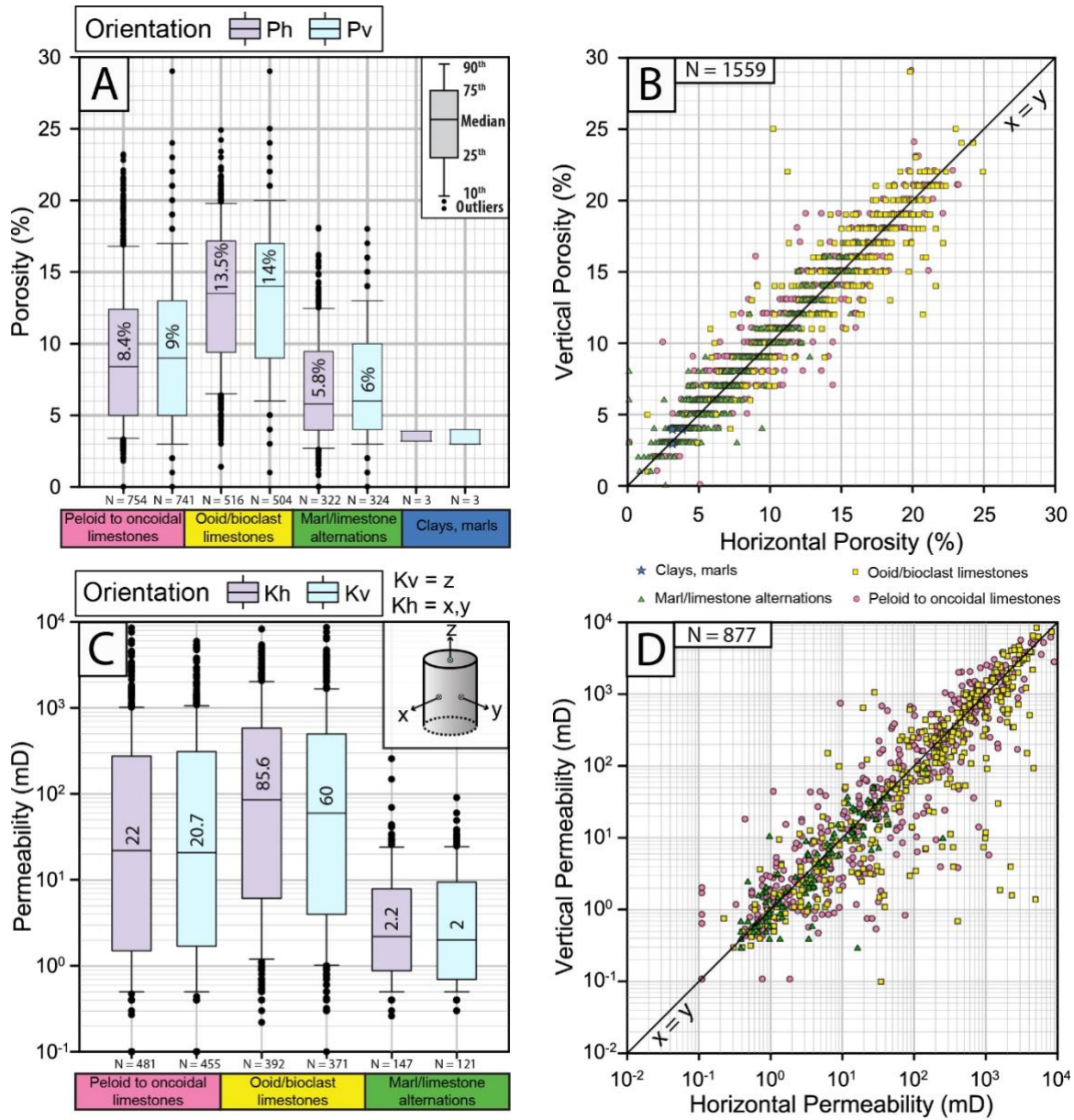
698 The porosity measured on mini-cores ranges between 0% and 39% (Fig. 13A). The best  
699 porosities are found in ooid limestones (3rd quartile at 17%). However, they may also be  
700 particularly low (<5%, Fig. 13A). In ooid limestones, the median of mini-core data indicates  
701 14% porosity confirming that these facies are of good reservoir quality (Fig. 13A). The lagoonal  
702 facies have lower median porosity (8.5%), but may locally display better porosity values, up to  
703 25% (Fig. 13A). Marl-limestone alternations have a better median porosity than peloid to  
704 oncoidal limestones (median of 9.5%, Fig. 13A). Clays/marls have the lowest effective  
705 porosities (median of 4%, Fig. 13A). Note that few data are available for the clayey/marly  
706 facies (N = 18, Fig. 13A). The marl/limestone alternation and clay/marl facies present in the  
707 upper and lower offshore deposits are less porous overall and considered as non-reservoir or  
708 cap rocks.

709 The permeability measured on mini-cores ranges between 0.01 mD and 8783.5 mD (Fig. 13B).  
710 Permeability values of lagoonal and oolitic limestones present very large ranges from 0.01 mD  
711 to 8711 mD for the lagoonal limestones and from 0.01 mD to 8783.5 mD for the oolitic  
712 limestones (Fig. 13B). The median value in oolitic limestone is 61 mD. In contrast, the median  
713 value of permeability in lagoonal facies is 24 mD, showing that these two sedimentary facies  
714 are of good reservoir quality (Fig. 13B). Marl-limestone alternations and clays have  
715 significantly lower permeabilities (median of 1.3 mD and 0.1 mD, Fig. 13B).

716 NPHI logs are known to be unrealistic in marls and clayey deposits if treated for limestone  
717 porosities (Serra, 1979). Mini-core porosity never exceeds 20%, whereas the 4<sup>th</sup> quartile has  
718 an unrealistic value of 28% for marl-limestone alternation (Fig. 13C). Porosity larger than 10%  
719 in clayey deposits and larger than 15% in marl-limestone alternations has been filtered by data  
720 analysis during modeling (Fig. 13C). Upscaled porosity of ooid limestones in wells is lower  
721 (median at 11%, Fig. 13C) than mini-core porosity and porosity of the lagoonal facies has  
722 similar porosity in the upscaled wells as mini-core porosity (median value of 9%, Fig. 13C).

723 The upscaled permeabilities range between 0.1 mD and 4000 mD (Fig. 13D). The lagoonal and  
724 oolitic limestone permeabilities (mini-cores and  $k_{SDR}$ ) are similar (median at 18.5 mD and  
725 19.1 mD respectively, Fig. 13D). Marl-limestone alternations and clays have significantly lower  
726 upscaled permeability values (median of 0.64 mD and 0.1 mD).

727 Horizontal and vertical porosity and permeability are positively correlated, except for a few  
728 samples that reveal larger vertical permeabilities than horizontal ones (Fig. 14).



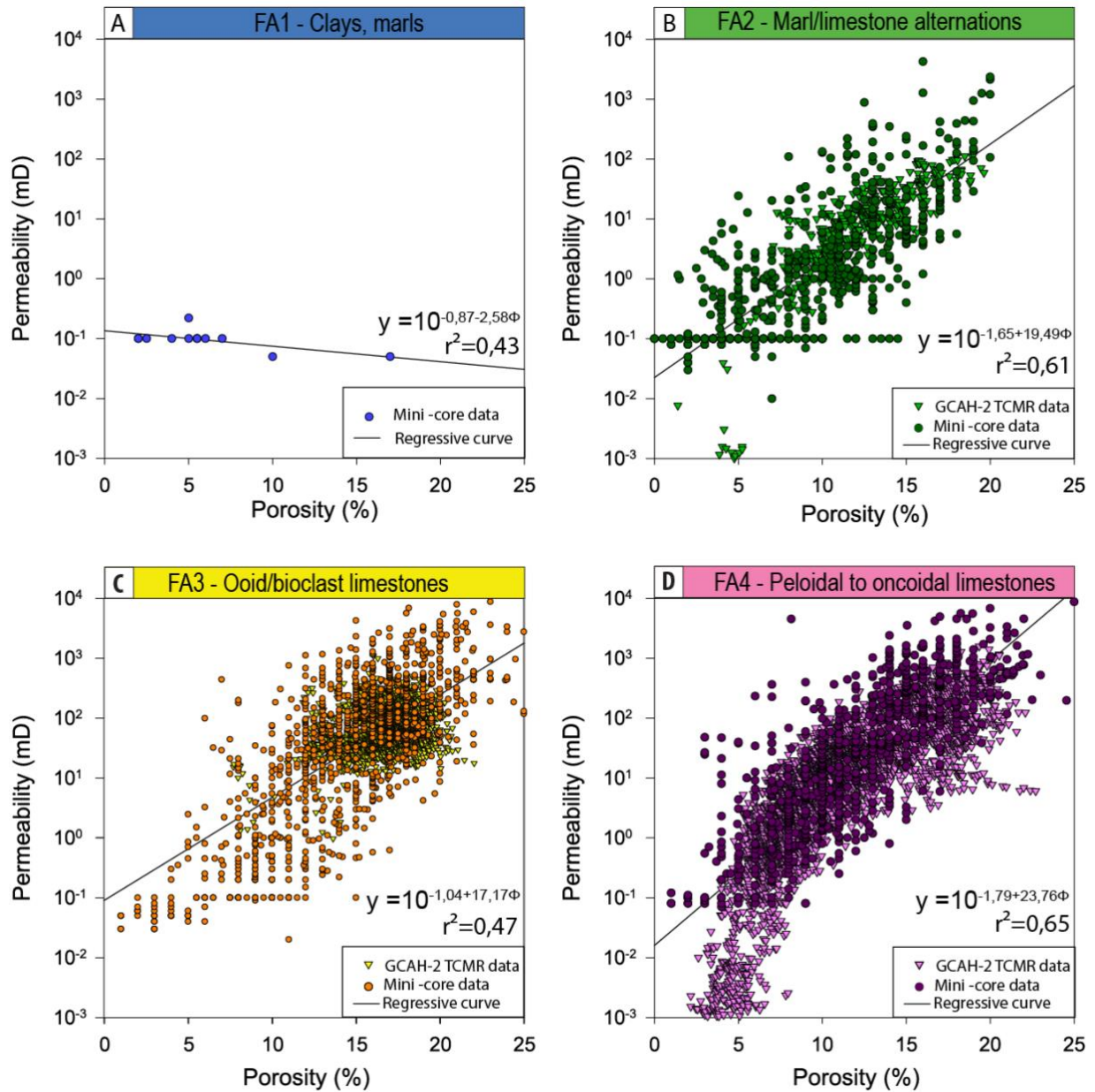
729

730 *Figure 14. A- Vertical (Pv) and horizontal (Ph) porosity distribution across each facies association. B- Porosity distribution in*

731 *vertical and horizontal directions. C- Vertical (Kv) and horizontal (Kh) permeability distribution across each facies association*

732 *(excluding clays, where no data could be found). D- Permeability distribution in vertical and horizontal directions.*

733



734

735 Figure 15. Porosity vs. permeability mini-core data and borehole (GCAH-2) well-logs (TCMR and  $K_{SDR}$ ) sorted by facies  
 736 association (A for clays and marls, B for marl-limestone alternations, C for ooid/bioclast limestones and D for peloid to oncoidal  
 737 limestones). Linear regression lines are plotted on the graphs. Regressive curves are computed only with mini-core porosity  
 738 and permeability (not with NMR). Values of permeability equal to 0.1 mD on mini-core data are linked to physical detection  
 739 limits of measuring devices.  $\Phi$  are expressed in %.

740 Porosity vs. logarithmic permeability relationship is presented in Figure 15 according to facies.

741 The data available for the clay/marl facies association (FA1) are not sufficient to determine a

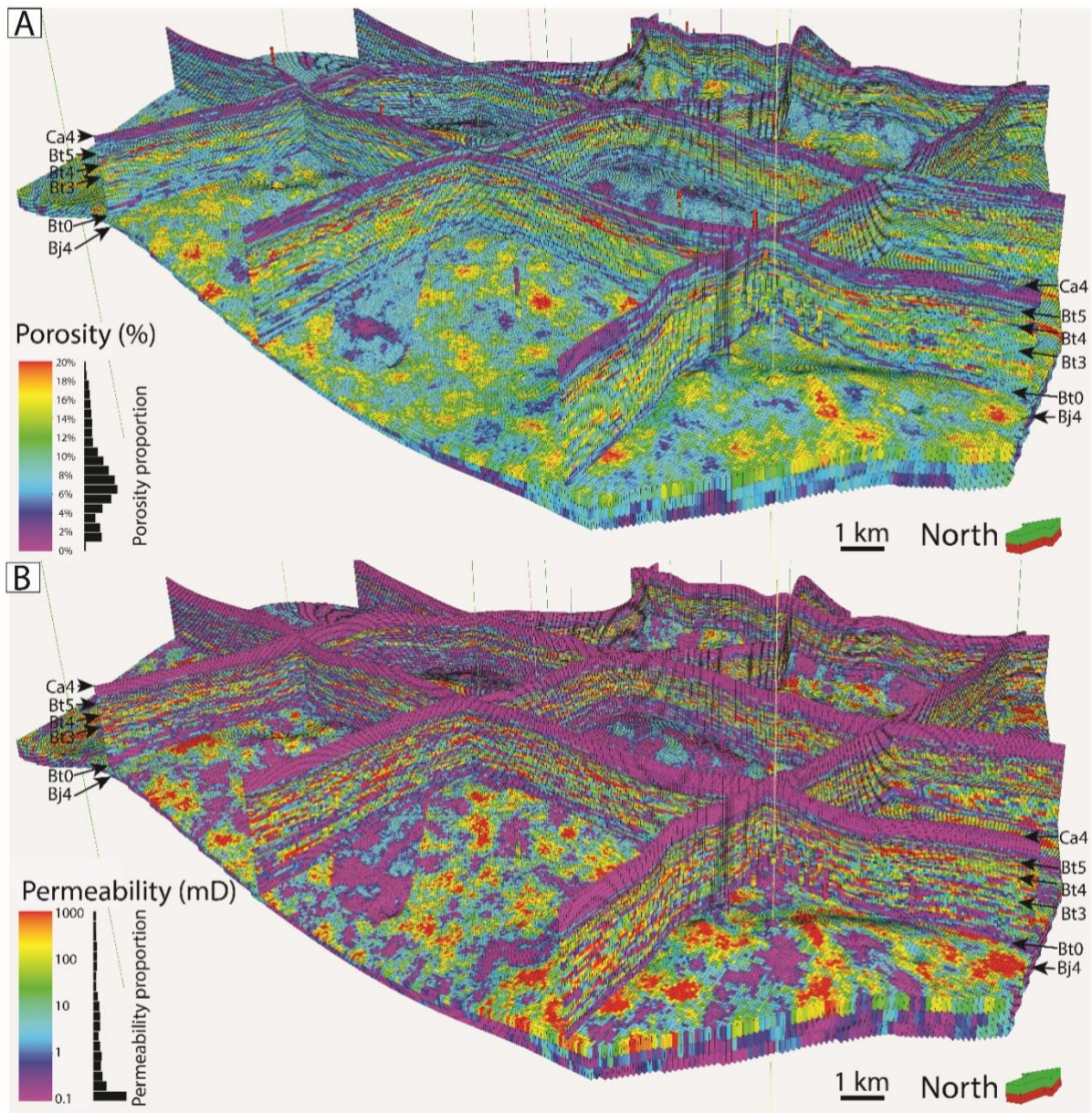
742 possible correlation between porosity and permeability (Fig. 15A). The marl/limestone  
743 alternation facies association (FA2) presents two datasets, (1) mini-core data and (2) porosity  
744 from TCMR versus  $k_{SDR}$  data originating from GCAH-2 (Fig. 15B). Overall, the data in the FA2 is  
745 concentrated between 5 to 15% porosity, but with quite low permeability (0.1 to a few mD).  
746 The ooid/bioclast limestone facies association (FA3) presents a cloud of data clustered in a  
747 zone of higher porosity and permeability (Fig. 15C). This cloud is present between 10 and 20%  
748 of porosity and from 10 to 1000 mD permeability (Fig. 15C). This trend is mainly observed on  
749 the mini-core data. In contrast, TCMR/ $k_{SDR}$  tend to show a more homogenous distribution (Fig.  
750 15C). In the peloid to oncoidal limestones, the sample distribution follows a linear regression  
751 between 8 and 25% of porosity (Fig. 15D). The lower porosity range, from 2 to 8%, follows a  
752 steeper linear regression line (Fig. 15D). Overall, there is a good overlap between mini-core  
753 data and data from the TCMR log (Fig. 15D). They follow a linear regression line (with  
754 permeability expressed as a logarithm) and display a symmetric dispersion for facies  
755 associations 2 (marl/limestone alternations), 3 (ooid/bioclast limestones) and 4 (peloid to  
756 oncoidal limestones) (Fig. 15).

757

#### 758 *4.5 Porosity and permeability distribution in the grid*

759

760



761

762 *Figure 16. A- View of the porosity model from the southeast with vertical cross-sections showing facies variations.*

763 *Stratigraphic surfaces are arrowed. B- View of the permeability model from the southeast with vertical cross-sections showing*

764 *porosity variations.*

765 Of the 12.2 million cells of the entire grid, 6384 cells have upscaled facies, 1686 cells have

766 upscaled porosity and 469 cells have upscaled permeability. Permeability data are only

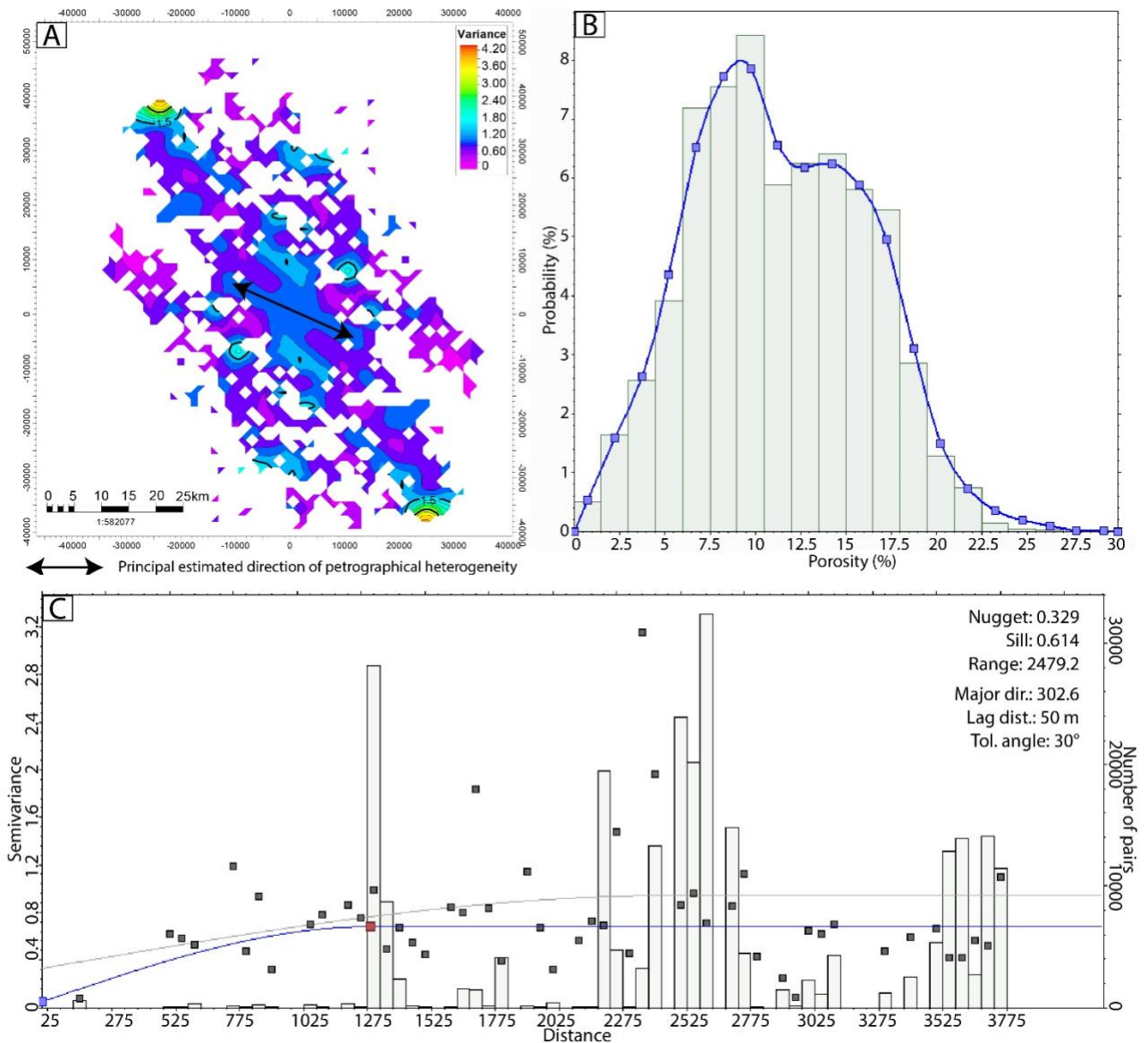
767 available in a small number of wells (34 wells) as it is not a property that could be easily logged

768 in ancient wells. Porosity, on the other hand, was often logged using mini-core plugs or

769 neutron-derived logs. All these cells with upscaled data represent cells where original data

770 issued from the reports or well logs are present as hard data and can be observed in the  
771 corresponding well path. Considering the size of the modeled area, a variance map of the  
772 average porosity of all sequences flattened to the Bt5 surface is produced using 40 lags of  
773 1 km (Fig. 17). Since this model is large, variogram maps cannot be used to determine the  
774 anisotropy accurately, thickness, length, and width of possible carbonate geobodies (porous  
775 layers of oolitic dunes, emerged islands, or less-cemented units; Brigaud et al., 2014). For the  
776 level of precision aimed at, variogram mapping is only used to detect the main direction of  
777 geobodies in a wide area (40 km in X, 40 km in Y). A main direction of N110° is detected (Fig.  
778 16A). This is the main direction of the oolitic barriers around Paris at the end of the Bathonian,  
779 and this direction is, in general, perpendicular to the slope of the ramp (Enay and Mangold,  
780 1980; Mégnien and Mégnien, 1980; Purser, 1980; Rojas et al., 1989). To better determine the  
781 anisotropy values, an individual variogram is calculated for each facies association using  
782 porosity and permeability distributions from well-logs (Fig. 17C, Table 2). The anisotropy of  
783 the different facies associations is determined first across the entire model and is then refined  
784 at the scale of the two targeted, high-quality reservoirs deposited during sequences MJXb and  
785 MJXa (Fig. 17C, Table 2). This step enhances the accuracy of the petrophysical data  
786 propagation across these two important sequences, especially for high reservoir-quality facies  
787 associations (1) ooid limestones and (2) lagoonal facies (Table 2).  
788





789

790 *Figure 17. A- Variogram map of the porosity across the model showing the regional anisotropy of the property. B- Distribution*  
 791 *of the raw porosity data in the ooid/bioclastic facies association. C- Example of the data analysis in Petrel© of a property*  
 792 *(vertical semi-variance of the porosity in the lagoon) across the zone MJXb of the model.*

793 When calculating the anisotropy, the lag distance parameter is very important as it will  
 794 determine the resolution and accuracy steps for the studied property. For the anisotropy  
 795 analysis, as the horizontal lag distance is 50 m, the value is rounded to 50 m, and the  
 796 uncertainty is +/-25 m (Fig. 17C, Table 2). In the vertical direction, the lag distance is set from  
 797 1.5 to 6 m, depending on the facies association and the thickness of the studied zone. The  
 798 well-log data from the mini-cores are taken as a standard to calibrate the “Data Analysis”  
 799 distribution.

Anisotropy values of porosity (m)					
Zone		Clays, marls	Marl/limestone alternations	Ooid/bioclastic limestones	Peloidal to oncoidal limestones
Entire model	Major range (m)	2150	1500	1300	1000
	Minor range (m)	2150	1000	1050	850
	Vertical range (m)	6	3	6	6
Bt5-Bt4 (sequence MJXb)	Major range (m)	N.P.	L.D.	1850	950
	Minor range (m)	N.P.	L.D.	1150	850
	Vertical range (m)	N.P.	L.D.	8	6
Bt4-Bt3 (sequence MJXa)	Major range (m)	N.P.	L.D.	1150	N.P.
	Minor range (m)	N.P.	L.D.	850	N.P.
	Vertical range (m)	N.P.	L.D.	4	N.P.
Anisotropy values of permeability (m)					
Zone		Clays	Marl/limestone alternations	Ooid/bioclastic limestones	Peloidal to oncoidal limestones
Entire model	Major range (m)	2150	1200	1600	850
	Minor range (m)	2150	900	1100	750
	Vertical range (m)	6	3	4	6
Bt5-Bt4 (sequence MJXb)	Major range (m)	N.P.	L.D.	L.D.	850
	Minor range (m)	N.P.	L.D.	L.D.	750
	Vertical range (m)	N.P.	L.D.	L.D.	6
Bt4-Bt3 (sequence MJXa)	Major range (m)	N.P.	L.D.	L.D.	N.P.
	Minor range (m)	N.P.	L.D.	L.D.	N.P.
	Vertical range (m)	N.P.	L.D.	L.D.	N.P.

801 *Table 2: Anisotropy values used in the model, obtained from the Data Analysis. All measurements are in meters. (N.P. = Not*  
802 *Present in the zone, L.D. = Low Data, meaning no clear statistical distribution is identified).*

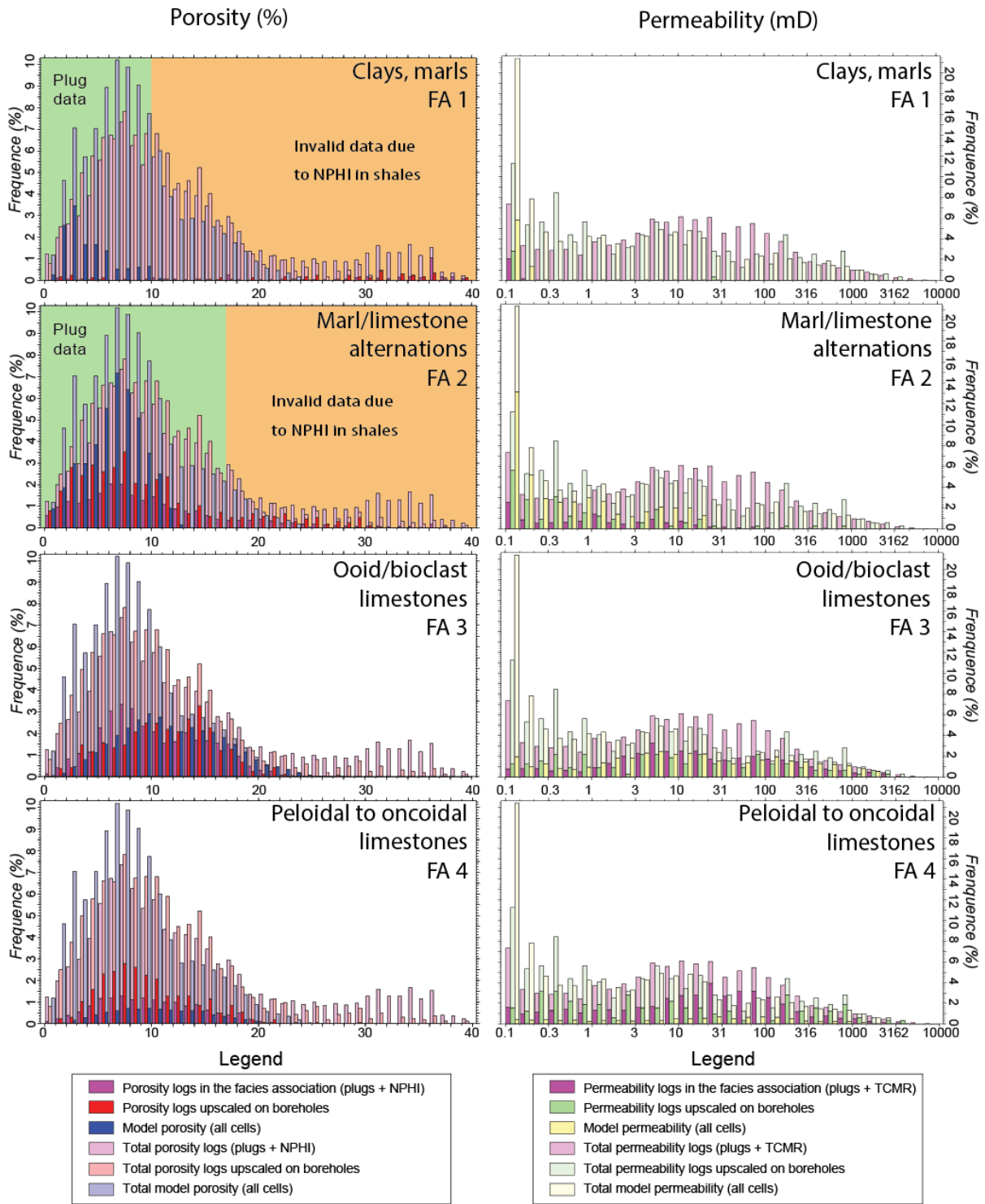
803

804 The Gaussian Random Function Simulation algorithm propagates porosity within the grid  
805 following the anisotropy of porosity for each facies association of the general model or  
806 following the anisotropy of porosity for specific facies associations in the MJXb and MJXa  
807 sequences (Table 2). The variograms used to populate porosity in ooid/bioclast limestones are  
808 mainly elongated perpendicular to the depositional slope, with a general relationship of  
809 1300 m x 1050 m and a thickness of 6 m in all sequences (except for MJXa and MJXb), 1850 m  
810 x 1150 m, and a thickness of 8 m for sequence MJXb, and 1150 m x 850 m and a thickness of  
811 4 m for sequence MJXa (Table 2). The variogram for marl/limestone alternations also shows a  
812 correlation distance mainly elongated perpendicular to the depositional slope, with a general  
813 relationship of 1500 m x 1000 m and a thickness of 3 m in all sequences. Anisotropy is low for  
814 mud-dominated limestones with variograms giving elongated porous layers of 1000 m x 850 m  
815 and a thickness of 4 m for all sequences (Table 2). The porosity variogram for clay facies does  
816 not exhibit anisotropy, with a correlation distance size of 2150 m x 2150 m (Table 2).

817 Permeability is modeled similarly using distributions of permeability in well-logs, spatial  
818 variograms (Table 2), and the Gaussian Random Function Simulation algorithm (Brigaud et al.,  
819 2014b). As the permeability is correlated with the facies and porosity (Fig. 15), a co-kriging of  
820 permeability against porosity is used in the Gaussian Random Function Simulation.  
821 Permeability and porosity are co-kriged using a varying local mean as a correlation and  
822 porosity as a secondary variable (Fig. 15). Each facies association is submitted to its respective  
823 variogram to introduce some heterogeneity into the reservoir (Fig. 16A-B). In clays, the same  
824 variograms are used to populate porosity and permeability. Ooid/bioclast limestones are

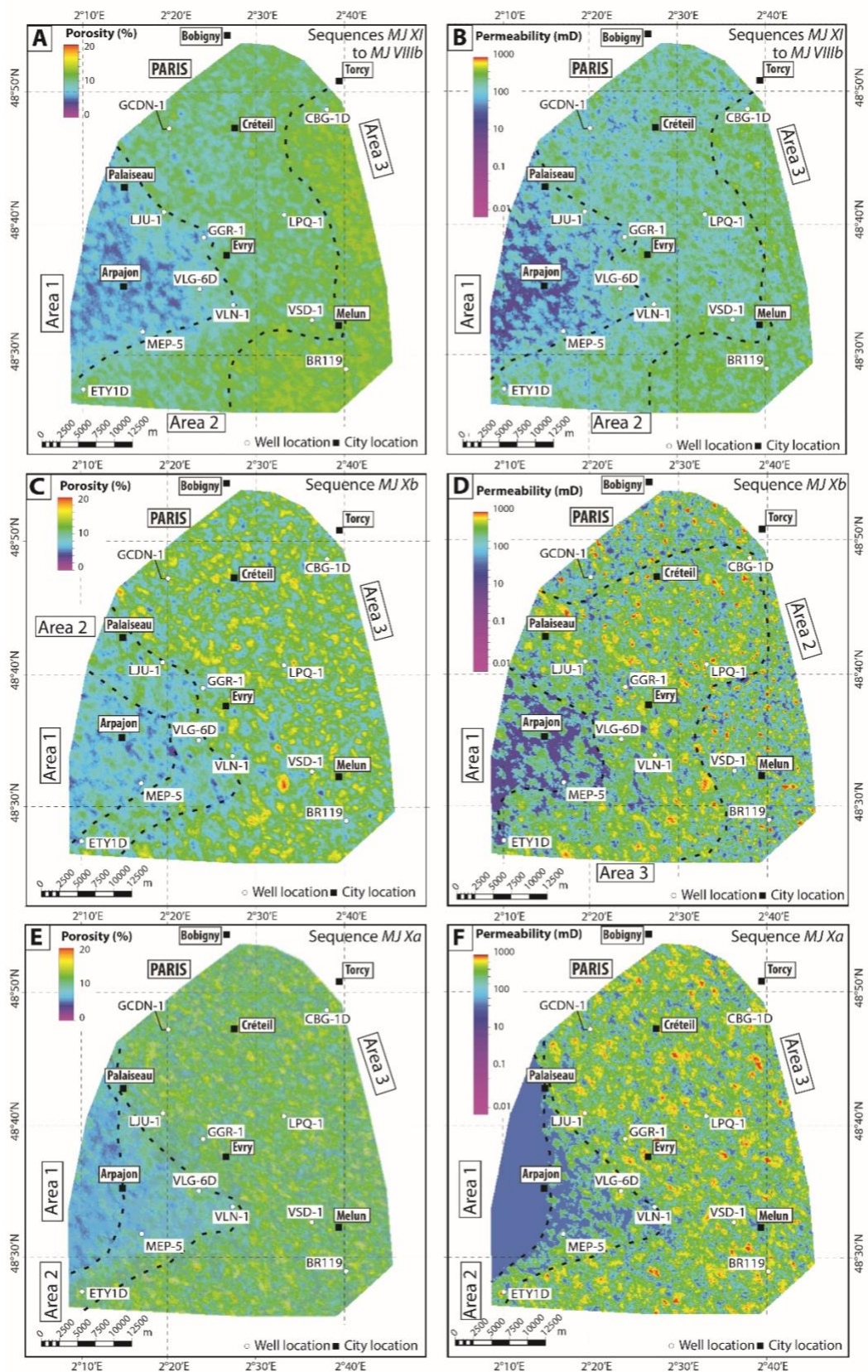
825 mainly elongated perpendicular to the depositional slope, with a general relationship of  
826 1600 m x 1100 m and a thickness of 4 m in all sequences (Table 2). The variogram for  
827 marl/limestone alternations also shows a correlation distance mainly elongated perpendicular  
828 to the depositional slope, with a general relationship of 1200 m x 900 m and a thickness of  
829 3 m in all sequences. Anisotropy is low for mud-dominated limestones with variograms giving  
830 elongated porous layers of 850 m x 750 m and a thickness of 6 m for all sequences (Table 2).  
831 The final porosity and permeability distributions are displayed in figure 16, showing the  
832 heterogeneity in the 3D grid along transects.

833 Histograms are used to compare the distribution of petrophysical properties between well  
834 logs, upscaled cells, and the total model classes after property modeling. These graphs help  
835 to perform quality control on the petrophysical properties (porosity and permeability) for  
836 each coded facies in the model to verify whether the data analysis and data transformation  
837 steps were correctly executed (Table 2; Fig. 18).



838

839 *Figure 18. Porosity and permeability distribution in the different facies associations compared between the final model,*  
 840 *upscaled cells in boreholes and original data in mini-cores given as a percentage of the total number of cells or measured*  
 841 *data. The data distribution is displayed in darker colours for each facies, and the distribution of values in all cells of the model,*  
 842 *independent of facies, is given in a lighter shade. Mini-core data are used as a reference dataset to match the property*  
 843 *distribution in the model. The graphs are separated into 40 columns.*



844

845 Figure 19. A- Average porosity map of sequences MJ VIIIb to MJ XI. B- Average permeability map of sequences MJ VIIIb to MJ XI.

846 C- Average porosity map of sequence MJ Xb. D- Average permeability map of sequence MJ Xb. E- Average porosity map of

847 sequence MJ Xa. F- Average permeability map of sequence MJ Xa. Dashed lines delimit areas discussed in the main text.

848 Porosity and permeability can be extracted on a regional scale (Fig. 19) and averaged to quickly  
849 localize areas with high geothermal potential (Fig. 19). An area around Arpajon, from  
850 Palaiseau, Grigny, Vert-Le-Grand to Marolles-en-Hurepoix exhibits poor reservoir properties  
851 for MJVIIIb to MJXI (area 1 in Fig. 19A-B). On the other hand, the best reservoir quality is  
852 identified in the eastern part of the model, and south of Melun, with high-permeability  
853 patches reaching a few hundreds of mD (Area 3 in Fig. 19A-B). Rojas et al. (1989) presented  
854 permeability maps indicating low global permeability in the western part of the studied zone  
855 with an overall upward trend. Between these two areas, intermediate porosities are present  
856 (area 2 in Fig. 19A). As the most productive reservoir facies are located in MJXa and MJXb  
857 sequences, average porosity and permeability in these two sequences allow us to refine the  
858 characterization of spatial heterogeneity of reservoir quality (Fig. 21C-F). In sequence MJXb,  
859 the area around Arpajon is unsuitable for geothermal exploitation (area 1 in Fig. 19D).  
860 However, some porous and permeable patches are predicted. This corresponds to the  
861 westward progradation of ooids or bioclastic grainstone facies forming a shoal at the end of  
862 the Bathonian. An area from Creteil to the southern part of the model is characterized by the  
863 presence of many very permeable kilometer-scale patches (area 3 in Fig. 19D), from a few  
864 hundred mD (yellow) to 1 D (red, Fig. 19D). This area is the best suited for geothermal  
865 prospects in this sequence (Fig. 21C-D). The rest of the studied zone, north of Creteil and  
866 south-east of Melun (area 2 in Fig. 19D), is characterized by smaller, highly permeable patches  
867 (Fig. 19D). In sequence MJXa, a non-permeable area is clearly identified east of Palaiseau and  
868 Arpajon (area 1 in Fig. 19F). A triangular area, between Palaiseau/Arpajon and Evry (area 2 in  
869 Fig. 19F), presents highly heterogenous reservoir quality, with local permeable patches up to  
870 a few hundred mD (green to yellow, Fig. 19B), separated by more extensive areas of  
871 impermeable patches (blue, Fig. 19). It should be noted that the shape of the permeable lenses

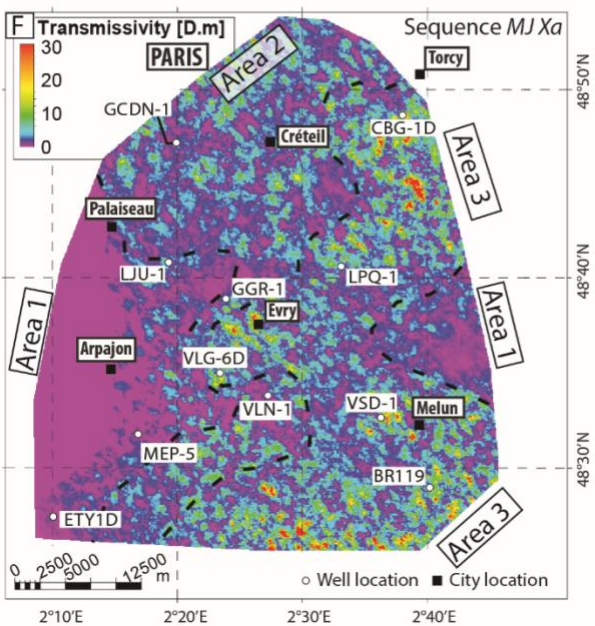
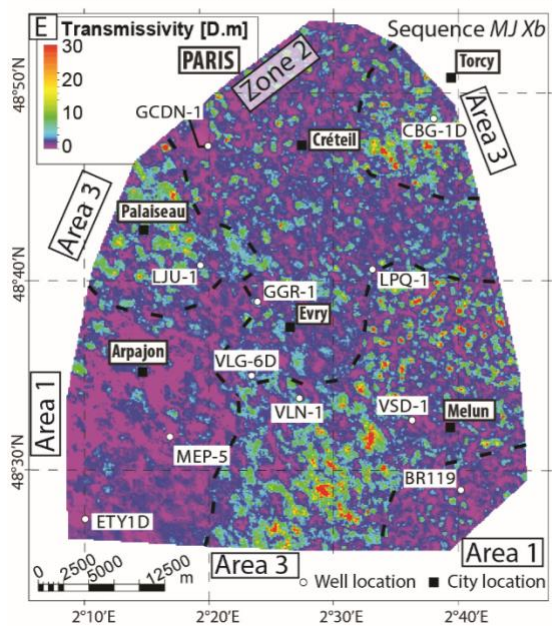
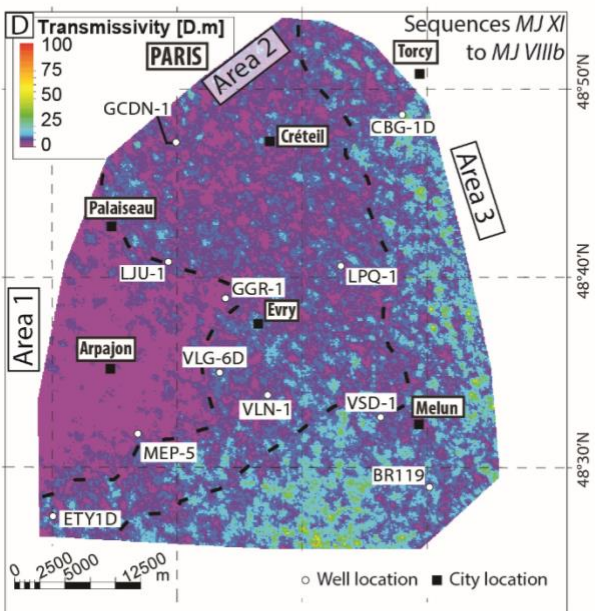
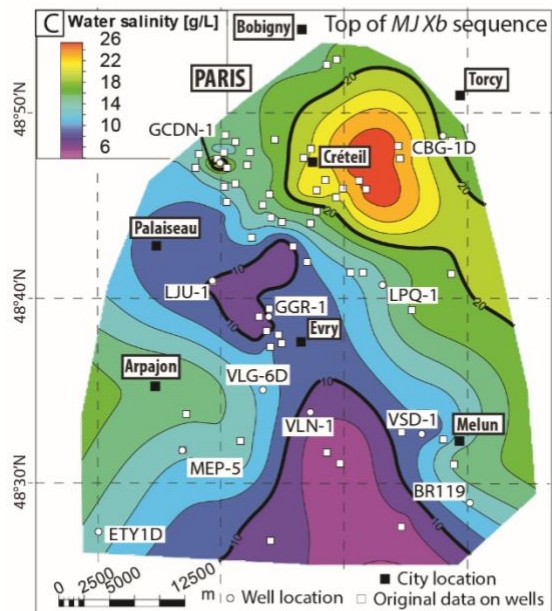
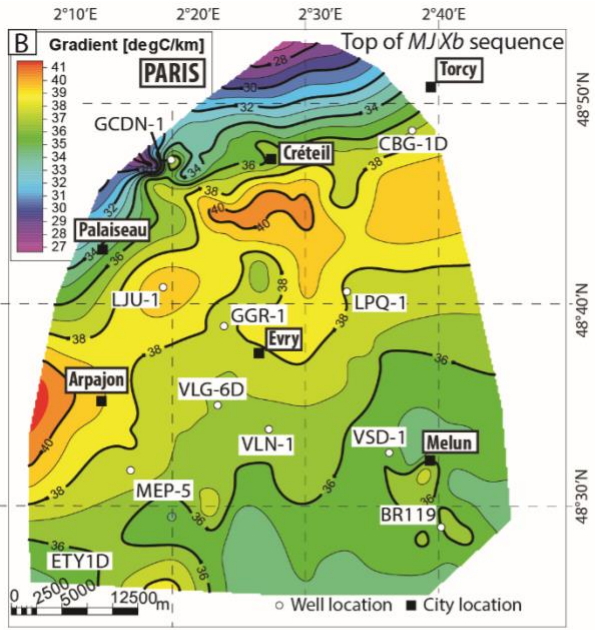
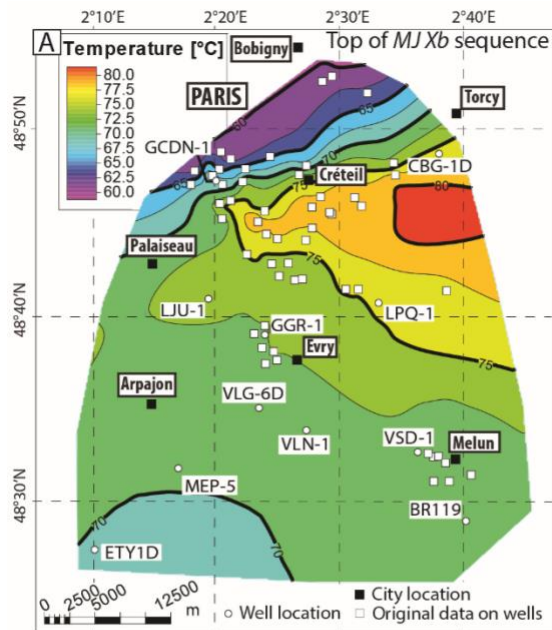
872 is robust, but their location is uncertain. They are not necessarily well located, perhaps 1 or 2  
873 km away. In the rest of the modeled zone, the averaged petrophysical properties are very  
874 good and display numerous high-permeability patches (around one kilometer in size)  
875 separated by non-permeable kilometeric patches (area 3 in Fig. 19F).

876

877 *4.6 Temperature, salinity, transmissivity, and thermal gradient*

878





880 *Figure 20. A- Temperature map at the top of the late Bathonian (Bt5) created from well data. B- Temperature gradient map*  
881 *at the top of the late Bathonian (Bt5) created from well data. C- Salinity map at the top of the late Bathonian (Bt5) created*  
882 *from well data D- Transmissivity map of reservoir between Sequences MJXI to MJVIIIb. E- Transmissivity map of Sequence*  
883 *MJXb. F- Transmissivity map of Sequence MJXa.*

884

885 A map has been constructed from the temperatures available in the well reports at the top of  
886 the reservoir using a convergent interpolation algorithm, helping to understand the  
887 temperature distribution (Fig. 20A). The south-eastern part of the study area does not have  
888 useful data, as temperature data in the area are issued from the drilling reports and are not  
889 usable as they are. Temperatures show high variability ranging from 58 °C in the northern part  
890 of the area to 82 °C in the western part (Fig. 20A). Also, in the southwest of the studied area,  
891 no trustworthy temperature could be extracted from the old well data available in this specific  
892 area. A transition from low temperatures of about 60 °C around Paris to high temperatures of  
893 80 °C in the eastern part of the model is clearly visible (Fig. 20A). A geothermal gradient map  
894 using temperature and depth maps of the top of the reservoir has been extracted (Fig. 20B).  
895 The gradient resulting from this study at the top of sequence MJXb indicates some interesting  
896 variations concerning the raw temperature map (Fig. 20B). A corridor showing high gradients  
897 runs from Arpajon to the south of Torcy, with values around 40 °C/km, which is in the high  
898 range of geothermal gradients in the Paris Basin, and more generally in intracratonic basins  
899 (Fabris, 1975; Rojas et al., 1989). The southern part of the basin presents homogeneous values  
900 of around 36 °C/km (Fig. 20B). In the northern part of the model, however, the gradient drops  
901 drastically to 27 °C/km around Paris. Compared to temperature, a different pattern appears  
902 for salinity (Fig. 20C). A corridor of low salinity (less than 10 g/L) is present from Palaiseau  
903 through Evry to the south of the model, as already described by Rojas et al. (1989) and Matray  
904 and Fontes (1990). Higher values, reaching 26 g/L, are observed west of Creteil (Fig. 20C).

905 With this study database, we also calculated transmissivity distribution maps (Fig. 20D-F). We  
906 combined the permeability maps averaged for groups of sequences or individual sequences  
907 with the thickness maps to estimate the possible reservoir transmissivity (Fig. 20D-F). The  
908 transmissivity property is bound to the calculated permeability in the model, averaged  
909 between the cells of a sequence multiplied by the thickness of the sequence. In Bathonian  
910 limestones (sequences MJVIIIb to MJXI), the lowest transmissivity is located around Arpajon  
911 (area 1 in Fig. 20D) whereas the most transmissive regions are located in the eastern and  
912 southern parts of the modeled zone with transmissive patches of 50 D.m (area 3 in Fig. 20D).  
913 This is because sequences MJVIIIc and MJIX are mainly composed of ooid/bioclast limestone  
914 facies in the eastern part of the model (Figs 10A and 12C). In the west, sequences MJVIIIc and  
915 MJIX consist mainly of low transmissivity marl/limestone alternations (Figs 10A and 12C).  
916 Intermediate transmissivity patches (about 10 D.m) are present around Créteil and north of  
917 Evry (area 2 in Fig. 20D), due to the smaller vertical thickness of ooid/bioclast limestones of  
918 sequences MJVIIIc and MJIX (Fig. 12C). In detail, the MJXb sequence presents very good  
919 transmissivity around Palaiseau, between Creteil and Torcy, and west of Melun (area 3 in Fig.  
920 19E). Area 2 also presents some interesting zones, forming scattered patches around 10 D.m  
921 (green in Fig. 20E). Transmissivity is low in the south-west and south-east of the model, due  
922 to the occurrence of mud-dominated facies without a granular facies unit (Area 1 in Fig. 20E).  
923 The MJXa sequence presents very low transmissivity in the western and eastern parts of the  
924 model (area 1 in Fig. 20F). An intermediate area (area 2 in Fig. 20F) presents local patches of  
925 tens of D.m and a high potential area (area 3 in Fig. 20F) presents short-wavelength patches  
926 of 30 D.m.

## 927 **5. Discussion**

928 *5.1 Temperature, salinity, transmissivity, and thermal gradient heterogeneity at the regional*  
929 *scale*

930 The high heterogeneity of petrophysical properties is known (Housse et al., 1976; Rojas et al.,  
931 1989; Le Nir et al., 2008; Lopez et al., 2010) and is confirmed by the supplementary data added  
932 to our model. Namely, temperature, thermal gradient, salinity, and transmissivity have been  
933 mapped in the study zone (Fig. 20D-F). The eastward deepening of the top of the reservoir  
934 from a vertical depth of 1460 m in Paris (temperature 58 °C) to 1660 m (temperature 82 °C)  
935 around Torcy is not sufficient to explain the 20 °C increase in temperature. It could only  
936 explain a drop of 4 °C to 8°C. Furthermore, the top of the reservoir is located at less than 1400  
937 m depth near Arpajon (temperature 68 °C), 10°C hotter than under Paris (58°C at 1460 m),  
938 showing that geothermal gradient is heterogeneous. Therefore, another mechanism must  
939 explain the drop in observed temperatures in the northwest of the studied area. This local  
940 geothermal gradient variation from 27 °C/km to 40 °C/km (Fig. 20B) is not well understood.  
941 To explain the heterogeneous geothermal gradient in the reservoir, Rojas et al. (1989)  
942 suggested (1) possible heat flux variation or, from pressure gradient, (2) fluid flow in the  
943 reservoir such as cold horizontal water flows from west of the greater Paris area to the north  
944 of Paris. This horizontal fluid flow would, however, be opposite to the rest of the formation  
945 water flows (Rojas et al., 1989). The regional flow, reconstructed by Menjoz et al. (1993),  
946 shows water flow from the southeast to the northwest, going from the Middle Jurassic  
947 limestone outcrops in Burgundy and Lorraine areas (Eastern Paris Basin) toward the English  
948 Channel. Regional flow modeling at the scale of the Paris Basin shows a possible effect of flow  
949 velocity increase to explain a positive anomaly of + 10 °C south of Paris (Menjoz et al., 1993).  
950 However, on re-interpreted seismic profiles, Dentzer et al. (2018) identified reduced seismic  
951 amplitude along chimneys corresponding to pervasive fractures. Cold water drawdown flows,

952 from the Late Jurassic and Early Cretaceous aquifers, along these chimneys, could partly  
953 explain the 20 °C fall in temperature between the northern and eastern parts of the model  
954 (Dentzer et al., 2018).

955 The transmissivities are in the same range as published earlier (Rojas et al., 1989), from less  
956 than 5 D.m west of Palaiseau to 50–75 D.m around Créteil. However, the transmissivity maps  
957 extracted from our model provide higher resolution than what was known in the literature  
958 (Rojas et al., 1989), showing locations of small transmissive patches unknown hitherto (Fig.  
959 20D-F). Transmissivity at the doublet scale is highly uncertain where no well data is available.  
960 Nonetheless, this study helps to better determine interesting areas of high transmissivity  
961 (locally above 50 D.m in area 3, Fig 20D), providing trends and a better understanding of the  
962 variations at the regional scale. The focus on the sequences MJXa and MJXb highlights the best  
963 areas of geothermal energy in the southern part of the greater Paris area (Fig 20E-F).

964

## 965 *5.2. Discussion – facies and impact on reservoir quality*

### 966 5.2.1. 3D heterogeneity at the core scale

967 In the high reservoir-quality facies association (facies association FA3; ooid/bioclust  
968 limestones), the pore network is relatively heterogeneous. Whereas pore sizes of facies F3b  
969 are relatively homogenous, with very well connected pores between 100 and 500 µm (Fig. 7B),  
970 facies F3c, which presents a grain type similar to the excellent reservoir facies F3b, displays  
971 intergranular spaces filled by large blocky calcite, reducing the porosity to intraparticle  
972 micropores (Fig. 7C). The lack of micrite and the presence of well-formed ooids (diameter of  
973 400 to 500 µm; Fig. 7B) indicate a high-energy environment, corresponding either to oolitic  
974 shoal or giant dunes (Thomas et al., 2021; Vincent et al., 2021). Diagenesis plays an essential  
975 role in the reservoir quality of this facies association. Isopachous cements protected the rock

976 against any decrease in its intergranular pore space during compaction (Purser, 1978; Brigaud  
977 et al., 2010, 2014a). Dedolomitization enhanced the effective porosity of facies F3b, and  
978 probably F3d (Fig. 7B-D), as already observed in the Coulommès oilfield 20 km from the study  
979 area (Purser, 1985), or in the Massangis outcrop analogue in Burgundy (Thomas et al., 2021).  
980 Facies F3d exhibits larger pores than facies F3b, from 100  $\mu\text{m}$  to 2 cm. However, the pores are  
981 less interconnected (Fig. 7D, Fig. 8). Large calcite crystals grew between bioclastic grains,  
982 especially along echinoderm fragments, filling pore space. Facies F3c is another good example  
983 of the diagenesis effects on reservoir properties. The heterogeneity of carbonate cementation  
984 is challenging to predict. The modeling of individual facies is complex due to the scarcity of  
985 core samples in the study area. The mud-dominated limestone facies association also has  
986 heterogeneous reservoir quality. Facies F4a and F4c were deposited in a calm environment  
987 where carbonate mud could settle, forming muddy facies with poor reservoir qualities. Facies  
988 F4b and F4d present grainstone to rudstone textures, indicating the presence of local  
989 moderate-energy zones in the otherwise calm lagoon (Rankey, 2014; Harris et al., 2015).  
990 Facies F4b is the only facies in this association displaying high porosity and permeability. As in  
991 facies F3b, pores are well connected and from 50  $\mu\text{m}$  to 500  $\mu\text{m}$  in size. Facies F4b forms  
992 permeable patches in a mud-dominated environment. Unfortunately, it has not been possible  
993 to model these individual facies due to the scarcity of core descriptions. Facies F4d, while  
994 similar in grain type and texture to facies F3d, underwent more intense carbonate cement  
995 development. The porosity only exists as intraparticle porosity, as well described around Saint-  
996 Martin-de-Bossenay (Delmas et al., 2010) (Fig. 7H).

997 Permeabilities can also exhibit a high degree of spatial heterogeneity at all scales, largely  
998 depending on the depositional environment and the subsequent diagenetic processes. High  
999 porosity and permeability values are controlled by (1) a high-energy environment, (2) low

1000 carbonate cement development, and (3) dissolution. A porous media micro-CT scan reveals  
1001 marked pore space heterogeneity, as demonstrated for facies F3d (Fig 8). Facies F3d has a  
1002 grainstone to rudstone texture and is composed of common intraclasts, gastropods, bivalves,  
1003 brachiopods, and echinoderm fragments. Large pore spaces up to the millimetric scale and  
1004 thin layers with millimetric bivalve and brachiopod shells probably induced strong horizontal  
1005 permeability anisotropy (from 70 mD to 145 mD) and relatively high vertical permeability  
1006 (135 mD). Heterogeneous millimeter-size blocky calcite crystals cementing the intergranular  
1007 space and local dissolution led to complex pore media at the centimetric scale.

1008

#### 1009 5.2.2. 3D heterogeneity at the doublet or multi-doublet scale

1010 For the Middle Jurassic limestones of the greater Paris area, no published geological model  
1011 capturing its fine-heterogeneity (facies, porosity and permeability) at the reservoir scale is  
1012 currently available, which was highlighted a decade ago by Lopez et al. (2010). Companies as  
1013 GEOFLUID or the French Geological Survey (BRGM) maintain an up-to-date hydraulic and  
1014 thermal model of the aquifer to predict the lifetimes of doublets and the occurrence of the  
1015 thermal breakthrough, but no heterogeneous geological model capturing the fine  
1016 heterogeneity of facies, porosity and permeability in the reservoir (XY dimension of the order  
1017 of hundreds of m and Z dimension of the order of a meter), (Ungemach et al., 2005; Lopez et  
1018 al., 2010; Hamm et al., 2010, 2015; Papachristou et al., 2016). The BRGM has built a well-  
1019 documented database on the “Geological Data Modeling” (GDM) tool (Hamm et al., 2015). An  
1020 analysis of the flowmetry well-logs and sedimentological facies distributions along wells was  
1021 carried out with two important information: (1) the depths of the producing levels with their  
1022 contribution to the total flow and (2) the depths of the sedimentological facies (lagoonal,  
1023 otolithic and marly facies, Hamm et al. 2015). Simple correlations, without variogram analysis,

1024 of the producing levels between wells separated by less than 1 km were able to be carried out  
1025 for the Chelles and Coulommiers doublets, indicating continuities between some producing  
1026 levels but not for others (Hamm et al., 2015). Geostatistical distributions of available reservoir  
1027 transmissivities published in the area were made more than 30 years ago and are shown as a  
1028 map at the scale of 100 km x 100 km (Rojas et al., 1989). The dataset of Hamm et al. (2015) is  
1029 not publicly available, including geolocalization of wells, facies along wells, producing level  
1030 and flow rate, for a reopening on GDM or other geomodeler such as Petrel©. Here, we  
1031 propose a strong update of the geological data of the geothermal reservoir, providing an open-  
1032 access 3D digital model (XYZ dimension of the entire model of about 40 km x 50 km x 0.2 km).  
1033 We also propose very fine heterogeneity in a total of 12.2 million cells capturing heterogeneity  
1034 of facies, porosity and permeability (XYZ cell dimension of 100 m x 100 m x 3.73 m on average).  
1035 As 3D heterogenous geological model and recent geological study at the scale of the reservoir  
1036 were unavailable, geological risks for total or partial failure existed as mentioned above for  
1037 the Grigny well (Lopez et al., 2010). Operations along the outer part of the oolitic ramp (facies  
1038 FA3) are very risky (around Evry, Figs. 20 and 21). At the multi-doublet scale, our model allows  
1039 us to view 3D heterogeneity in the grid. Eight doublets in the area around Evry provide a high-  
1040 resolution picture of facies, porosity, and permeability distribution. At this scale, the model  
1041 presented in this study clearly shows that porous areas form patches of about 1500 m x  
1042 1000 m and thickness of 6 m on average in ooid/bioclast limestones, separated by low-  
1043 porosity (<10%) units (Fig. 21A-C). Stratigraphically, these porous patches are mainly located  
1044 just below maximum regressive surfaces Bt5 and Bt4, in sequences MJXa and MJXb (Fig. 21C).  
1045 Local porous patches, smaller in size (1000 m x 850 m x 6 m), are located in mud-dominated  
1046 limestones, in granular facies (Fig. 21A-C). As permeability is correlated to porosity, permeable  
1047 bodies also form slightly larger patches (1600 m x 1100 m x 4 m) disconnected from each other



1048 (Fig. 21D). It is important to note that this distribution is strongly controlled by facies  
1049 association distribution in the model. Around Evry, the ooid/bioclast limestones form a wedge  
1050 prograding westward (Fig. 21B). Total thickness of the ooid/bioclast limestones decreases  
1051 from east to west, from 50 m to 28 m respectively at the reservoir scale (Fig. 21B). For  
1052 example, the Grigny 2 well (GGR2) has 3 m of oolitic limestone and 6.5 m of mud-dominated  
1053 limestone facies (which could also have some local high reservoir quality) in sequence MJXb.  
1054 In sequence MJXa, 19 m of oolitic limestones with marl/limestone alternations are found (Fig.  
1055 21B). A few kilometers further southeast, a good reservoir example can be observed in the  
1056 Evry 1 well (GEV1) with 32 m thickness for sequence MJXb and MJXa (Fig. 21B). In the Grigny  
1057 2 well (GGR2), the high-quality ooid/bioclast limestones change laterally into marl/limestone  
1058 alternations, which have low reservoir quality. As no model was available before the  
1059 installation of the Grigny doublet, a geological risk has been taken to drill GGR2 in this area.  
1060 The GGR2 well turned out to be a failure in terms of transmissivity with very thin beds of  
1061 porous limestones (meter-scale). The 3D zoom extracted from our model clearly shows the  
1062 thickening of the marl/limestone alternations and thinning of the oolitic limestone reservoir  
1063 from GGR-1 to GGR-2. The representation given here is very precise, predicting depths of the  
1064 top of the reservoir and possible permeable levels, typically located 20 m below the caprock  
1065 in this area. This indicates that models as the one presented here in this study could de-risk  
1066 future operations and provide a tool to assist investors in deciding on the drilling of future  
1067 geothermal wells by providing risk criteria for future projects (Fig. 21).

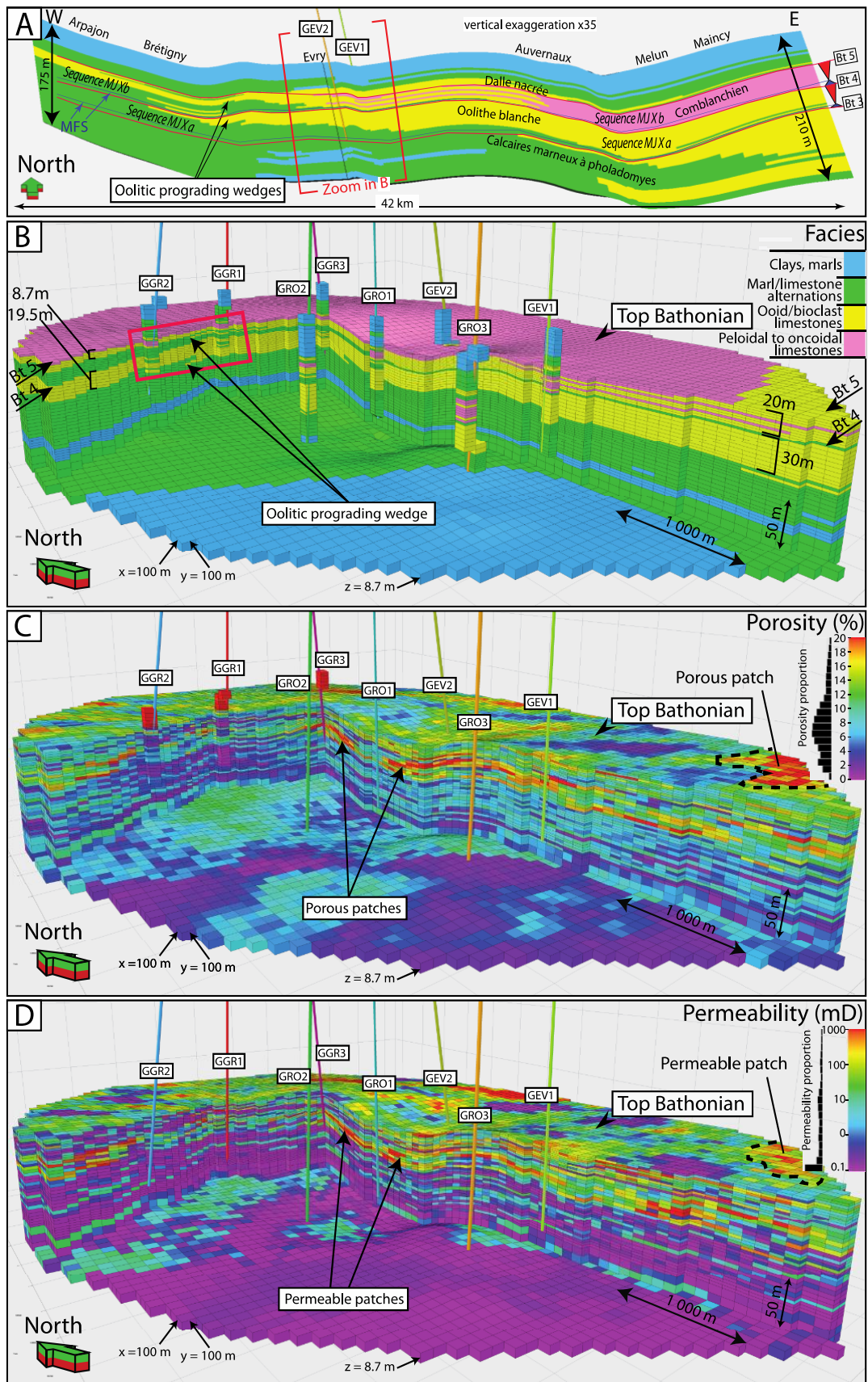
1068 3D seismic is proving to be a very promising tool to strengthen the predictions of geothermal  
1069 resources (Casini et al., 2010; Lüschen et al., 2011; Drouiller et al., 2019; Salaun et al., 2020).

1070 Use of 3D seismic data is increasing in the exploration and production of geothermal resources  
1071 in European basins (Munich, Vienna, ...). This kind of data is, however, not available in this

1072 study area, but it would be an excellent addition to de-risk the implementation of new  
1073 doublets as it could help to localize areas of high potential in zones where well data is not  
1074 present nearby and its general use should be seriously discussed also for the Paris area  
1075 (Drouiller et al., 2019). Deep neural networks are also promising to estimate porosity and  
1076 permeability in the Middle Jurassic geothermal reservoir from old 2D seismic lines acquired in  
1077 the 1980s and well log data (Allo et al., 2021).

1078 The facies property model is very deterministic. This is due to the “Truncated Gaussian with  
1079 Trends” algorithm, enabling the possibility to strongly influence the facies repartition both  
1080 horizontally and vertically inside a zone (zone as a thickness layer in the model, here,  
1081 depositional sequence) to constrain the property to mimic the “trends” observed in the facies  
1082 data. However, the porosity and permeability properties are distributed randomly in the  
1083 volume, such as to respect the variograms, histograms, and hard data issued from the  
1084 upscaling process. A good way to reduce the uncertainty of porosity and permeability  
1085 prediction as the distance of a cell increases from the closest cell containing hard data would  
1086 be to use 3D seismic data, precise gravimetry and recalculated/synthetic well logs or reservoir  
1087 analogue to populate the grid with usable trends (Petrovic et al., 2018; Arnold et al., 2019;  
1088 Feng et al., 2020). This could enhance the predictability of properties in the volume.

1089 Creating synthetic logs from other well logs could be a way to de-risk future operations,  
1090 allowing for more upscaled cells in the model. For example, it is possible to create a  
1091 permeability log by applying porosity-permeability relationships from the Neutron logs (Lucia,  
1092 2007). However, in this study, as porosity-permeability data is relatively heterogeneous along  
1093 facies association (Fig. 15), only real data were used from well logs as synthetic logs could be  
1094 a new vector of uncertainty. For new geothermal operations, the NMR logging tool is very  
1095 promising, giving a continuous record of permeability (Wielemaker et al., 2020).



1096

1097  
1098  
1099  
1100

Figure 21. Close look at the zone of the Grigny Bathonian reservoir highlighted in Fig 3. A- West-east stratigraphic cross-section through the modeled area, crossing near cities of Arpajon, Brétigny, Evry, Auvernaux and Maincy. The two main reservoir sequences MJXa and MJXb prograde westward. B- Facies distribution. C- Porosity distribution. D- Permeability distribution. The red rectangle highlights the reservoir thinning discussed in the main text.

1101 **6. Conclusions**

1102 To guide the positioning of future geothermal doublets, this paper presents the first high-  
1103 resolution 3D reservoir model of the Middle Jurassic geothermal reservoir in the south-  
1104 eastern greater Paris area (about 40 km x 50 km x 0.2 km). This 3D model, compiling all the  
1105 available well-log data for the area, details the geological architecture and specifies the 3D  
1106 reservoir heterogeneity of the late Bajocian to early Callovian limestones. The resulting 3D  
1107 model is one possible 3D realization showing the geological heterogeneities. The grid of the  
1108 model including zones, facies, porosity and permeability propagated in the volume, as well as  
1109 temperature and salinity with their representative maps, are available online as a .rar file. This  
1110 realization should be used to inspire further modeling and doublet planning. Important  
1111 information such as the top of the reservoir, facies heterogeneity or possible location of  
1112 permeable layers will be available. The geostatistical results presented here could be taken  
1113 into account in future geothermal developments in order to propose other possible  
1114 realizations and to investigate, for example, the uncertainties. This 3D representation will be  
1115 a prerequisite for thermo-hydro-dynamic simulations and could provide support to assist  
1116 decision-making on potentially low-risk areas for future geothermal development in a  
1117 carbonate reservoir. The primary outcomes of this study are:

1118

- 1119 1. The creation of a digital database compiled for 168 wells. This database includes 4561  
1120 porosity and 3317 permeability values from routine analysis of mini-cores from 40  
1121 wells, precisely located in 3D. It is the most complete published database of the Middle  
1122 Jurassic geothermal reservoir in this part of the basin.

1123

1124 2. The late Bajocian to early Callovian deposits contain 13 facies grouped into four facies  
1125 associations: (1) clays and marls from lower offshore, (2) marl/limestone alternations  
1126 from upper offshore, (3) ooid/bioclast limestones from shoreface, and (4) mud-  
1127 dominated lagoonal limestones. Many oolitic facies have good reservoir quality (25%  
1128 of the porosities are higher than 17% and permeabilities higher than 340 mD). The  
1129 granular facies located in the mud-dominated facies association locally has good  
1130 reservoir units (25% of the porosities above 12.7% and permeabilities above 252 mD).

1131  
1132 3. A high-resolution sequence stratigraphy scheme was constructed on the ammonite  
1133 biozone scale, with the identification of 12 third-order depositional sequences (MJXIVb  
1134 to MJVIIIa), that can easily be integrated into existing stratigraphic schemes on the  
1135 basin scale and more generally on the scale of the western European basins. Sequences  
1136 MJXa and MJXb (*hodsoni* and *orbis* Zone) form the two targeting sequences for  
1137 geothermal development.

1138  
1139 4. Facies association distribution defined in the 168 wells are upscaled to populate the  
1140 grid using the Truncated Gaussian with Trends (TGwT) algorithm, applied sequence by  
1141 sequence. The facies model presents facies heterogeneity in 53 layers to maintain a  
1142 very good vertical resolution (average of 3.73 m). This 3D facies model locates the  
1143 ooid/bioclast limestone wedge, prograding from east to west.

1144  
1145 5. Porosity and permeability along wells are upscaled to the model layering by  
1146 calculating the arithmetic average for the porosity and the geometric average for the  
1147 permeability. Of the 12.2 million cells of the entire grid, 6384 cells (XYZ cell dimension

1148 of 100 m x 100 m x 3.73 m on average) have upscaled facies, 1686 cells have upscaled  
1149 porosity and 469 cells have upscaled permeability.

1150

1151 6. The temperature of geothermal water ranges from 51 °C to 79.3 °C. A temperature  
1152 gradient map shows heterogenous geothermal gradients, from high values (37 to  
1153 41 °C/km) in an area between Etrechy in the southwest and Croissy-Beaubourg in the  
1154 northeast, to low gradients of about 27 °C/km, around Paris itself. The area presenting  
1155 the highest temperature gradients also presents average good petrophysical reservoir  
1156 qualities and transmissivities.

1157

1158 7. Geostatistics show the occurrence of permeable patches of 1600 m x 1100 m (XY  
1159 dimensions) and a thickness of 4 m (Z dimension) elongated perpendicular to the  
1160 depositional slope in the ooid/bioclast limestone. In the peloidal-oncoidal limestone,  
1161 permeable patches consist of porous granular facies with a size of 850 m x 750 m x  
1162 vertical thickness of 6 m (XYZ dimensions).

1163

1164

#### 1165 **Acknowledgements**

1166 This work is supported by the UPGEO “UPscaling and heat simulations for improving the  
1167 efficiency of deep GEOthermal energy” program funded by the Agence Nationale de la  
1168 Recherche [ANR-19-CE05-0032-01]. We would like to dedicate this work to Andro Mikelic, who  
1169 left us in 2020, and who was a driving force behind the construction of the UPGEO project and  
1170 who more generally developed many research activities in mathematics on upscaling and fluid  
1171 flow in porous media. This work is also supported by the “Geothermal water circulation in

1172 heterogeneous aquifers” project funded by the “Paris-Saclay Initiative d’Excellence”, a state  
1173 aid program managed by the Agence Nationale de la Recherche [ANR-11-IDEX-0003].  
1174 University Paris-Saclay benefits from the Schlumberger Software Donation Program. We are  
1175 grateful to Schlumberger for the academic license for Petrel© software and for very valuable  
1176 support in its utilization. We also thank Anaëlle Guillevic, Maë-Berinda Babadoudou, Maoli  
1177 Compay (bachelor students), Vivien Folliot, Anne-Sophie Canivet, Myriam Mansour, Codjo  
1178 Thomas Florent Essou (master students) for the digitalization of wells using Neuralog.  
1179 We also thank the four anonymous reviewers who helped with their comments to increase  
1180 the clarity of the manuscript.

#### 1181 **Data availability**

1182 Datasets of the 3D model are available as a .rar file which can be found at  
1183 <https://data.mendeley.com/datasets/kd6dyfwg5f/1> (doi:10.17632/kd6dyfwg5f.1), an open-  
1184 source online data repository hosted at Mendeley Data. This file can be read only with  
1185 Schlumberger software Petrel©, version 2019.2 and later. It contains an extracted grid of the  
1186 model including zones, facies, porosity and permeability propagated in the volume, as well  
1187 as temperature and salinity with their representative maps. Supplementary Table A  
1188 summarizes the wells manager available in Petrel©. It contains the well names, positions,  
1189 maximum depth, type of well, origin of the data and a summary of the available well logs.  
1190 Supplementary Table B, an Excel sheet, resumes all the petrophysical data available from  
1191 mini-cores and integrated in the model, as well as the temperatures and salinities.

#### 1192 **Appendices**

1193 Supplementary Table A: Well manager spreadsheet summarizing well names, positions,  
1194 maximum depth, type of well, origin of the data and available well logs.

1195 Supplementary Table B: Porosity, permeability, temperature and salinity spreadsheet. All the  
1196 data are reported by well name, depth and facies type.

## 1197 **References**

1198

- 1199 Allo, F., Coulon, J.-P., Formento, J.-L., Reboul, R., Capar, L., Darnet, M., Issautier, B., Marc,  
1200 S., Stopin, A., 2021. Characterization of a carbonate geothermal reservoir using rock-  
1201 physics-guided deep neural networks. *Lead. Edge* 40, 751–758.  
1202 <https://doi.org/10.1190/tle40100751.1>
- 1203 Andrieu, S., Brigaud, B., Barbarand, J., Lasseur, E., Saucède, T., 2016. Disentangling the  
1204 control of tectonics, eustasy, trophic conditions and climate on shallow-marine  
1205 carbonate production during the Aalenian–Oxfordian interval: From the western  
1206 France platform to the western Tethyan domain. *Sediment. Geol.* 345, 54–84.  
1207 <https://doi.org/10.1016/j.sedgeo.2016.09.005>
- 1208 Arnold, D., Demyanov, V., Rojas, T., Christie, M., 2019. Uncertainty Quantification in  
1209 Reservoir Prediction: Part 1—Model Realism in History Matching Using Geological  
1210 Prior Definitions. *Math. Geosci.* 51, 209–240. [https://doi.org/10.1007/s11004-018-](https://doi.org/10.1007/s11004-018-9774-6)  
1211 [9774-6](https://doi.org/10.1007/s11004-018-9774-6)
- 1212 Aubertin, G., Benderitter, Y., Cordier, Eli., Doillon, F., Fabris, H., Gable, R., Gaillard, B.,  
1213 Ledoux, E., de Marsily, G., 1987. Détermination expérimentale de la vitesse naturelle  
1214 d'écoulement de la nappe géothermique du Dogger en région parisienne. *Bull. Société*  
1215 *Géologique Fr.* 3, 991–1000. <https://doi.org/10.2113/gssgfbull.III.5.991>
- 1216 Autran, A., Lefort, J.P., Debeglia, N., Edel, J.B., Vignerresse, J.L., 1994. Gravity and  
1217 Magnetic Expression of Terranes in France and Their Correlation Beneath Overstep  
1218 Sequences, in: Chantraine, J., Rolet, J., Santallier, D.S., Piqué, A., Keppie, J.D. (Eds.),  
1219 *Pre-Mesozoic Geology in France and Related Areas*. Springer Berlin Heidelberg,  
1220 Berlin, Heidelberg, pp. 49–72. [https://doi.org/10.1007/978-3-642-84915-2\\_2](https://doi.org/10.1007/978-3-642-84915-2_2)
- 1221 Averbuch, O., Piromallo, C., 2012. Is there a remnant Variscan subducted slab in the mantle  
1222 beneath the Paris basin? Implications for the late Variscan lithospheric delamination  
1223 process and the Paris basin formation. *Tectonophysics* 558, 70–83.
- 1224 Beccaletto, L., Hanot, F., Serrano, O., Marc, S., 2011. Overview of the subsurface structural  
1225 pattern of the Paris Basin (France): Insights from the reprocessing and interpretation  
1226 of regional seismic lines. *Mar. Pet. Geol.* 28, 861–879.  
1227 <https://doi.org/10.1016/j.marpetgeo.2010.11.006>
- 1228 Beck, S., Ribon, O., Riedinger, N., 2021. Chiffres clés de l'énergie édition 2021. Ministère de  
1229 la transition écologique.
- 1230 Bel, A., Poux, A., Goyénèche, O., Allier, D., Darricau, G., Lemale, J., 2012. Etude préalable à  
1231 l'élaboration du schéma de développement de la géothermie en Île-de-France (Rapport  
1232 No. BRGM/RP-60615-FR). BRGM, Orléans.
- 1233 Bergerat, F., 1984. La fracturation nivernaise: Influences bourguignonne et centralienne sur la  
1234 structuration du Nivernais. *Bull. Inf. Géologues Bassin Paris* 21, 27–31.
- 1235 Bohnsack, D., Potten, M., Pfrang, D., Wolpert, P., Zosseder, K., 2020. Porosity–permeability  
1236 relationship derived from Upper Jurassic carbonate rock cores to assess the regional  
1237 hydraulic matrix properties of the Malm reservoir in the South German Molasse  
1238 Basin. *Geotherm. Energy* 8, 12. <https://doi.org/10.1186/s40517-020-00166-9>



- 1239 Bonté, D., Guillou-Frottier, L., Garibaldi, C., Bourguine, B., Lopez, S., Bouchot, V., Lucazeau,  
1240 F., 2010. Subsurface temperature maps in French sedimentary basins: new data  
1241 compilation and interpolation. *Bull. Société Géologique Fr.* 181, 377–390.
- 1242 Borgomano, J.R.F., Fournier, F., Viseur, S., Rijkels, L., 2008. Stratigraphic well correlations  
1243 for 3-D static modeling of carbonate reservoirs. *AAPG Bull.* 92, 789–824.  
1244 <https://doi.org/10.1306/02210807078>
- 1245 Briais, J., Guillocheau, F., Lasseur, E., Robin, C., Châteauneuf, J.J., Serrano, O., 2016.  
1246 Response of a low subsiding intracratonic basin to long wavelength deformations: the  
1247 Palaeocene–early Eocene period in the Paris basin. *Solid Earth* 7, 205–228.  
1248 <https://doi.org/10.5194/se-7-205-2016>
- 1249 Brigaud, B., Durllet, C., Deconinck, J.-F., Vincent, B., Thierry, J., Trouiller, A., 2009. The  
1250 origin and timing of multiphase cementation in carbonates: Impact of regional scale  
1251 geodynamic events on the Middle Jurassic Limestones diagenesis (Paris Basin,  
1252 France). *Sediment. Geol.* 222, 161–180. <https://doi.org/10.1016/j.sedgeo.2009.09.002>
- 1253 Brigaud, B., Vincent, B., Carpentier, C., Robin, C., Guillocheau, F., Yven, B., Huret, E.,  
1254 2014a. Growth and demise of the Jurassic carbonate platform in the intracratonic Paris  
1255 Basin (France): interplay of climate change, eustasy and tectonics. *Mar. Pet. Geol.* 53,  
1256 3–29. <https://doi.org/10.1016/j.marpetgeo.2013.09.008>
- 1257 Brigaud, B., Vincent, B., Durllet, C., Deconinck, J.-F., Blanc, P., Trouiller, A., 2010. Acoustic  
1258 Properties of Ancient Shallow-Marine Carbonates: Effects of Depositional  
1259 Environments and Diagenetic Processes (Middle Jurassic, Paris Basin, France). *J.*  
1260 *Sediment. Res.* 80, 791–807. <https://doi.org/10.2110/jsr.2010.071>
- 1261 Brigaud, B., Vincent, B., Durllet, C., Deconinck, J.-F., Jobard, E., Pickard, N., Yven, B.,  
1262 Landrein, P., 2014b. Characterization and origin of permeability–porosity  
1263 heterogeneity in shallow-marine carbonates: From core scale to 3D reservoir  
1264 dimension (Middle Jurassic, Paris Basin, France). *Mar. Pet. Geol.* 57, 631–651.  
1265 <https://doi.org/10.1016/j.marpetgeo.2014.07.004>
- 1266 Brigaud, B., Vincent, B., Pagel, M., Gras, A., Noret, A., Landrein, P., Huret, E., 2018.  
1267 Sedimentary architecture, depositional facies and diagenetic response to intracratonic  
1268 deformation and climate change inferred from outcrops for a pivotal period  
1269 (Jurassic/Cretaceous boundary, Paris Basin, France). *Sediment. Geol.* 373, 48–76.  
1270 <https://doi.org/10.1016/j.sedgeo.2018.04.011>
- 1271 Brosse, É., Badinier, G., Blanchard, F., Caspard, E., Collin, P.Y., Delmas, J., Dezayes, C.,  
1272 Dreux, R., Dufournet, A., Durst, P., Fillacier, S., Garcia, D., Grataloup, S., Hanot, F.,  
1273 Hasanov, V., Houel, P., Kervévan, C., Lansart, M., Lescanne, M., Menjz, A.,  
1274 Monnet, M., Mougine, P., Nedelec, B., Poutrel, A., Rachez, X., Renoux, P., Rigollet,  
1275 C., Ruffier-Meray, V., Saysset, S., Thinon, I., Thoraval, A., Vidal-Gilbert, S., 2010.  
1276 Selection and Characterization of Geological Sites able to Host a Pilot-Scale CO<sub>2</sub>  
1277 Storage in the Paris Basin (GéoCarbone -PICOREF). *Oil Gas Sci. Technol. – Rev.*  
1278 *L’Institut Fr. Pétrole* 65, 375–403. <https://doi.org/10.2516/ogst/2009085>
- 1279 Brunet, M.-F., Le Pichon, X., 1982. Subsidence of the Paris basin. *J. Geophys. Res. Solid*  
1280 *Earth* 87, 8547–8560.
- 1281 Casini, M., Ciuffi, S., Fiordelisi, A., Mazzotti, A., Stucchi, E., 2010. Results of a 3D seismic  
1282 survey at the Travale (Italy) test site. *Geothermics* 39, 4–12.  
1283 <https://doi.org/10.1016/j.geothermics.2009.11.003>
- 1284 Cazes, M., Torrelles, G., 1988. Étude de la croûte terrestre par sismique profonde: profil nord  
1285 de la France; structure hercynienne. Technip Ophrys editions.
- 1286 Collin, P.Y., Loreau, J.P., Courville, P., 2005. Depositional environments and iron ooid  
1287 formation in condensed sections (Callovian-Oxfordian, south-eastern Paris basin,

1288 France). *Sedimentology* 52, 969–985. <https://doi.org/10.1111/j.1365->  
1289 3091.2005.00728.x

1290 Contini, D., Mangold, C., 1980. Evolution paléogéographique de la France au Jurassique  
1291 moyen, in: Enay, R., Mangold, C. (Eds.), *Synthèse paléogéographique du Jurassique*  
1292 français, Docum. Lab. Géol. Lyon. Groupe d'étude français du Jurassique, pp. 66–70.

1293 Delmas, J., Brosse, E., Houel, P., 2010. Petrophysical Properties of the Middle Jurassic  
1294 Carbonates in the PICOREF Sector (South Champagne, Paris Basin, France). *Oil Gas*  
1295 *Sci. Technol. – Rev. L'Institut Fr. Pétrole* 65, 405–434.  
1296 <https://doi.org/10.2516/ogst/2010002>

1297 Dentzer, J., Bruel, D., Delescluse, M., Chamot-Rooke, N., Beccaletto, L., Lopez, S.,  
1298 Courrioux, G., Violette, S., 2018. Thermal and seismic hints for chimney type cross-  
1299 stratal fluid flow in onshore basins. *Sci. Rep.* 8. <https://doi.org/10.1038/s41598-018->  
1300 33581-x

1301 Drouiller, Y., Hanot, F., Gillot, E., Ferran, J.-C., Michel, L., 2019. 3D seismic for design and  
1302 derisking of dual geothermal boreholes in sedimentary sequences and new prospects  
1303 in the Paris Basin (Adapted methodology using petroleum industry techniques). *Oil*  
1304 *Gas Sci. Technol. – Rev. D'IFP Energ. Nouv.* 74, 32.  
1305 <https://doi.org/10.2516/ogst/2018106>

1306 Embry, A.F., Johannessen, E.P., 2017. Two approaches to sequence stratigraphy, in:  
1307 *Stratigraphy & Timescales*. Elsevier, pp. 85–118.

1308 Enay, R., Mangold, C., 1980. *Synthèse paléogéographique du Jurassique français*, Docum.  
1309 Lab. Géol. Lyon. Groupe d'étude français du Jurassique.

1310 Fabris, H., 1975. Les températures dans les forages - Gisements pétroliers du bassin Parisien  
1311 et de l'Aquitaine (Rapport No. 75 SGN 062 GTH). BRGM, Orléans.

1312 Feng, R., Balling, N., Grana, D., 2020. Lithofacies classification of a geothermal reservoir in  
1313 Denmark and its facies-dependent porosity estimation from seismic inversion.  
1314 *Geothermics* 87, 101854. <https://doi.org/10.1016/j.geothermics.2020.101854>

1315 Garcia, J.-P., Dromart, G., 1997. The validity of two biostratigraphic approaches in sequence  
1316 stratigraphic correlations: brachiopod zones and marker-beds in the Jurassic.  
1317 *Sediment. Geol.* 114, 55–79. [https://doi.org/10.1016/S0037-0738\(97\)00072-9](https://doi.org/10.1016/S0037-0738(97)00072-9)

1318 Garcia, J.-P., Laurin, B., Sambet, G., 1996. Les associations de brachiopodes du Jurassique  
1319 moyen du bassin de Paris; une échelle biochronologique ponctuee de niveaux-reperes  
1320 pour la contrainte des correlations sequentielles a haute resolution. *Bull. Société*  
1321 *Géologique Fr.* 167, 435–451.

1322 Gaumet, F., 1997. *Fondements géologiques pour la modélisation stratigraphique des systèmes*  
1323 *carbonatés: le jurassique moyen de l'Angleterre à la Méditerranée (PhD Thesis)*.  
1324 Université de Lyon 1.

1325 Gaumet, F., Garcia, J.-P., Dromart, G., Allemand, P., 2001. Middle Jurassic production rates  
1326 and “patchy” architecture of the carbonate systems along the north western Thetysian  
1327 margin (Paris basin to Subalpine basin). *Géologie Méditerranéenne* 79–83.

1328 Gaumet, F., Garcia, J.-P., Dromart, G., Sambet, G., 1996. Contrôle stratigraphique des facies,  
1329 geometries et profils de depot de la plate-forme carbonatée bourguignonne au  
1330 Bathonien-Callovien. *Bull. Société Géologique Fr.* 167, 409–421.

1331 Guillocheau, F., Robin, C., Allemand, P., Bourquin, S., Brault, N., Dromart, G., Friedenber,  
1332 R., Garcia, J.-P., Gaulier, J.-M., Gaumet, F., Grosdoy, B., Hanot, F., Le Strat, P.,  
1333 Mettraux, M., Nalpas, T., Prijac, C., Rigoltet, C., Serrano, O., Grandjean, G., 2000.  
1334 Meso-Cenozoic geodynamic evolution of the Paris Basin: 3D stratigraphic constraints.  
1335 *Geodin. Acta* 13, 189–245. <https://doi.org/10.1080/09853111.2000.11105372>

1336 Hamm, V., Castillo, C., Le Brun, M., Goyenche, O., 2010. Mise en œuvre de la gestion de la  
1337 ressource géothermique du Dogger de la région Ile-de-France dans le cadre du

1338 dispositif d'acquisition et de stockage des données. (Rapport No. RP-58834-FR).  
1339 BRGM, Orléans.

1340 Hamm, V., de Treil, J., Receveur, J., 2015. Gestion du Dogger et corrélation entre niveaux  
1341 producteurs. (Rapport No. RP-65472-FR). BRGM, Orléans.

1342 Hardenbol, J.A.N., Thierry, J., Farley, M.B., Jacquin, T., De Graciansky, P.-C., Vail, Peter R.,  
1343 1998. Mesozoic and Cenozoic sequence chronostratigraphic framework of European  
1344 basins, in: De Graciansky, P.-C., Hardenbol, J.A.N., Jacquin, T., Vail, P. R. (Eds.),  
1345 Mesozoic and Cenozoic Sequence Stratigraphy of European Basins. Special  
1346 Publications of SEPM, pp. 3–13.

1347 Harris, P.M., Purkis, S.J., Ellis, J., Swart, P.K., Reijmer, J.J., 2015. Mapping bathymetry and  
1348 depositional facies on Great Bahama Bank. *Sedimentology* 62, 566–589.

1349 Hendry, J.P., 2002. Geochemical trends and palaeohydrological significance of shallow burial  
1350 calcite and ankerite cements in Middle Jurassic strata on the East Midlands Shelf  
1351 (onshore UK). *Sediment. Geol.* 151, 149–176. [https://doi.org/10.1016/S0037-](https://doi.org/10.1016/S0037-0738(01)00236-6)  
1352 [0738\(01\)00236-6](https://doi.org/10.1016/S0037-0738(01)00236-6)

1353 Houel, P., Delmas, J., 2013. Synthèse des données géologiques sur le bassin de Paris (Rapport  
1354 IFP No. Rapport n° 63030). IFP Energies nouvelles, Rueil-Malmaison.

1355 Housse, B., Maget, Ph., Lavigne, J., Fabris, H., Gable, R., Rojas, J., 1976. Potentiel  
1356 géothermique du bassin parisien (Rapport No. 74-7-0990). BRGM, Orléans.

1357 Jacquin, T., Dardeau, G., Durllet, C., de Graciansky, P.-C., Hantzpergue, P., 1998. The North  
1358 Sea cycle: an overview of 2nd-order transgressive/regressive facies cycles in western  
1359 Europe, in: De Graciansky, P.-C., Hardenbol, J.A.N., Jacquin, T., Vail, P.R. (Eds.),  
1360 Mesozoic and Cenozoic Sequence Stratigraphy of European Basins. Publisher: Special  
1361 Publications of SEPM, pp. 445–466.

1362 Jacquin, T., Garcia, J.P., Ponsot, C., Thierry, J., Vail, P.R., 1992. Séquences de dépôt et  
1363 cycles régressif/transgressifs en domaine marin carbonaté : exemple du Dogger du  
1364 Bassin de Paris; Depositional sequences and regressive/transgressive facies cycles in  
1365 marine carbonate settings : example of the Dogger of the Paris Basin. *Comptes Rendus*  
1366 *Académie Sci. Ser. II Fasc. -Sci. Terre Planetes* 315, 353–362.

1367 Javaux, C., 1992. La plate-forme parisienne et bourguignonne au Bathonien terminal et au  
1368 Callovien: dynamique sédimentaire, séquentielle et diagenétique: place et création des  
1369 réservoirs potentiels (PhD Thesis). Université de Bourgogne.

1370 Kenyon, W.E., Day, P.I., Straley, C., Willemsen, J.F., 1988. A Three-Part Study of NMR  
1371 Longitudinal Relaxation Properties of Water-Saturated Sandstones. *SPE Form. Eval.*  
1372 3, 622–636. <https://doi.org/10.2118/15643-PA>

1373 Le Brun, M., Hamm, V., Lopez, S., Ungemach, P., Antics, M., Ausseur, J.Y., Cordier, E.,  
1374 Giuglaris, E., Goblet, P., Lalos, P., 2011. Hydraulic and thermal impact modelling at  
1375 the scale of the geothermal heating doublet in the Paris Basin, France, in: Proceedings  
1376 of the 36 Workshop on Geothermal Reservoir Engineer. Stanford, California, USA, p.  
1377 14.

1378 Le Nir, M., Bézèlgues, S., Ranquet, C., Szymanski, A.L., Darricau, G., Lemale, J., 2008.  
1379 Ressources géothermiques du département de l'Essonne (91) (Rapport No.  
1380 BRGM/RP-56966-FR). BRGM, Orléans.

1381 Lenoir, L., Blaise, T., Somogyi, A., Brigaud, B., Barbarand, J., Boukari, C., Nouet, J.,  
1382 Brézard-Oudot, A., Pagel, M., 2021. Uranium incorporation in fluorite and exploration  
1383 of U–Pb dating. *Geochronology* 3, 199–227. [https://doi.org/10.5194/gchron-3-199-](https://doi.org/10.5194/gchron-3-199-2021)  
1384 [2021](https://doi.org/10.5194/gchron-3-199-2021)

1385 Lopez, S., Hamm, V., Le Brun, M., Schaper, L., Boissier, F., Cotiche, C., Giuglaris, E., 2010.  
1386 40 years of Dogger aquifer management in Ile-de-France, Paris Basin, France.  
1387 *Geothermics* 39, 339–356. <https://doi.org/10.1016/j.geothermics.2010.09.005>

- 1388 Lucia, J.F., 2007. Carbonate Reservoir Characterization. Springer-Verl. Second Ed. 336 p.
- 1389 Lund, J.W., Toth, A.N., 2021. Direct utilization of geothermal energy 2020 worldwide  
1390 review. *Geothermics* 90, 101915. <https://doi.org/10.1016/j.geothermics.2020.101915>
- 1391 Lüschen, E., Dussel, M., Thomas, R., Schulz, R., 2011. 3D seismic survey for geothermal  
1392 exploration at Unterhaching, Munich, Germany. *First Break* 29, 45–54.  
1393 <https://doi.org/10.3997/1365-2397.2011002>
- 1394 Matray, J.M., Chery, L., 1998. Origin and age of deep waters of the Paris Basin, in: Causse,  
1395 C., Gasse, F. (Eds.), *Hydrologie et Géochimie Isotopique*. ORSTOM, Paris, France,  
1396 pp. 117–133.
- 1397 Matray, J.-M., Fontes, J.-C., 1990. Origin of the oil-field brines in the Paris basin. *Geology*  
1398 18, 501–504.
- 1399 Mégnien, C., Mégnien, F., 1980. Synthèse géologique du bassin de Paris, Mémoires du  
1400 BRGM. ed. Editions du BRGM, Orléans.
- 1401 Menjoz, A., Lambert, M., Matray, J.M., 1993. Flow of formation water in the Jurassic of the  
1402 Paris Basin and its effects. *The Royal Society* 344, 159–169.  
1403 <https://doi.org/10.1098/rsta.1993.0084>
- 1404 Nader, F.H., Champenois, F., Barbier, M., Adelinet, M., Rosenberg, E., Houel, P., Delmas, J.,  
1405 Swennen, R., 2016. Diagenetic effects of compaction on reservoir properties: The case  
1406 of early callovian “Dalle Nacrée” formation (Paris basin, France). *J. Geodyn.* 101, 5–  
1407 29. <https://doi.org/10.1016/j.jog.2016.05.010>
- 1408 Nurmi, R., 1986. The land of giants. *Middle East Well Eval. Rev.* 1, 7–21.
- 1409 Papachristou, M., Ungemach, P., Fytikas, M., 2016. Geothermal resource management - a  
1410 reservoir simulation approach - the Paris Basin case. *Bull. Geol. Soc. Greece* 47,  
1411 1938–1948. <https://doi.org/10.12681/bgsg.10996>
- 1412 Perrodon, A., Zabek, J., 1990. M 51: Interior Cratonic Basins, in: Paris Basin: Chapter 32:  
1413 Part II. Selected Analog Interior Cratonic Basins: Analog Basins, AAPG Special  
1414 Volumes. AAPG Special Volumes, pp. 633–679.
- 1415 Petrovic, A., Aigner, T., Pontiggia, M., 2018. Facies heterogeneities in a ramp carbonate  
1416 reservoir analogue: a new high-resolution approach for 3D facies modelling. *J. Pet.*  
1417 *Geol.* 41, 155–174. <https://doi.org/10.1111/jpg.12698>
- 1418 Phan, C., Plouhinec, C., Andreï, A., Beck, S., Foussard, A., Laghouati, R., Lauerjat, J.,  
1419 Lemaire, D., L’Homond-Fernandez, S., Misak, E., Nauroy, F., Ricaud, E., 2021.  
1420 Chiffres clés des énergies renouvelables Edition 2021 (Rapport No. 2557–8138).  
1421 Commissariat général au développement durable, Paris.
- 1422 Purser, B.H., 1985. Dedolomite Porosity and Reservoir Properties of Middle Jurassic  
1423 Carbonates in the Paris Basin, France, in: Roehl, P.O., Choquette, P.W. (Eds.),  
1424 Carbonate Petroleum Reservoirs, Casebooks in Earth Sciences. New York, NY, pp.  
1425 341–355.
- 1426 Purser, B.H., 1980. Sédimentation et diagenèse des carbonates néritiques récents: les éléments  
1427 de la sédimentation et de la diagenèse. Editions Technip.
- 1428 Purser, B.H., 1978. Early diagenesis and the preservation of porosity in Jurassic limestones. *J.*  
1429 *Pet. Geol.* 1, 83–94.
- 1430 Purser, B.H., 1972. Subdivision et interprétation des séquences carbonatées. *Mem BRGM* 77,  
1431 679–698.
- 1432 Rankey, E.C., 2014. Contrasts between wave- and tide-dominated oolitic systems: Holocene  
1433 of Crooked–Acklins Platform, southern Bahamas. *Facies* 60, 405–428.  
1434 <https://doi.org/10.1007/s10347-013-0385-x>
- 1435 Rojas, J., Giot, D., Le Nindre Y. M, Criaud, A., Fouillac, C., Brach, M., Menjoz, A., Martin,  
1436 J.-C., Lambert, M., 1989. Caractérisation et modélisation du réservoir géothermique  
1437 du Dogger, Bassin parisien, France (Rapport No. BRGM R 30169). BRGM, Orléans.

- 1438 Salaun, N., Toubiana, H., Mitschler, J.-B., Gigou, G., Carriere, X., Maurer, V., Richard, A.,  
1439 2020. High-resolution 3D seismic imaging and refined velocity model building  
1440 improve the image of a deep geothermal reservoir in the Upper Rhine Graben. *Lead.*  
1441 *Edge* 39, 857–863. <https://doi.org/10.1190/tle39120857.1>
- 1442 Serra, O., 1979. *Diagraphies différees - bases de l'interprétation. Tome 1 : Acquisition des*  
1443 *données diagraphiques.*, Bull. Cent. Rech. Explor.-Prod. Elf-Aquitaine, Pau.
- 1444 Thierry, J., Barrier, E., 2000. Middle Callovian, map 9, in: Dercourt, J., Gaetani, M.,  
1445 Vrielynck, B., Barrier, E., Biju-Duval, B., Brunet, M.F., Cadet, J.P., Crasquin, S.,  
1446 Sandulescu, M. (Eds.), *Atlas Peri-Tethys, Palaeogeographical Maps - Explanatory*  
1447 *Notes.* CCGM/CGMW, Paris, Paris, pp. 49–110.
- 1448 Thomas, H., Brigaud, B., Blaise, T., Saint-Bezar, B., Zordan, E., Zeyen, H., Andrieu, S.,  
1449 Vincent, B., Chirol, H., Portier, É., 2021. Contribution of drone photogrammetry to  
1450 3D outcrop modeling of facies, porosity, and permeability heterogeneities in carbonate  
1451 reservoirs (Paris Basin, Middle Jurassic). *Mar. Pet. Geol.* 123, 104772.  
1452 <https://doi.org/10.1016/j.marpetgeo.2020.104772>
- 1453 Tomassetti, L., Petracchini, L., Brandano, M., Trippetta, F., Tomassi, A., 2018. Modeling  
1454 lateral facies heterogeneity of an upper Oligocene carbonate ramp (Salento, southern  
1455 Italy). *Mar. Pet. Geol.* 96, 254–270. <https://doi.org/10.1016/j.marpetgeo.2018.06.004>
- 1456 Trippetta, F., Durante, D., Lipparini, L., Romi, A., Brandano, M., 2021. Carbonate-ramp  
1457 reservoirs modelling best solutions: Insights from a dense shallow well database in  
1458 Central Italy. *Mar. Pet. Geol.* 126, 104931.  
1459 <https://doi.org/10.1016/j.marpetgeo.2021.104931>
- 1460 Ungemach, P., Antics, M., Davaux, M., 2019. Subhorizontal well architecture and geosteering  
1461 navigation enhance well performance and reservoir evaluation A field validation, in:  
1462 *Proceedings, 44th Workshop on Geothermal Reservoir Engineering, Stanford*  
1463 *University, Stanford, California.* p. 12.
- 1464 Ungemach, P., Antics, M., Papachristou, M., 2005. Sustainable Geothermal Reservoir  
1465 Management. Presented at the *Proceedings World Geothermal Congress 2005,*  
1466 *Antalya, Turkey,* p. 12.
- 1467 Vail, P.R., Colin, J.P., Jan du Chene, R., Kuchly, J., Mediavilla, F., Trifilieff, V., 1987. La  
1468 stratigraphie sequentielle et son application aux correlations chronostratigraphiques  
1469 dans le Jurassique du bassin de Paris. *Bull. Société Géologique Fr.* III, 1301–1321.  
1470 <https://doi.org/10.2113/gssgfbull.III.7.1301>
- 1471 Vail, P.R., Mitchum Jr, R.M., Thompson III, S., 1977. Seismic stratigraphy and global  
1472 changes of sea level: Part 4. Global cycles of relative changes of sea level : Section 2.  
1473 Application of seismic reflection configuration to stratigraphic interpretation, in: M  
1474 26: *Seismic Stratigraphy-Applications to Hydrocarbon Exploration, Geology,*  
1475 *Geography, Environmental Science. AAPG Special Volumes,* pp. 83–97.
- 1476 Vincent, B., Brigaud, B., Thomas, H., Gaumet, F., 2021. Giant subaqueous carbonate dunes: a  
1477 revised interpretation of large-scale oo-bioclastic clinoforms in the middle Jurassic of  
1478 the Paris Basin and its implications. *Facies* 67, 1–28. [https://doi.org/10.1007/s10347-](https://doi.org/10.1007/s10347-021-00621-4)  
1479 [021-00621-4](https://doi.org/10.1007/s10347-021-00621-4)
- 1480 Wei, H.F., Ledoux, E., De Marsily, G., 1990. Regional modelling of groundwater flow and  
1481 salt and environmental tracer transport in deep aquifers in the Paris Basin. *J. Hydrol.*  
1482 120, 341–358.
- 1483 Westphal, H., Surholt, I., Kiesl, C., Thern, H.F., Kruspe, T., 2005. NMR Measurements in  
1484 Carbonate Rocks: Problems and an Approach to a Solution. *Pure Appl. Geophys.*  
1485 *PAGEOPH* 162, 549–570. <https://doi.org/10.1007/s00024-004-2621-3>
- 1486 Wielemaker, E., Cavalleri, C., Dahlhaus, L., Reynaldos, A., Sosio, G., Ungemach, P., Antics,  
1487 M., Davaux, M., 2020. Delineating the geothermal structure and flow properties in a

1488 sub-horizontal well with the use of wireline and LWD data in a multiphysics  
1489 approach., in: SPWLA 61st Annual Online Symposium Transactions. Presented at the  
1490 2020 SPWLA 61st Annual Online Symposium, Society of Petrophysicists and Well  
1491 Log Analysts. <https://doi.org/10.30632/SPWLA-5065>  
1492

1493